Master's thesis

NTNU
Norwegian University of Science and Technology
Faculty of Natural Sciences
Department of Chemical Engineering

Sindre Ottøy

VLE Measurements and Verification of a state-of-the-art Helmholtz Energy Equation of State for the Ternary Mixture of CO_2-N_2-CH_4

Master's thesis in Chemical Engineering
Supervisor: Jana P. Jakobsen, Jacob Stang, Tobias Neumann and Sigurd W. Løvseth

June 2019

NTNU
Kunnskap for en bedre verden

SINTEF

Sindre Ottøy

VLE Measurements and Verification of a state-of-the-art Helmholtz Energy Equation of State for the Ternary Mixture of CO_2-N_2-CH_4

Master's thesis in Chemical Engineering
Supervisor: Jana P. Jakobsen, Jacob Stang, Tobias Neumann and Sigurd W. Løvseth
June 2019

Norwegian University of Science and Technology
Faculty of Natural Sciences
Department of Chemical Engineering

Abstract

CO_2 can be captured on large scale from power generation and/or from carbon intensive industries. The captured CO_2 stream is not pure, it includes different types of impurities at different concentrations depending on the source and the chosen capture technology. The thermodynamic model for pure CO_2 [1] is highly accurate. However, the impurities can change the properties of the CO_2 stream significantly. These changes in properties due to small amounts of impurities can cause problems in any unit of the process. For example, increased compressor work, thermal effects, or corrosion may further lead to increased costs. Accurate thermodynamic models adjusted to highly accurate experimental data for CO_2-rich mixtures are therefore necessary to properly describe, develop, and optimize all the involved process units.

The models applied and discussed in this work are expressed in terms of the Helmholtz energy and are based on the GERG-2008 models [2]. Accurate experimental data of the fluid properties, e.g., densities, speed of sound, heat capacities, and vapor-liquid equilibrium, are used to fit, improve, or validate pure component and binary mixture parameters of the equations of state. The multicomponent mixture approach of the discussed thermodynamic model is based on the assumption to predict the mixture behaviour by combining the equations of state for the pure components and all possible binary mixture combinations.

An experimental setup for measuring the vapor-liquid equilibrium (VLE) of CO_2-rich mixtures has been built at SINTEF Energy within the project CO2Mix [3]. In this work, the apparatus has been used to measure VLE data of the ternary mixture of CO_2-N_2-CH_4 at the isotherms 223 K, 253 K, 273 K, 283 K, and 298 K and pressures in the range of 0.8 MPa to 9.3 MPa. The reported standard (k=1) uncertainty is lower than 14 mK for temperature, 1.5 kPa for pressure, and 0.06 mole percent for composition. The total standard uncertainty in terms of composition has been estimated to be lower than 0.07 mole percent for all the measurements.

The results were compared to the state-of-the-art Helmholtz energy based equation of state for the mixture of CO_2-N_2-CH_4, the EOS-CG- 2019 model [4]. All deviations between model and experimental data points are below 0.5 mole percent for liquid compositions and 1.0 mole percent for vapor compositions. In general, the model describes the data better at lower pressures and lower composition of N_2 and CH_4. Furthermore, the deviations between model and experimental points in the ternary mixture of CO_2-N_2-CH_4 follow the same trends seen in literature between model and experimental data for the binary mixtures of CO_2-N_2 [5] and CO_2-CH_4 [6]. To a large extent, the results presented in this work validate the assumption that the properties of the multicomponent mixture of CO_2-N_2-CH_4 can be described purely based on the pure component and binary mixture contributions.

Sammendrag

CO_2 kan fanges i stor skala fra store punktkilder som kraftverk og/eller karbonintensiv industri. Når CO_2-en fanges vil den ikke være ren, men inneholde flere forskjellige forurensninger i ulike konsentrasjoner avhengig av fangstteknologi og utslippskilde. Den termodynamiske modellen for ren CO_2 [1] er nøyaktig, men forurensingene kan endre egenskapene til CO_2-strømmen betydelig. Disse endrede egenskapene kan skape problemer i alle involverte prosessenheter. Økt kompressorarbeid, termiske effekter, eller korrosjon kan for eksempel føre til økte kostnader. Nøyaktige termodynamiske modeller tilpasset nøyaktige eksperimentelle data for CO_2-rike blandinger er derfor nødvendig for å beskrive, utvikle og optimalisere alle involverte prosesser på en god måte.

Modellene som er brukt og diskutert i dette arbeidet er uttrykt i Helmholtz energi og basert på GERG-2008 modellene [2]. Nøyaktige eksperimentelle data på fluidegenskaper, for eksempel tettheter, lydhastigheter, varmekapasiteter, og damp-væske likevekt, brukes til å tilpasse, forbedre eller validere parametere i tilstandsligningene for rene komponenter og binære blandinger. For å beskrive flerkomponentblandinger med disse modellene antas det at en flerkomponentblanding kan beskrives ved å kombinere tilstandsligningene for rene komponenter og alle mulige binære blandingers kombinasjoner.

Et eksperimentelt oppsett for å måle damp-væske likevekt i CO_2-rike blandinger har gjennom prosjektet CO2Mix blitt bygd ved SINTEF Energi [3]. I dette arbeidet har oppsettet blitt brukt til å måle damp-væske likevekt for den ternære blandingen CO_2-N_2-CH_4 på isotermene 223 K, 253 K, 273 K, 283 K, 298 K og trykk fra 0.8 MPa til 9.3 MPa. Rapportert standard (k=1) usikkerhet er under 14 mK for temperatur, 1.5 kPa for trykk og 0.06 molprosent for komposisjon. Den totale standard usikkerheten gitt i komposisjon er estimert til å være under 0.07 molprosent for alle målingene.

Måleresultatene har blitt sammenlignet med den mest nøyaktige Helmholtz energi-baserte tilstandsligningen for den ternære blandingen CO_2-N_2-CH_4, EOS-CG 2019 modellen [4]. Alle avvik mellom modell og eksperimentelle datapunkt er under 0.5 molprosent for væskekomposisjon og 1.0 molprosent for gasskonsentrasjon. Modellen beskriver generelt de eksperimentelle punktene best ved lave trykk og lavt innhold av N_2 og CH_4. Avvikene mellom modell og eksperimentelle punkt i den ternære blandingen CO_2-N_2-CH_4 følger de samme trendene som er rapportert i litteraturen mellom modell og eksperimentelle punkt for de binære blandingene CO_2-N_2 [5] og CO_2-CH_4 [6]. Resultatene presentert i dette arbeidet validerer i stor grad antagelsen om at egenskapene til flerkomponentblandingen CO_2-N_2-CH_4 kan beskrives utelukkende med rene komponentbidrag og binære blandingsbidrag.

Preface

The work presented in this thesis is the result of about two months summer job from June to August 2018, a specialization project during the fall of 2018 and the master thesis itself during the spring of 2019. The project is funded by Sintef Energy AS through the NCCS Centre and the partners stated under the "NCCS Acknowledgements" below.

After working on this project for nearly 12 months, I finally find the time to write the preface for this thesis. Surely, the work has tested my patience many times, especially when problems have occurred in the lab apparently for no reason. Luckily, I have been surrounded by people eager to help ever since the first day I started working on this project. Without them, the results and conclusions achieved in this thesis would not be possible. I certainly learned a lesson when it comes to research and how hard it can be to obtain valuable results. For example, the first two months of the project were mostly spent on preparing calibration gas mixtures, which was extremely tedious, manual work with long hours in the lab requiring full focus and high accuracy. This work was strictly needed to obtain the final results, but it did not provide any results directly. It was not until the start of December 2018 the first results were obtained. Thus, it took nearly six months to obtain any significant results due to extensive preparatory work to achieve satisfactory accuracy. Going through all these months without knowing if the final results would be useful was hard, and definitely increased my respect for full-time researchers.

For the first two months during the summer job I wish to thank Amanda Langørgen for the cooperation and all the fun discussions. Also thanks to Anders Austegard, Snorre F. Westman and Ingrid Snustand for their help in the lab during the summer. I certainly wish to thank my supervisors Jacob Stang, Tobias Neumann, Sigurd W. Løvseth and Jana P. Jakobsen for all your help during the entire project period. Jacob has been vital to all the work in the lab, coming up with new solutions to occurring problems during the experimental work and in general being very available for questions and supervising. Most likely, the measurements would not be completed without your help. Tobias has been supervising all the work with visualizing the model and comparing the measurement results to the model. Thanks for all the interesting discussions on thermodynamics and how to best visualize multi-dimensional surfaces in two or three dimensions. Thanks to Sigurd for giving me the opportunity to work on this project in the first place by offering the summer job position, and following up on the planning of the experimental work as well as the analysis through the entire project period. Finally, thanks to Jana for all your advise on project strategy, scientific writing and reminding me of the objectives of this project.

NCCS Acknowledgements
This publication was supported by the NCCS Centre, performed under the Norwegian research program Centres for Environment-friendly Energy Research (FME). The authors acknowledge the following partners for their contributions: Aker Solutions, ANSALDO Energia, CoorsTek Membrane Sciences, Equinor, EMGS, Gassco, KROHNE, Larvik Shipping, Norcem, Norwegian Oil and Gas, Quad Geometrics, Shell, TOTAL, and the Research Council of Norway (257579/E20).

Table of Contents

List of Tables

List of Figures

Nomenclature

List of symbols used for variables and functions. Parameters are not included in this list and are explained in the text as they are introduced. The most frequently used subscripts and superscripts are listed, but all sub- and superscripts will be introduced throughout the text. Notice that some symbols are used for different quantities, which will be specified in the text.

Abbreviations

EOS	=	Equation of State

Latin Symbols

a,A	=	Helmholtz energy
A	=	Area
C	=	Number of components
F	=	Degrees of freedom
g,G	=	Gibbs energy
G	=	Gravity constant
h	=	Enthalpy
l	=	Length
m	=	Mass
M	=	Molar mass
n	=	Moles
P	=	Number of phases
p	=	Pressure
r	=	Radius
R	=	Universal gas constant
R	=	Resistance
s	=	Entropy
s	=	Standard deviation
t	=	time
T	=	Temperature
u	=	Internal energy
u	=	Standard uncertainty
U	=	Weight reading
v	=	Specific volume
V	=	Volume
W	=	Resistance ratio
x,y,z	=	Mole fractions
X,Y,Ω,O	=	Energy potentials

Greek Symbols

α	=	Reduced Helmholtz Energy
δ	=	Reduced Density
Δ	=	Departure term
ξ	=	Transformed Variable
ρ	=	Density
τ	=	Reduced Temperature
ϕ	=	Air Humidity

Frequently used subscripts

c	=	Critical parameter
c	=	Combined
Cal	=	Calibration
$Calc$	=	Calculated
Exp	=	Exponential term
f	=	Final
GBS	=	Gaussian term
i	=	Component index
j	=	Component index
o	=	Pure fluid property
Pol	=	Polynomial term
r	=	Reducing parameter
r	=	Reference index
Spec	=	Special exponential term
T	=	Temperature index
tot	=	Total
v	=	Specific volume index
90	=	ITS-90 temperature scale

Frequently used superscripts

o	=	Ideal gas state
r	=	Residual

Chapter 1

Introduction and Background

1.1 Global Warming and Energy Demand

In 2018 the Intergovernmental panel on climate change (IPCC) delivered a special report on the impacts of global warming above 1.5 °C. [7]. The report clearly states that the consequences of a global rise in the average temperature of 1.5 °C are dramatic, including more extreme weather conditions such as hurricanes, drought and flooding. The 1.5 °C average scenario will also cause more extreme temperature changes, in for example arctic and high-altitude environments. This in turn has a potentially large impact on coastal ecosystems due to rise in sea level and temperature. However, according to the IPCC special report the consequences of an average global increase of 1.5 °C are far more manageable and less costly to handle than a temperature increase of 2 °C or higher.

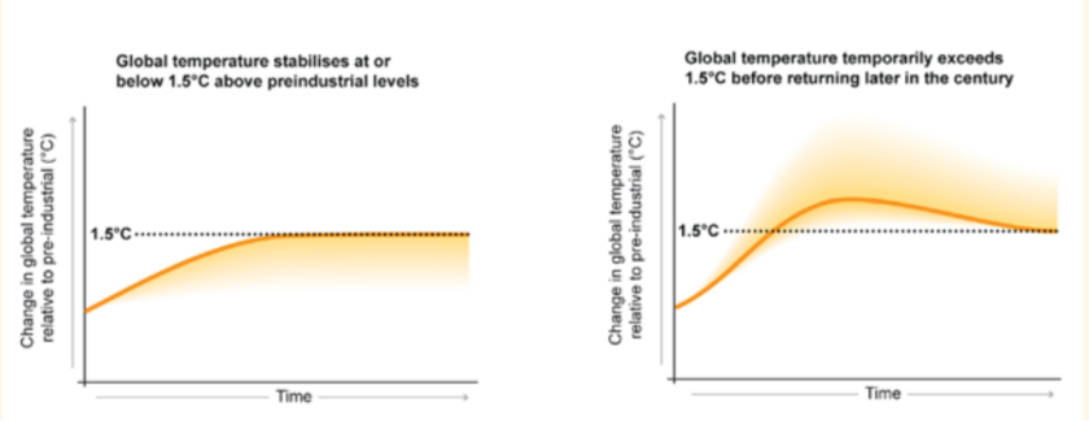

.

Figure 1.1: Two possible pathways to limit the global warming to 1.5 °C. The pathway to the left is characterized by a temperature stabilizing at 1.5 °C without exceeding the 1.5 limit. The other pathway illustrates how the global temperature will exceed 1.5 °C to a certain extent before returning to 1.5 °C later in the century by global net negative emissions of CO_2. ©IPCC [8]

The report further investigates various pathways to limit the global warming to a 1.5 °C increase. The main focus lies on two different pathways, illustrated in figure 1.1. The left figure

shows a stabilization at 1.5°C with no overshoot while the right shows a stabilization at 1.5 °C with a limited overshoot. The report states that ”All pathways that limit global warming to 1.5°C with limited or no overshoot project the use of carbon dioxide removal (CDR) on the order of 100–1000 GtCO2 over the 21st century.” Here, CDR refers to either afforestation or bioenergy with carbon capture and storage (BECCS). Fossil energy with carbon capture storage (CCS) is excluded since it only has net zero emissions. For comparison, one U.S. household would emit about 11.6 ton CO_2 per year if the electricity is produced solely by coal fired power plants[9] [10]. Thus, the lowest estimate of the use of CDR (100 $GtCO_2$) corresponds to approximately 85 million US household emissions over a duration of 100 years. To avoid a temperature overshoot, as illustrated in the left picture in Figure 1.1, the global CO_2-emissions must start declining before 2030. However, the reported emission goals of governments worldwide are not enough to start declining the global emissions by 2030. Hence, the pathway leading to a global temperature exceeding 1.5 °C is currently a significantly more likely pathway and requires CDR in the upper range of 100-1000 $GtCO_2$ over the 21st century. According to the Energy outlook 2018 report from the International Energy Agency (IEA) [11], the ”New Policies Scenario” leads to a 16% increase in the use of fossil fuels from 2017 to 2040. The New Policies Scenario is estimated and based on the current energy policies of governments and the likely results of announced policy intentions, see Figure 1.2.

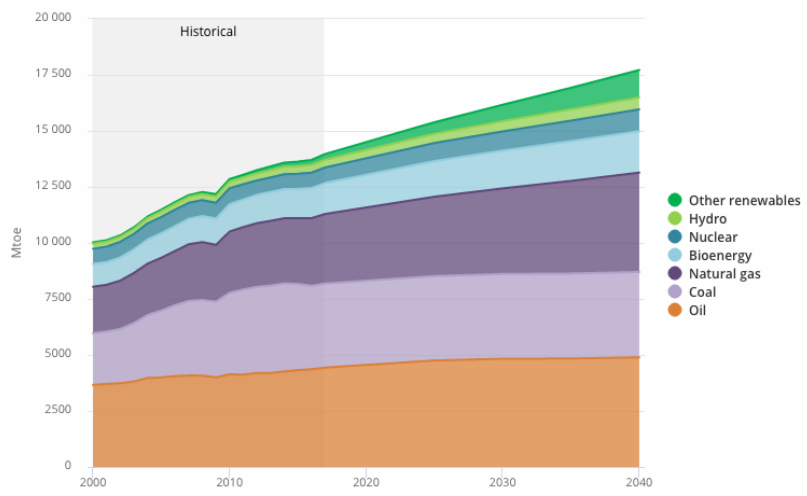

Figure 1.2: Historical (2000 to 2017) energy demand and future (2018-2040) energy demand in the New Policies Scenario presented by the International Energy Agency (IEA). ©IEA [11]

Figure 1.3 shows the ”Sustainable Development Scenario”, leading to a 27% decrease in the total fossil energy production. However, the fossil energy production will still contribute to 60% of the total energy mix compared to 74% in the ”New Policies Scenario” and 80% today. As a consequence, the potential emission reduction by successfully implemented CCS is huge. Furthermore, sufficient emission reduction of CO_2 is dependent on successfully implemented CCS in large scale.

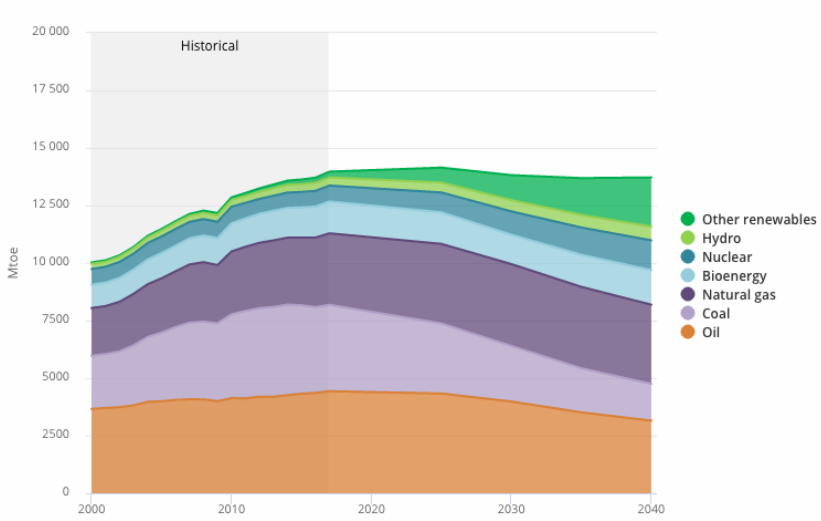

Figure 1.3: Historical (2000 to 2017) energy demand and future (2018-2040) energy demand in the Sustainable Development Scenario presented by the International Energy Agency (IEA). ©IEA [11]

1.2 Carbon Capture Storage

Carbon Capture Storage is the process of capturing CO_2 from emission sources and transport it to an appropriate and safe reservoir for long term storage. An overview of the CCS value chain is illustrated in Figure 1.4. The capturing process is complicated and costly, because an advanced process unit is needed to capture the CO_2 from the source. It is therefore advantageous to capture the CO_2 at large point sources, such as power plants, gas processing units or industry producing exhaust gases with high CO_2 content. Subsequent, the captured CO_2 must be prepared for transportation by purification, compression and cooling. Finally, the captured CO_2 is injected to a reservoir for long-term storage. Minor changes in purity, pressure or temperature may result in significant cost and safety effects. The optimization of the transportation conditions is therefore an important part of making CCS economically feasible.

1.3 CCS in Norway

In 2015 the Norwegian government started a full scale CCS project and requested a feasibility study of a full scale CCS value chain in Norway. In the fall of 2017 the three companies Norcem (cement producer in Brevik), Yara (fertilizer producer in Porsgrunn), and Fortum Oslo Varme (waste-to-energy plant outside Oslo) delivered concept reports on how the companies could realize full scale CO_2-capture at their plant locations. Based on these reports, the government decided to proceed with a capture unit at Norcems plant. The main reasons for choosing Norcem were low cost per ton captured CO_2 and the fact that the global cement industry is a large contributor to CO_2-emission. The captured CO_2 will be transported to the west coast of Norway (Øygarden) by ship for temporary storage and further transportation by pipeline to a reservoir offshore where the CO_2 will be stored. The transportation and storage part of the value chain have been outsourced to the three industry partners Equinor, Shell and Total [13]. They have defined the project ”Northern Lights” and made a separate feasibility study for the transportation and storage part of the value chain. The project is divided into two phases. The

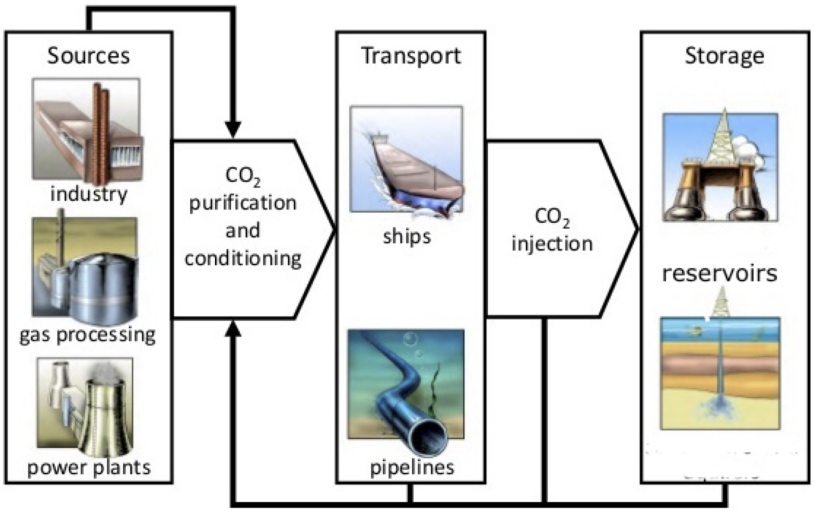

Figure 1.4: Overview of the CCS value chain ©Sintef [12].

first part consist of building an infrastructure able to handle 1.4 million ton CO_2 and the second part of increasing the capacity to 4 million ton [14].

As part of the Norwegian government plan of realizing full scale CCS in Norway, the Norwegian CCS Research Center (NCCS) was established as a program under the Centre for Environment-Friendly Energy Research (FME). The main goals of the NCCS project are to ensure Norways leading position in CCS technology, support achieving CO_2-storage in the North Sea, and realize a full-scale CCS chain by 2022. The strategy within NCCS to achieve these goals is to divide the center into 12 main tasks [15]. This work is part of task 8, Fiscal Metering and Thermodynamics, which goal is to ”(...)provide improved experimental data and models on properties of CO_2-rich mixtures relevant for CCS and facilitate fiscal metering of the same fluids.” [16].

1.4 Properties of CO_2-rich Mixtures

Research on the physical properties of CO_2-rich mixtures has been defined as a task on its own because of its importance in any of the process units in CCS technology. Accurate thermodynamic equations of state (EOS) are needed in order to model, dimension, and optimize the processes related to capture, transportation, and storage. The EOS for pure CO_2 is highly accurate. However, captured CO_2 might contain other components such as water, nitrogen, oxygen, argon, carbon monoxide, methane, hydrogen, various sulfides, nitrogen oxides, and amines. Since purification to 100% CO_2 is costly, it is more cost efficient to allow some impurities in the product being transported for long-term storage.

However, physical properties may change significantly when using CO_2-rich mixtures instead of pure CO_2. This has to be considered in the development of a process design to avoid problems. For instance, a mixture containing 5 mole% nitrogen and 95 mole% carbon dioxide has a saturation pressure which is 25 bar higher at 0 °C than pure CO_2 [5]. Those changes in physical properties may represent significant costs due to increased compressor work, thermal effects,

material quality, and corrosion.

To develop accurate thermodynamic EOS, accurate experimental data on densities, speed of sound, heat capacities, and phase equilibria are needed. An experimental apparatus for measuring the vapor-liquid equilibrium (VLE) has been developed at SINTEF Energy throughout the project CO_2Mix [3]. Measurement campaigns on the binary systems CO_2-N_2 [5], CO_2-O_2 [17], CO_2-Ar [18], CO_2-CH_4 [6] and CO_2-CO [19], obtaining highly accurate data are already completed. The VLE measurements, along with literature data, have been used to validate or adjust the parameters of the thermodynamic EOS for the binary mixtures.

An assumption of the highly accurate Helmholtz energy based EOS developed to describe multi-component CO_2-rich mixtures is that the multi-component mixture can be described purely based on the pure component and all possible binary combinations. However, little work has been done so far to verify this assumption for CO_2-rich mixtures. In this work, the ternary system of CO_2-N_2-CH_4 has been investigated to verify the thermodynamic EOS. VLE measurements at the isotherms 223 K, 253 K, 273 K, 283 K, and 298 K have been performed using the experimental apparatus for VLE measurements developed at the SINTEF Energy lab. Additionally, Matlab code developed at the Ruhr-Universät Bochum by Neumann [20] has been further developed to visualize the model behaviour of the ternary mixture. This enables the systematic investigation of the pure and binary contributions. The results of this work will contribute to increased insights in modeling of multi-component mixtures and verify whether a model solely based on pure fluids and binary mixtures predict the thermodynamic properties of the ternary mixture with satisfactory accuracies.

Chapter 2

Theory

2.1 Thermodynamic Equations of State

Thermodynamic equations of state (EOS) relate the state function to its state variables. The state function is unambiguously determined when all the thermodynamic state variables are specified. It does not depend on the previous values of neither state function nor state variable, only the current state. Thermodynamic EOS are usually divided into two main types, thermal and caloric EOS. The thermal EOS relate the state variables pressure (p), specific volume (v) and temperature (T). The simplest example is the ideal gas law, stated in equation 2.1 with R as the universal gas constant. Another example is the Van der Vaals EOS.

$$pv = TR \tag{2.1}$$

The caloric EOS relate the caloric property to its canonical, also called natural, variables. The most fundamental caloric property is the internal energy (u) with the canonical variables specific volume (v), composition (**x**) and entropy (s). However, the entropy is difficult to measure experimentally. Other caloric properties, or energy potentials, can be derived using the Legendre transformation:

$$\begin{aligned} f_i(\xi_i, x_j, x_k, ...x_n) \hat{=} & f(x_i, x_j, x_k, ...x_n) - \xi_i x_i, \\ \text{with } \xi_i \hat{=} & \left(\frac{\partial f}{\partial x_i}\right)_{x_j, x_k, ..., x_n} \end{aligned} \tag{2.2}$$

The Legendre transformation is a valid transformation for any convex function, i.e. function with a positive second derivative. The transformation can also be applied on several variables at once or in sequence, which will yield the same result:

$$f_i(\xi_i, \xi_j, x_k, ...x_n) \hat{=} f(x_i, x_j, x_k, ...x_n) - \xi_i x_i - \xi_j x_j \tag{2.3}$$

Applying the Legendre transformation to the internal energy with respect to the canonical variable entropy results in the new state function and energy potential called Helmholtz energy in the specific form:

$$a(T, v, x) = u(s, v, x) - \left(\frac{\partial u}{\partial s}\right)_{v,x} s \hat{=} u - Ts \tag{2.4}$$

The last part comes from the definition of $\left(\frac{\partial u}{\partial s}\right)_{v,x} \hat{=} T$. The internal energy can also be transformed with respect to all its canonical variables in any combination, giving 7 different energy

potentials derived from the internal energy. An overview of these is given in Table 2.1. The energy potentials named X, Y and Ω in Table 2.1 are little used, and a common name convention for these potentials has therefore not been established. The canonical variable chemical potential, μ, is described further in section 2.3. Complex integrals are needed to compute the energy

Table 2.1: Overview of energy potentials derived from internal energy and their canonical variables.

Function	**Canonical variables**		
Internal Energy (u)	v	**x**	s
Helmholtz Energy (a)	v	**x**	T
Enthalpy (h)	p	**x**	s
X	v	μ	s
Gibbs Energy (g)	p	**x**	T
Y	p	μ	s
Ω	v	μ	T
Zero-potential (O)	p	μ	T

potentials from thermal equations while the energy potentials are explicit in their canonical variables. On the other hand, all thermodynamic quantities can be calculated using combinations of derivatives of the energy potentials making them convenient as a basis for thermodynamic EOS. Both Helmholtz energy and Gibbs energy are explicit in measurable quantities (composition, volume, temperature and pressure, see Table 2.1) in contrast to internal energy or enthalpy where the entropy cannot be measured directly. Therefore, many thermodynamic EOS are written in terms of either Gibbs or Helmholtz energy. The Helmholtz energy is also a monotonic function over the entire fluid surface including the two-phase region [21] [20].

2.2 Helmholtz Energy EOS

For CO_2-rich mixtures Helmholtz energy based thermodynamic EOS are the state-of-the-art. The GERG-2008 model of Kunz and Wagner (2012) [2] was developed for natural gas mixtures. The GERG-2008 model was later used as a starting point to develop new EOS. First by Gernert and Span (2016) [22] to develop the EOS-CG 2016. Later, Herrig (2018) developed the EOS-CG 2019 model [4] as an extension to the EOS-CG 2016 model and Neumann *et al.* (2019) developed the EOS for mixtures containing ammonia [23]. The EOS-CG 2019 model is currently the state-of-the-art for the ternary mixture of CO_2-N_2-CH_4 studied in this work. An overview of CCS-relevant components and the state-of-the art EOS for each binary mixture are given in Figure 2.1. The models discussed above are Helmholtz energy based equations in the canonical variables temperature, density and composition. Notice that density is the inverse of specific volume, which was used as a canonical variable in section 2.1.

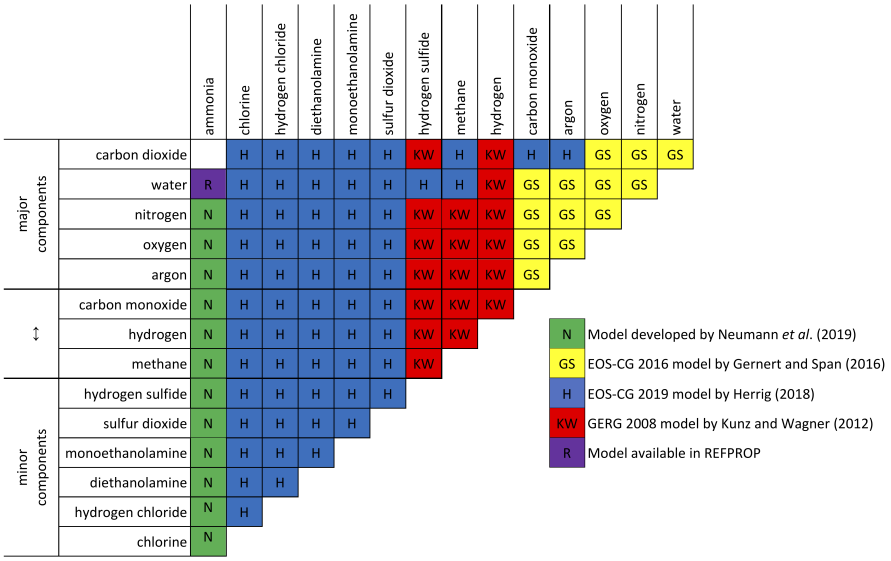

Figure 2.1: Overview of relevant impurities in CCS. The model that covers each binary mixture is specified (Neumann *et al.* (2019) [23], EOS-CG 2016 by Gernert and Span (2016) [22], EOS-CG 2019 by Herrig (2018) [4], GERG-2008 by Kunz and Wagner (2012) [2], and the reference database REFPROP [24]).

The Helmholtz energy of a fluid is divided into an ideal and residual part:

$$a(T, \rho, x) = a^o(T, \rho, x) + a^r(T, \rho, x) \tag{2.5}$$

The ideal part comes from the hypothetical ideal gas contribution of the pure component, while the residual part represents the deviation from the ideal behavior. The expression for the residual Helmholtz energy is purely constructed of empirically fitted terms, for both pure fluids and mixtures. This is further described in the next two subsections. To be clear, the residual part of the model is not derived from physical laws or principles but relies completely on an empirical approach. Hence, the fitted parameters of the Helmholtz based EOS do not have a physical meaning.

2.2.1 Pure Fluids

The Helmholtz energy is often used in a reduced form, reduced by the universal gas constant and temperature:

$$\alpha(\tau, \delta) = \frac{a(T, \rho)}{RT} = \frac{a^o(T, \rho) + a^r(T, \rho)}{RT} = \alpha^o(\tau, \delta) + \alpha^r(\tau, \delta) \tag{2.6}$$

For pure fluids, the reduced temperature and density are defined as given in equation 2.7, with ρ_c and T_c as the critical density and temperature, respectively.

$$\delta = \frac{\rho}{\rho_c} \text{ and } \tau = \frac{T_c}{T} \tag{2.7}$$

The residual part consists of polynomial, exponential and Gaussian terms purposed by Kunz and Wagner (2012) [2]:

$$\alpha^r(\tau, \delta) = \alpha^r_{\text{Pol}}(\tau, \delta) + \alpha^r_{\text{Exp}}(\tau, \delta) + \alpha^r_{\text{GBS}}(\tau, \delta) \tag{2.8}$$

with

$$\alpha^r_{\text{Pol}}(\tau,\delta) = \sum_{i=1}^{K_{\text{Pol}}} n_i \delta^{d_i} \tau^{t_i} \tag{2.9}$$

$$\alpha^r_{\text{Exp}}(\tau,\delta) = \sum_{i=1+K_{\text{Pol}}}^{K_{\text{Pol}}+K_{\text{Exp}}} n_i \delta^{d_i} \tau^{t_i} e^{-\delta^{p_i}} \tag{2.10}$$

$$\alpha^r_{\text{GBS}}(\tau,\delta) = \sum_{i=1+K_{\text{Pol}}+K_{\text{Exp}}}^{K_{\text{Pol}}+K_{\text{Exp}}+K_{\text{GBS}}} n_i \delta^{d_i} \tau^{t_i} e^{-\eta_i(\delta-\epsilon_i)^2-\beta_i(\tau-\gamma_i)^2} \tag{2.11}$$

The parameters n_i, d_i, t_i, p_i, η_i,β_i, ϵ_i, γ_i and the number of each term type, K_{Pol}, K_{Exp} and K_{GBS}, are fitted to experimental data.

2.2.2 Mixtures

For mixtures, the ideal part consists of the linear combination of the ideal contribution from each pure component, $\alpha^o_{o,j}(\tau_{o,j},\rho_{o,j})$, in the mixture:

$$\alpha^o(\tau,\rho,\mathbf{x}) = \sum_{j=1}^{N} x_j \left[\alpha^o_{o,j}(\tau_{o,j},\rho_{o,j}) + \ln(x_j)\right] \tag{2.12}$$

Since the critical temperature and density are different for different components, the reduced temperature and density are computed for each component, $\tau_{o,j}$ and $\rho_{o,j}$, based on the critical temperature and density of that component:

$$\tau_{o,j} = \frac{T_{c,j}}{T} \text{ and } \rho_{o,j} = \frac{\rho}{\rho_{c,j}} \tag{2.13}$$

The residual part of the Helmholtz energy for mixtures is based on the linear combination of the residual part of the pure components, $\alpha^r_{o,j}(\tau,\delta)$ and a departure term describing the non-ideal effects of mixing, $\Delta\alpha^r(\tau,\delta,\mathbf{x})$, specific for every mixture with composition $\mathbf{x}$:

$$\alpha^r(\tau,\delta,\mathbf{x}) = \sum_{j=1}^{N} x_j \alpha^r_{o,j}(\tau,\delta) + \Delta\alpha^r(\tau,\delta,\mathbf{x}) \tag{2.14}$$

The departure term is a sum of terms consisting of all the possible binary combinations of the components in the mixture:

$$\Delta\alpha^r(\tau,\delta,\mathbf{x}) = \sum_{i=1}^{N}\sum_{j=i+1}^{N} x_i x_j F_{i,j} \alpha_{i,j}(\tau,\delta) \tag{2.15}$$

where $F_{i,j}$ is a weighting factor for the binary mixture with component i and j [25]. $\alpha^r_{i,j}$ is the binary specific departure function possibly containing three different term types. These term types include polynomial, exponential and special exponential terms. The full expressions are

shown in equation 2.16:

$$\alpha_{i,j}^{r} = \sum_{k=1}^{K_{\text{Pol}}} n_{i,j,k}\delta^{d_{i,j,k}}\tau^{t_{i,j,k}} + \sum_{k=1+K_{\text{Pol}}}^{K_{\text{Pol}}+K_{\text{Exp}}} n_{i,j,k}\delta^{d_{i,j,k}}\tau^{t_{i,j,k}}e^{-\delta^{p_{i,j,k}}} + \sum_{k=1+K_{\text{Pol}}+K_{\text{Exp}}}^{K_{\text{Pol}}+K_{\text{Exp}}+K_{\text{spec}}} n_{i,j,k}\delta^{d_{i,j,k}}\tau^{t_{i,j,k}}e^{-\eta_{i,j,k}(\delta-\epsilon_{i,j,k})^2-\beta_{i,j,k}(\tau-\gamma_{i,j,i})} \quad (2.16)$$

The reduced temperature and density, τ and δ, in equations 2.14-2.16 represent the reduced temperature and density of the mixture. However, it is complicated to determine the critical point of a mixture. Therefore, the reducing functions for mixtures were introduced by Kunz *et al.* in 2007 [26]:

$$T_r(\mathbf{x}) = \sum_{i=1}^{N} x_i^2 T_{c,i} + \sum_{i=1}^{N-1}\sum_{j=i+1}^{N} 2x_i x_j \beta_{T,ij}\gamma_{T,ij}\frac{x_i + x_j}{\beta_{T,ij}^2 x_i + x_j}(T_{c,i}T_{c,j})^{0.5} \quad (2.17)$$

$$\frac{1}{\rho_r(\mathbf{x})} = \sum_{i=1}^{N} x_i^2 \frac{1}{\rho_{c,i}} + \sum_{i=1}^{N-1}\sum_{j=i+1}^{N} 2x_i x_j \beta_{v,ij}\gamma_{v,ij}\frac{x_i + x_j}{\beta_{v,ij}^2 x_i + x_j}\frac{1}{8}\left(\frac{1}{\rho_{c,i}^{1/3}} + \frac{1}{\rho_{c,j}^{1/3}}\right)^3 \quad (2.18)$$

where $\beta_{t,ij}$, $\gamma_{T,ij}$, $\beta_{v,ij}$ and $\gamma_{v,ij}$ are the reducing parameters of the binary mixture containing component i and j. The reducing parameters are fitted for each binary mixture. Figure 2.2 visualizes the structure of the Helmholtz energy based EOS.

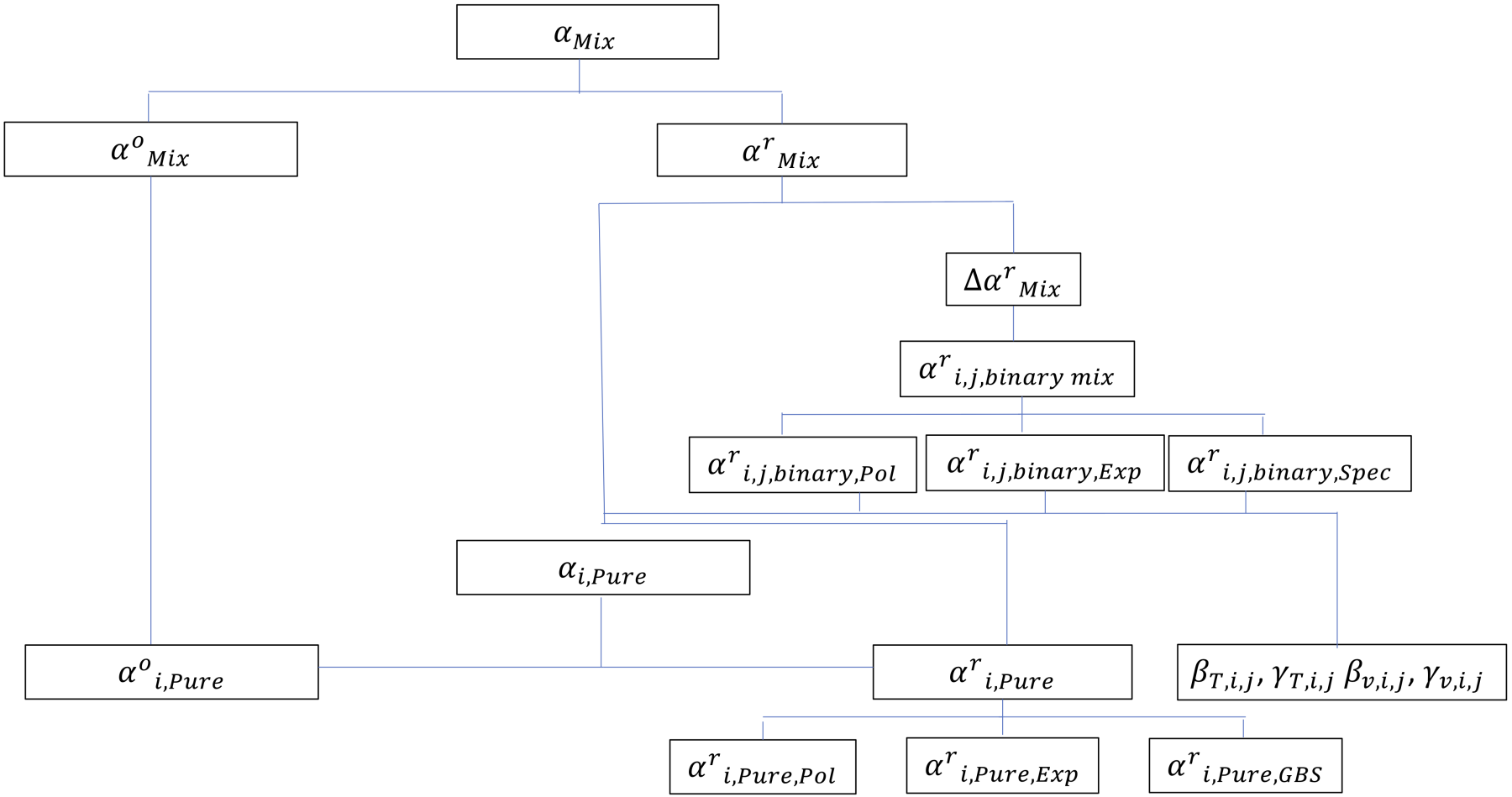

Figure 2.2: Illustration of how the Helmholtz energy based EOS are constructed, showing the build-up of the ideal and residual part of pure components and mixtures.

2.3 Phase Equilibrium

In general, two phases β_1 and β_2 with C components will be in equilibrium when the temperature, T, pressure, p, and chemical potential of all components, μ_i, are equal in the two phases, as given in equation 2.19 [27]. To be clear, the chemical potential in phase β_1 for component i is equal to the chemical potential in phase β_2 for component i at equilibrium, but not necessarily equal to the chemical potential of component $j \neq i$ in phase β_1 and β_2.

$$\begin{aligned} T^{\beta_1} &= T^{\beta_2} \\ p^{\beta_1} &= p^{\beta_2} \\ \mu_i^{\beta_1} &= \mu_i^{\beta_2} \end{aligned} \tag{2.19}$$

The chemical potential of a component, μ_i, can be defined in terms of Gibbs or Helmholtz energy as [27]:

$$\mu_i = \left(\frac{\partial G}{\partial n_i}\right)_{T,p,n_j \neq n_i} = \left(\frac{\partial A}{\partial n_i}\right)_{T,v,n_j \neq n_i} \tag{2.20}$$

Notice that the extensive form of the energy potentials are used (G, A), instead of the intensive form previously used (g,a). Thus, the unit is Joule rather than Joule/mole for the energy potentials and Joule/mole for the chemical potential. The chemical potential can also be defined in terms of other energy potentials, such as enthalpy or internal energy. If the chemical potential of each component is not equal in the two phases, driving forces will cause the composition of the two phases to change until equilibrium is reached. Notice that equal chemical potentials in two phases not necessarily means that the composition is equal. Gibbs phase rule, given in equation 2.19, states that the degrees of freedom (F) in the system equals number of components (C) minus the number of phases (P) plus 2 [28]. The cases of two phases (liquid and vapor) and one, two, or three components are discussed in more detail in the next paragraphs.

$$F = C - P + 2 \tag{2.21}$$

2.3.1 Pure Fluids

A physical matter consisting of one component usually exist in three different states of aggregation: solid, liquid and gas. Figure 2.3 shows the phase diagram of pure CO_2, illustrating the various phases existing at a given temperature and pressure. The solid-gas, solid-liquid and liquid-gas lines show the states where two phases coexist in equilibrium. At these equilibrium lines, the degree of freedom is one. Hence, specifying a temperature will determine the pressure and vice versa. At the triple point solid, liquid, and gas exist simultaneously. Thus, the degree of freedom is zero and the triple point can only exist at one specific temperature and pressure. Above the critical point the liquid-gas coexistence is no longer possible and a single super critical phase exist. In a carbon capture storage context the liquid-gas line is of great interest due to the significantly higher density of liquid than vapor, making it largely advantageous to transport and store the CO_2 in liquid state rather than vapor state.

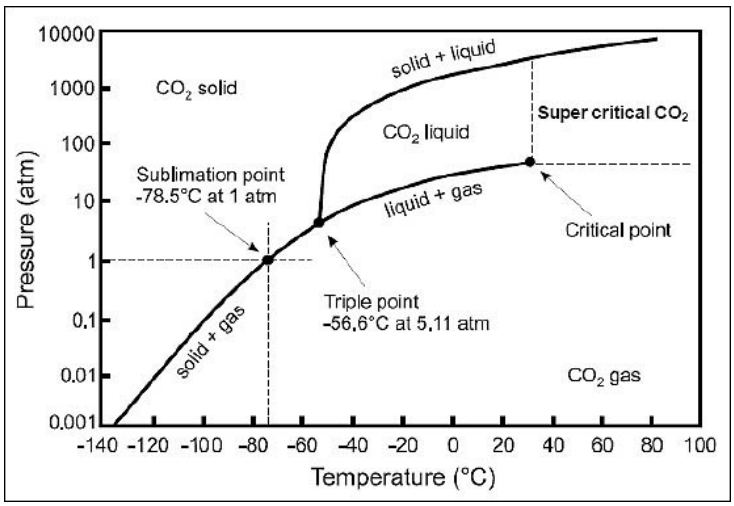

Figure 2.3: Phase diagram of pure CO_2, showing solid-gas line, solid-liquid line, liquid-gas line, triple point, sublimation point and critical point ©2013 Energy Institute, London [29].

2.3.2 Binary Mixture

For binary mixtures (two components), the phase diagram changes. According to Gibbs phase rule given in equation 2.21, a binary mixture in two phases has two degrees of freedom as compared to one degree of freedom for a single component. Consequently, the pressure is not fully specified by the temperature, but also depends on the composition of the mixture. This is illustrated in figure 2.4, where pressure is plotted as a function of mole fraction CO_2 at a constant temperature of 260 K. At a given temperature, pressure and total composition in the two-phase region, an equilibrium exist between the liquid and vapor phase. The composition of the liquid and vapor phase will be equal to the bubble and dew point composition at the given temperature and pressure. Given a liquid and vapor composition, the total composition will be somewhere on a line between the bubble and dew point composition, depending on the total mass of the liquid and vapor phase.

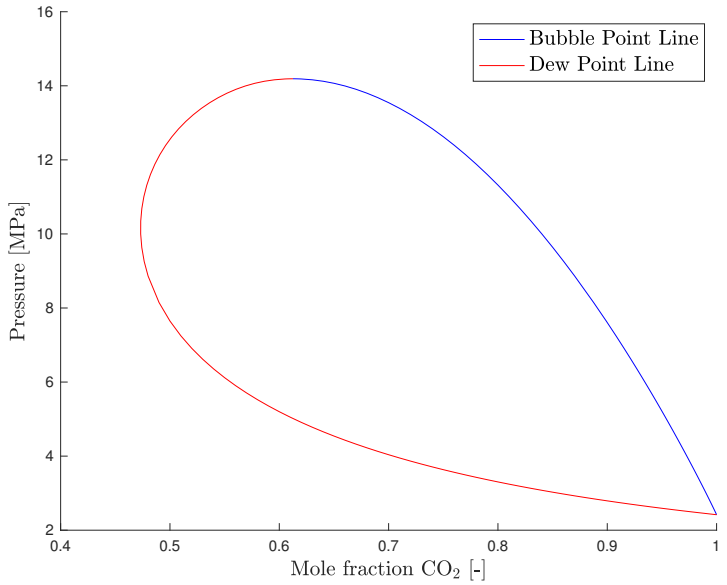

Figure 2.4: Phase diagram with respect to pressure and composition of CO_2 of a binary mixture of CO_2 and N_2 at 260 K, showing bubble point lines and dew point lines calculated with EOS-CG 2019.

2.3.3 Ternary Mixture

When a third component is introduced to a mixture, the degrees of freedom with two phases will be three according to Gibbs phase rule in equation 2.21. A fully determined state requires temperature, pressure, and the composition of one component to be specified. This is illustrated in Figure 2.5, showing the dew and bubble points of the ternary mixture CO_2-N_2-CH_4 in a three dimensional diagram, with mole fraction of CH_4 and N_2 on the x- and y-axis and pressure on the z-axis. The dew and bubble points are calculated by the EOS-CG 2019 model and mark the border of the two phase region. The gap between the dew and bubble points at high pressures results from numerical issues solving the model close to the critical region.

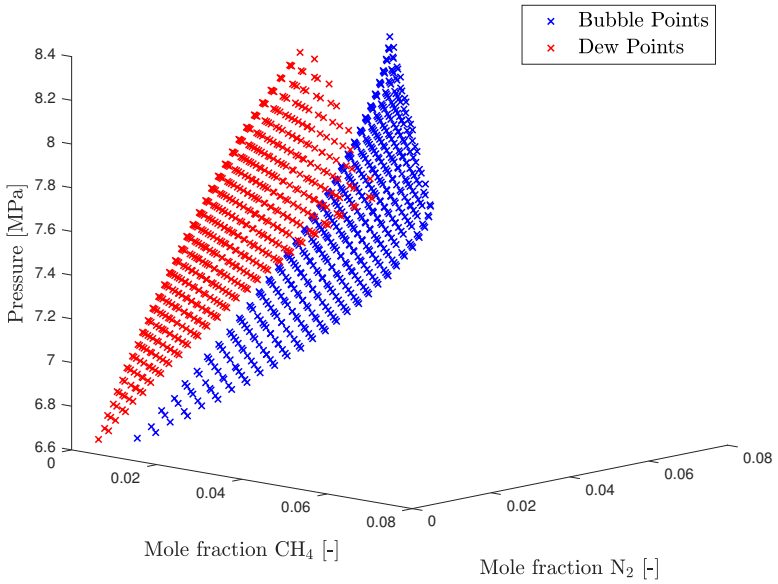

Figure 2.5: Three dimensional phase diagram of a ternary mixture of CO_2, N_2 and CH_4 showing dew and bubble points calculated by the EOS-CG 2019 at 298 K. The composition of CH_4 and N_2 are varied on the x- and y-axis. The gap between dew and bubble point at high pressures is due to numerical issues solving the model close to the critical region.

The two phase region of a ternary mixture can also be visualized in two dimensions by setting one additional variable constant. Figure 2.6 shows three diagrams of the two-phase region at constant temperature and pressure. The lines between corresponding dew and bubble points are often called tie lines. The total composition of the mixture (liquid and vapor combined) must lie on this line. Another way of visualizing the VLE in two dimensions is fixing the ratio of compositions between two components, generating a ”pseudo-binary” plot. An example of this is given in Figure 2.7. Since the bubble and dew points depend on the total composition in addition to temperature and pressure, the bubble and dew points at a given pressure will be slightly different for different total compositions. Therefore, several different dew and bubble points at the same pressure are shown in Figure 2.7.

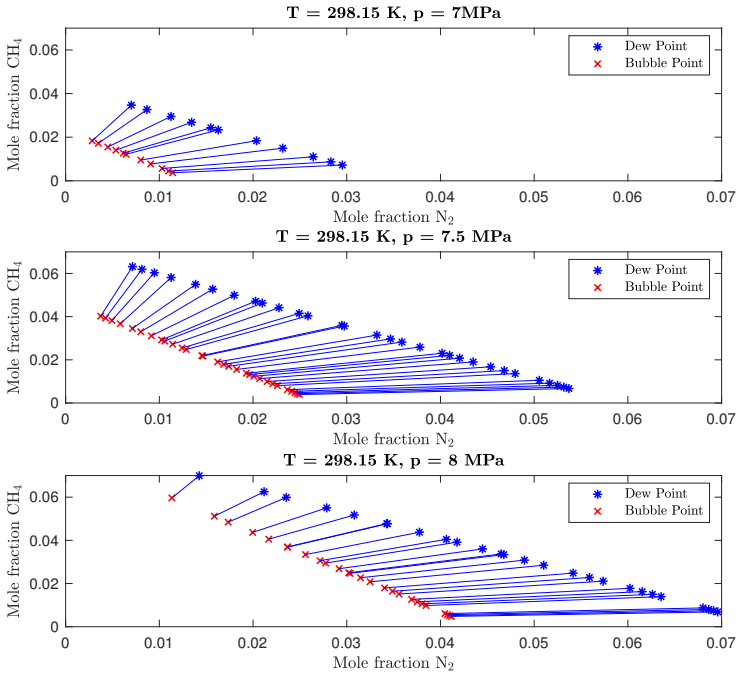

Figure 2.6: Two dimensional phase diagrams of a ternary mixture of CO_2, N_2 and CH_4 at 298 K and 7 MPa, 7.5 MPa and 8 MPa from top to bottom respectively, showing dew and bubble points calculated with the EOS-CG 2019.

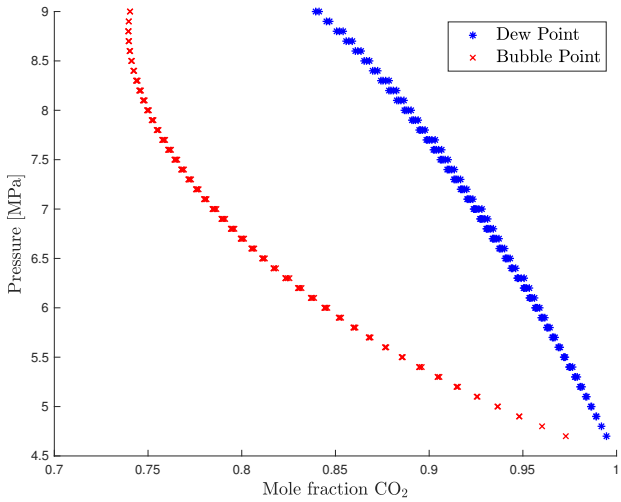

Figure 2.7: Two dimensional phase diagrams of a ternary mixture of CO_2, N_2 and CH_4 at 283 K and constant ratio of 1:1 between total composition of N_2 and CH_4. Dew and bubble points are calculated with EOS-CG 2019. The gap between dew and bubble point at high pressure is due to numerical issues solving the model close to the critical region.

2.4 Literature Data

Six publications on VLE measurements of the ternary mixture CO_2-N_2-CH_4 exist in the literature. They were published in the period of 1971-1992. In total, 291 VLE points have been published. An overview is given in Figure 2.8, illustrating the temperatures and pressures where the VLE data have been measured. Few measurements have been conducted above 273 K, only Xu *et al.* [30] measured at 293 K before. The articles by Sarashina *et al.* (1971) [31] and Trappehl *et al.* (1989) [32] have not stated any uncertainty. For the remaining four articles, Somait *et al.* (1978)[33], Al-Sahhaf *et al.* (1983, 1990) [34][35] and Xu *et al.* (1992), the uncertainty in temperature, pressure and composition range from 10 to 20 mK, 0.02 to 0.21 bar and 0.001 to 0.003 in mole fraction.

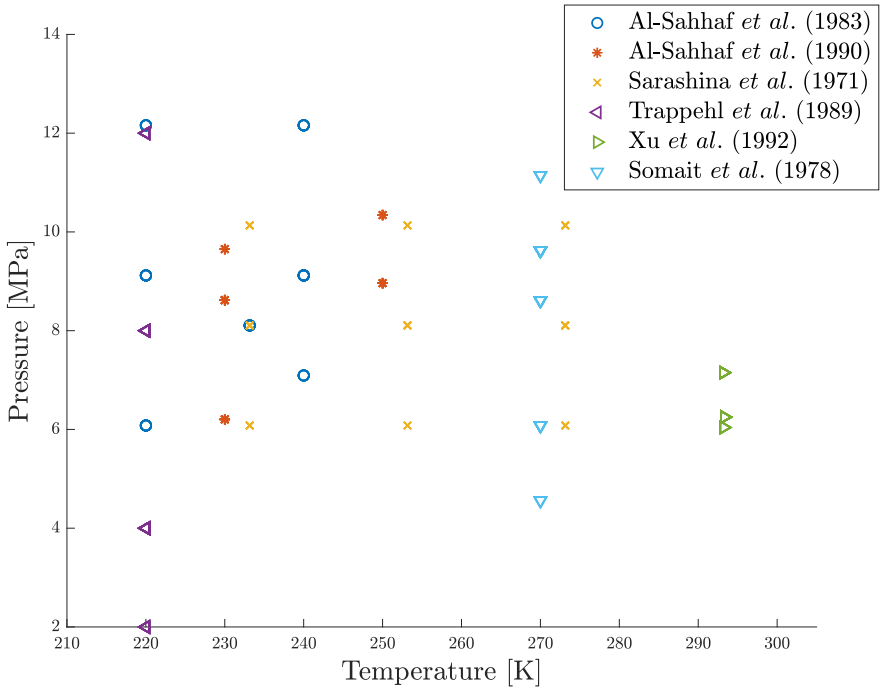

Figure 2.8: Summary of VLE literature data found on the ternary mixture of CO_2-N_2-CH_4.

Chapter 3

Experimental

The description of the experimental apparatus and the procedures used in the project are included with permission from Sintef Energy AS, but is subject to the Confidentiality Agreement between the author and Sintef Energy AS. Chapter three is therefore not to be published publicly as part of the master thesis. The intention of including this chapter is to allow the sensors to understand how the VLE measurements have been conducted and connect this to Chapter four and five. This chapter can also be helpful for current and future researchers working for Sintef Energy AS on VLE measurement campaigns. The experimental apparatus is described in section 3.1 and the experimental procedures are described in section 3.2.

3.1 Experimental Apparatus

An overview of the lab area used for the experimental apparatus is given in figure 3.1. The bold lines mark the walls of room 4, while the stapled lines mark transparent cabinet walls enclosing ventilated areas. This is to minimize the risk in case of a gas leakage. The bottle cabinet with gas bottles, including methane, is located outside the room in a separately ventilated area. Room 4 is mainly divided into the three sections test chamber, mixing chamber and weigh chamber which is described in more detail below. In the lower left corner of the schematic overview in Figure 3.1 there is a tubing from the test chamber to the surrounding of room 4. This tube connects the test rig tubing system to the dead weight (DW) used for the pressure calibration described in section 3.2.1 and 4.1.2.

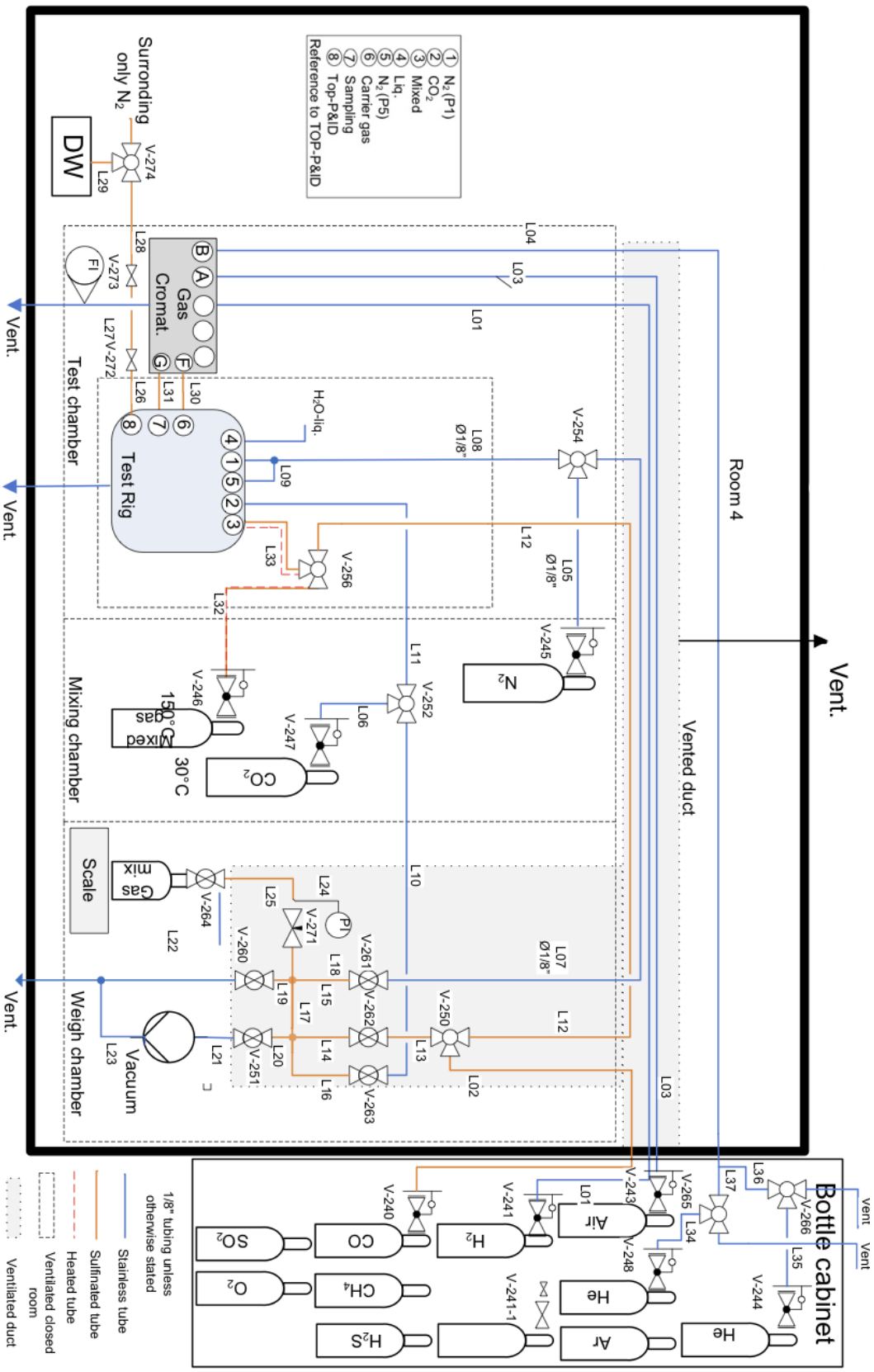

Figure 3.1: Overview of the lab area used for the experimental apparatus.

3.1.1 VLE/ Test Chamber

A schematic of the vapor-liquid test rig is shown in Figure 3.2. The cell itself is in the center of Figure 3.2. A more detailed picture of the cell with labeled key components can be found in Figure 3.3. The glass is made of sapphire and the flanges of titanium.The cell is designed for pressures up to 200 bar. The stirrer inside the cell enables mixing of the cell contents to reach VLE faster. The temperature sensors of the cell, two Standard Platinum Resistance Thermometers (see section 3.2.2 for more details), are located in the top (TE04) and bottom (TE05) flange. The bellows are located inside the upper part of the cell. Pump 1 is filled with nitrogen gas and controls the pressure in the bellows circuit directly and the volume of the bellows indirectly. The volume of the bellows can in turn be used to make small pressure adjustments in the cell (see section 3.2.4 for more details). The four manually operates valves, three in the top flange and one in the bottom flange, are connected to the surrounding tubing system and pumps. Pump 2, 3 and 4 are used to pump gas or liquid into the cell. Pump 2 is used for pure CO_2 gas and Pump 4 for any non-explosive liquid content. The valve in the bottom flange connects the cell to the vacuum pump in addition to pump 4. Pump 3 is usually filled with the impurity component(s), or a mixture of CO_2 and the impurity component(s). Pump 5 controls the pressure sensor circuit, connected to the absolute pressure sensors P1, P2, P3 and P4 and the right hand side of the differential pressure sensor P11. The left hand side of P11 is directly connected to the cell, and P11 therefore measures the pressure difference between the cell and the pressure circuit. Each of the the absolute pressure sensors have different pressure ranges (P1: 0-10 bar, P2: 0-30 bar, P3: 0-100 bar, P4: 0-250 bar) and are used in their respective ranges with corresponding accuracy (see section 4.2.2). The pressure circuit can also be connected to the dead weight for calibration measurements, but this is not marked on the simplified schematic. The dead weight is described in more detail in section 3.2.1. The cell is surrounded by a fluid bath, which has a stirrer and a temperature control function of its own. The bath is filled with a fluid suitable for the temperature range being measured, usually ethanol below 0 °C, water between 0 and 100 °C and silica above 100 °C. The small boxes marked LS and VS represent the liquid (L) and vapor (V) samplers. Each of these are connected to a thin capillary that extends into the cell. The vapor and liquid capillary ends close to the top and bottom of the cell, respectively. The samplers are used to take samples from the liquid and gas phase of the cell content and sends them to the gas chromatograph for analysis (see section 3.2.4). A Labview control system was developed through the project CO2Mix [3] to control all automatic valves, temperature regulators, stirrers and the sampling functions in addition to log all sensor readings. For the measurements at 298 K, a camera has been used to visually inspect the liquid level of the cell (see picture 3.4 for an example). However, the camera used does not withstand water or ethanol for long periods of time and was therefore only a temporary solution. Other options were tested, but the cameras were either poorly resistant to water and/or ethanol or gave pictures of low quality. A more permanent solution should be developed for future work to more easily and rapidly reach desirable VLEs during measurements. For the measurements at 223 K, 253 K, 273 K and 283 K the total composition of the cell and the liquid level were estimated approximately instead of visually. See section 3.2.4 for more details on this.

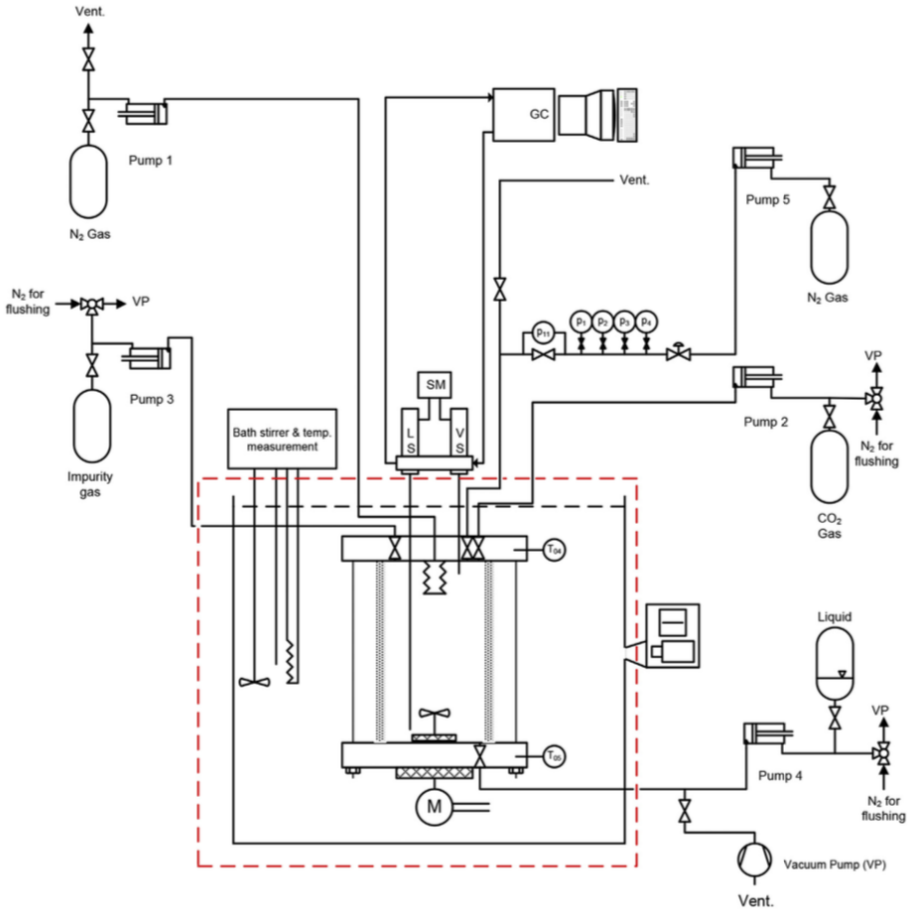

Figure 3.2: Simplified schematic overview diagram of the VLE rig.

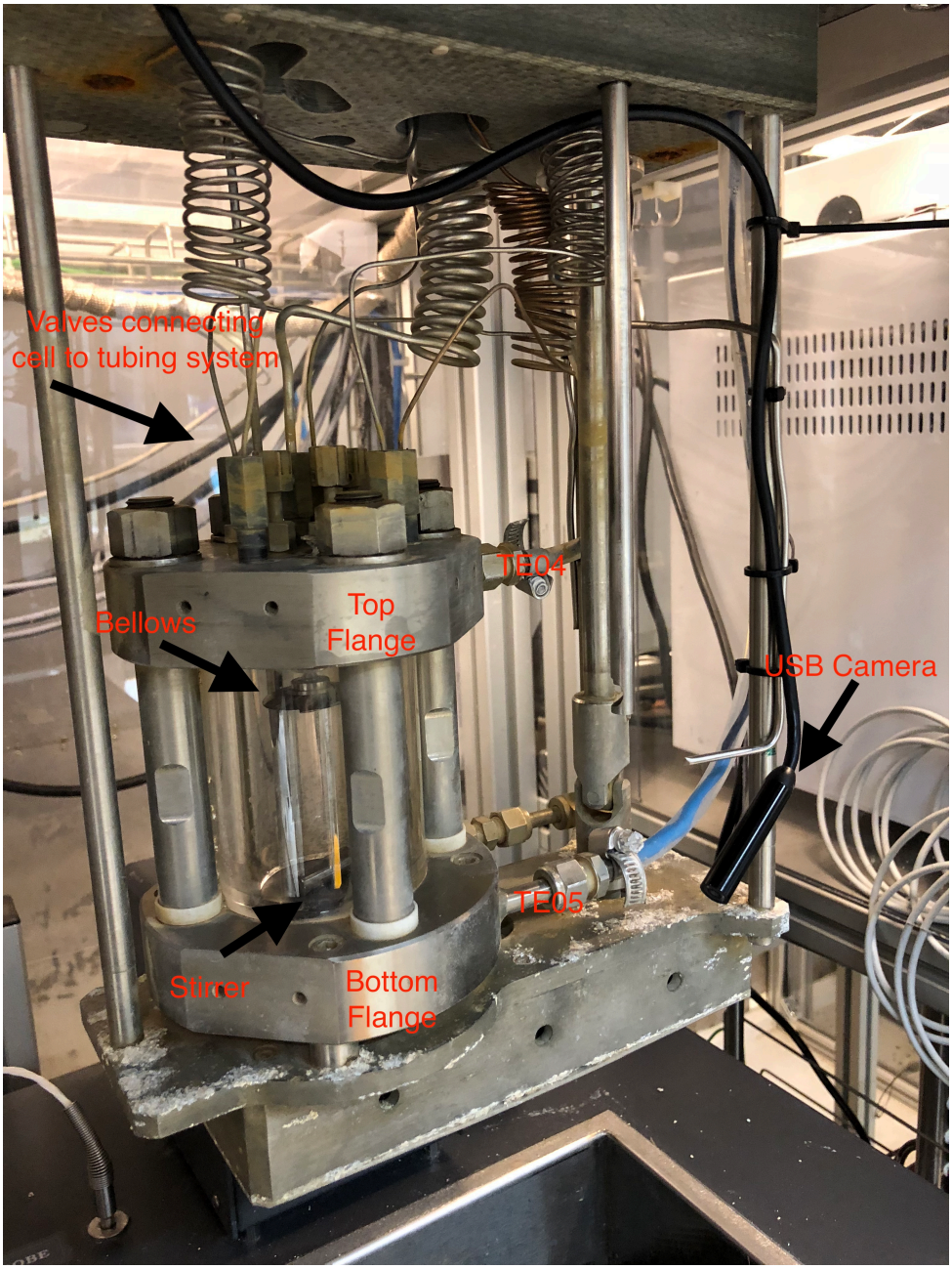

Figure 3.3: The vapor-liquid cell labeled with main components.

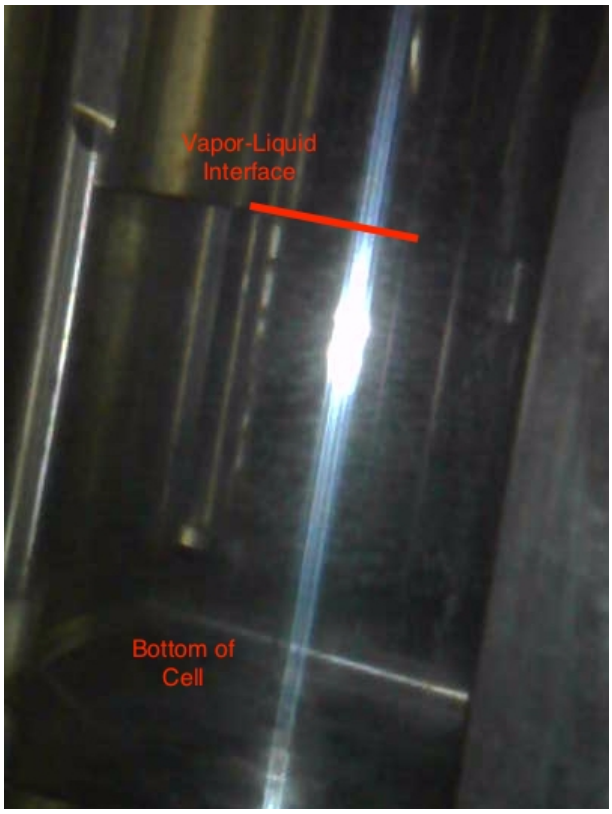

Figure 3.4: Picture of the cell filled with a mixture of CO_2, N_2 and CH_4. The vapor-liquid interface is marked with a red line.

3.1.2 Weight Chamber

To calibrate the gas chromatograph (GC), calibration gas mixtures with highly accurate known compositions (see section 3.2.3 and 4.1.3 for more details) are needed. To prepare these mixtures, an in-house gravimetrical set up was built in the weigh chamber through the project CO2Mix [3]. A picture of the set up is shown in Figure 3.5. The charging tube is connected to the source gas bottles and a vacuum pump to vacuum and fill the calibration gas bottle with the desired components. The procedure for gravimetrically preparing the calibration gas mixtures is described in section 3.2.3.

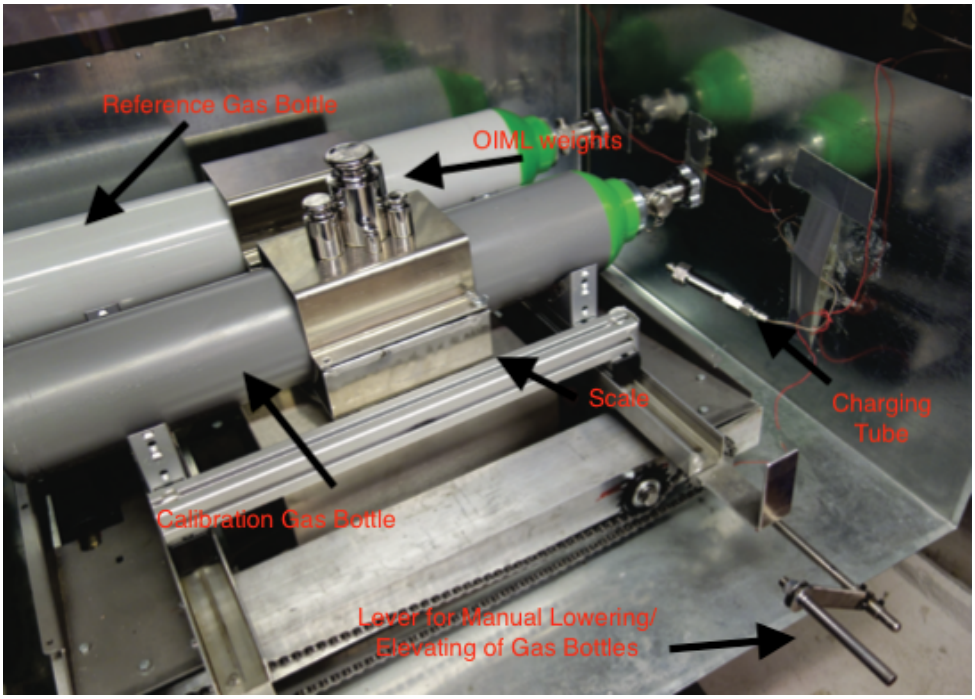

Figure 3.5: The set up for gravimetric preparation of the calibration gas mixtures.

3.1.3 Mixing Chamber

Inside the mixing chamber there is a custom built roller to mix the calibration gas mixtures properly before filling them onto the cell. The mixing chamber also contains source gas bottles of the two most used and non-explosive gases, CO_2 and N_2.

3.2 Experimental Procedures

This section describes the experimental procedures used during the project. Notice that the temperature and pressure calibration measurements were performed during the summer of 2018. However, the experimental procedures for these measurements are included because the analysis of the pressure and temperature values and uncertainties in the VLE measurements depend highly on these (see chapter 4 for more details). Calibration measurements of 5 out of 7 calibration gases were also performed from July 2018 to October as part of the summer internship and fall specialization project. Furthermore, the VLE measurements at the 298 K isotherm were performed in October and November 2018 as part of the fall specialization project.

3.2.1 Pressure Calibration Measurements

The four absolute pressure sensors P1, P2, P3 and P4 were calibrated to relate the sensor readings to the actual pressure measured. P1 was calibrated in 2015 by S.F. Westman and P2-P4 was calibrated in 2018. The calibration was done by connecting the pump 5 nitrogen circuit (see Figure 3.2), where all pressure sensors were connected, to the dead weight (see figure 3.6). The dead weight was used to measure the force applied to the scale. Certified weights were used to relate the scale reading to force for the pressure piston used. Three pressure pistons were used during the calibration measurements with pressure ranges 0-10 bar, 0-50 bar and 0-200 bar. Hence, piston 1 was used for pressures below 10 bar, piston two for pressures between 10 and 50 bar and piston three for pressures between 50 and 200 bar. The pistons also had a resistance with a known reference resistance at 0 °C to determine the temperature inside the piston. For each calibration measurement, the pressure circuit was filled to the desired pressure using pump 5 and stabilized. The pressure sensor readings were then logged together with the scale and resistance readings. The analysis of the calibration measurements and the construction of a calibration function for each of the pressure sensors can be found in section 4.1.2.

3.2.2 Temperature Calibration Measurements

To verify the current calibration of the two Standard Platinum Resistance Thermometers (SPRTs) located in the bottom and top flange of the cell (see figure 3.3), the triple point of water was measured. This was done by using a triple point cell for water, see the picture in Figure 3.7. Dry ice (Solid CO_2) was used to cool the cell from room temperature to the triple point of water, 273.16 K. It was ensured that the ice cap that formed inside the triple point cell covered the well (at the center of the cell) properly. The resistance of the SPRTs were measured indirectly by comparing the resistance of the SPRTs with the reference resistance of 24.998982 Ω in an ASL F650AC thermometry bridge. The resistance ratio of the SPRTs were logged for around 10 minutes after the resistance ratio had stabilized, keeping the SPRTs in the well of the triple point cell. See section 4.1.1 for the analysis of the calibration measurements.

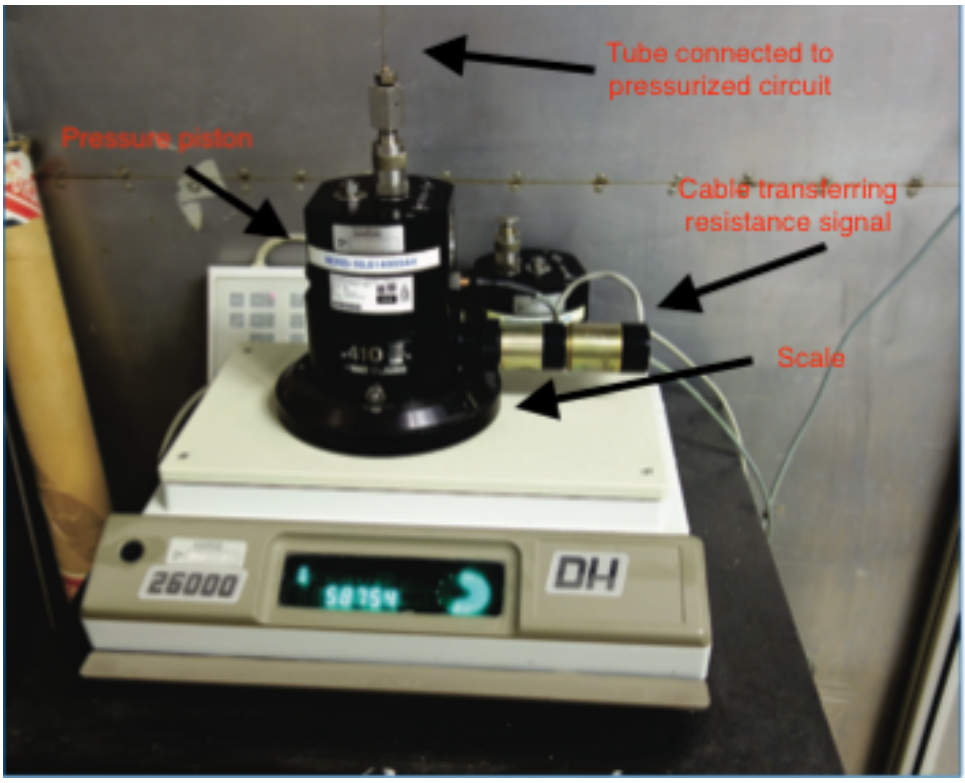

Figure 3.6: The dead weight used in the pressure calibration measurements.

Figure 3.7: Triple point cell for water.

3.2.3 Composition Calibration Measurements

To relate the output from the gas cromatograph (GC) to the composition accurately, a large amount of calibration measurements were needed. The analysis of the composition calibration measurements can be found in section 4.1.3. The experimental procedures to obtain these data are described below.

Gravimetric Preparation of the Calibration Gases

A gravimetric procedure was used to prepare 7 calibration gases with a highly accurately known composition. 10.0 L calibration gas bottles were emptied and evacuated to less than 20 Pa, to ensure negligible amounts of gases. The bottles were placed on the comparator together with

a reference gas bottle as shown in Figure 3.5. From now on, the bottles were handled very carefully to prevent scraping the bottles or leaving fingerprints. Next, weights certified by the International Organization of Legal Metrology (OIML) were placed on the lightest gas bottle, either the calibration or the reference gas bottle, to ensure a weight difference of less than 10 g. The reference and calibration gas bottle was then weighted using an "ABBA" weighting scheme 10 times. "A" was taken as the reference gas bottle and "B" as the calibration gas bottle in the weighting scheme. Thus, each bottle was weighted 20 times. To estimate the buoyancy force, the air density was estimated by measuring the dry bulb temperature, wet bulb temperature and atmospheric pressure before and after the weighing.

After determining the weight difference between reference and calibration gas bottle, the calibration gas bottle was filled with the desired amount of CO_2 through the charging tube. The tubing system between the charging tube and the source gas bottle was flushed and evacuated four times to prevent significant amounts of impurities to enter the calibration gas bottle. Subsequent to filling the bottle, the "ABBA" weigh scheme was applied again.

After determining the mass of CO_2, the calibration gas bottle was filled with either N_2 or CH_4. The component with the lowest desired mass was filled first. The filling was done similar to the filling of CO_2 for both N_2 and CH_4, except for extra safety precautions when filling methane due to the danger of explosion. The mass of each component was determined using the "ABBA" weighting scheme as described before. After all components had been filled into the calibration gas bottle and the mass of each component had been determined, the calibration gas bottles were rolled on the custom built roller in the mixing chamber for about one hour.

Filling of Bath

The fluid bath surrounding the cell was filled with clean water and the temperature was set to 40 °C. This was done to be able to take measurements at higher pressures without risking the calibration gas to split into two phases.

Flushing of Relevant Components

The calibration gas bottle was connected to the tubing system of the VLE test rig. The bottle regulator, the tubes being used, pump 3 and the cell was evacuated and flushed four times with the calibration gas to ensure negligible amounts of impurities. The vacuum pump was used for evacuation. For each new calibration gas that was connected the evacuation and flushing was repeated four times.

Filling of Cell and Sampling to GC

Subsequent to flushing and evacuating, pump 3 was filled with the calibration gas. It was then used to fill the cell to the desired pressure. After the desired pressure was reached, all manual valves connecting the cell to pump 3 and the vacuum pump were closed. Next, a flushing sample was taken with each sampler (see Figure 3.2 and section 3.1.1 for description of the location of these samplers). Finally, samples of desired sizes were taken with the two samplers. This procedure was repeated for all 7 calibration gas mixtures.

3.2.4 Vapor-Liquid Equilibrium Measurements

A flow sheet of the two different procedures used during the vapor-liquid equilibrium (VLE) measurements is presented in Figure 3.8. The procedure is described in more detail below.

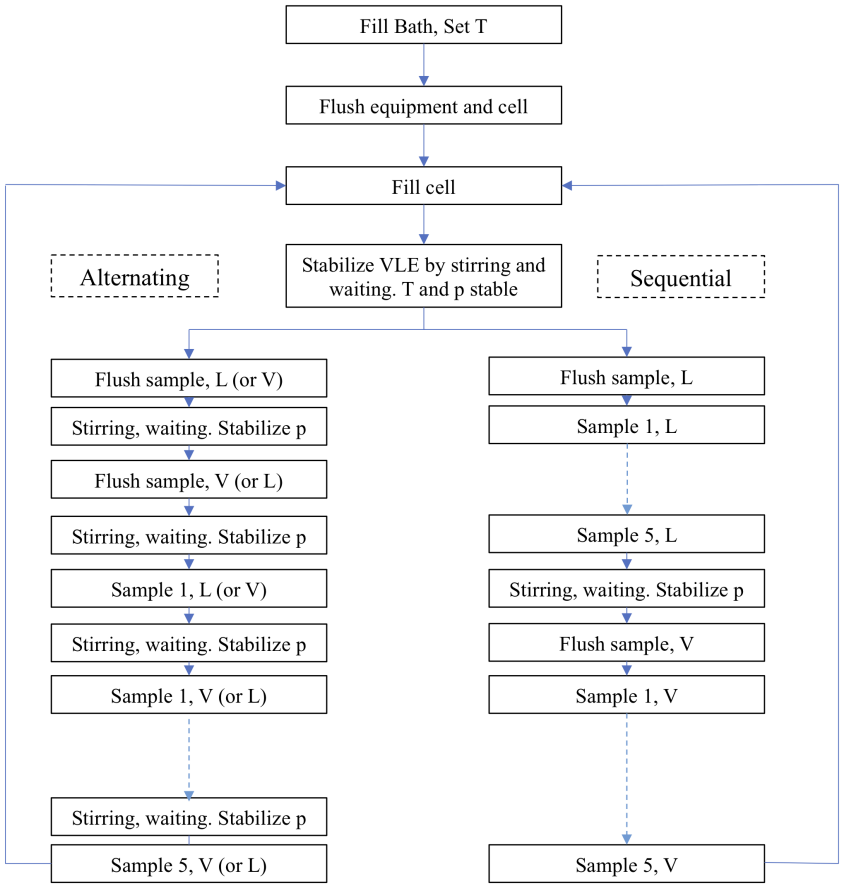

Figure 3.8: Flow sheet illustrating the experimental procedure of the VLE measurements.

Filling of Fluid Bath and Setting Bath Temperature

Depending on the desired temperature of the VLE measurements, the fluid bath was filled with a suitable fluid. Water was chosen for the 283 K and 298 K isotherms and ethanol for the 223 K, 253 K and 273 K isotherms. After filling the bath with the fluid, the desired temperature was set. It was verified that the temperature had reached the set point by using the SPRTs and the calibration function as described in section 4.1.1.

Flushing Regulators, Tubes, Pumps, and Cell

In the same way as for the composition calibration measurements, the gas bottle regulators, tubes, pumps and the cell were flushed and evacuated 4 times before use. Pump 2 was filled with CO_2 and was therefore also flushed with CO_2. Pump 3 was filled with a desired calibration gas to mix with the pure CO_2 in the cell. Hence, the total composition in the cell could be varied by filling mixed gas from pump 3.

Filling of Cell

The cell was flushed with pure CO_2 from pump 2 before an isotherm was started. Next, it was filled with CO_2 to the saturation pressure and a liquid level significantly above the stirrer to ensure that the liquid sampler was below the liquid surface. The temperature and pressure were measured to verify that the sensor readings were in agreement with literature data within the uncertainty of the measurement. See section 4.2.3 for results of the saturation pressure measurements. Two samples were also taken on each sampler to verify that the cell content was pure CO_2. See below for details on temperature, pressure and composition measurements.

To reach a new equilibrium state, gas was filled from pump 2 and 3 depending on the desired state. The filling was done in intervals, mixing with the stirrer at 400 rpm in between, to prevent the state of the mixture to move outside the two phase region. When the desired pressure was reached, it was verified that the mixture was in the two phase region. For the measurements at 298 K, this was done visually using the USB camera to locate the liquid interface. For the other isotherms, a test sample was taken at each of the samplers and analyzed (see section 4.1.3 for details on the sample analysis) to verify that the composition was significantly different in the two phases. If the composition was not significantly different, it was assumed that the mixture had moved outside the two phase region, and the cell was emptied and filled again with adjusted amounts of CO_2, N_2 and CH_4.

VLE Stabilization

To ensure that the mixture had reached equilibrium, the stirrer was run at 400 rpm until the pressure was stable within 10 mbar. Depending on the pressure, temperature and composition the stabilization took from 15 minutes to 3 hours. If the mixture was closer to the critical point it typically took more time to stabilize. After stirring, the mixture was left to settle for at least 20 minutes.

Temperature Measurement

The temperature was measured indirectly through the measurement of the resistance in two Standard Platinum Resistance Thermometers (SPRTs) located in the bottom and top flange of the cell, see Figure 3.3. The SPRTs were connected to an ASL F650AC Thermometry Bridge, and the ratio between the SPRTs and a reference resistance of 24.998982 Ω (Tinsley 5685A external resistance normal) was logged. A calibration function was fitted as described in section 4.1.1 to relate the resistance ratio to the temperature.

Pressure Measurement

The pressure in the cell was taken as the sum of the differential pressure sensor P11, p_{diff}, the most accurate absolute pressure sensor (P1,P2,P3 or P4), p_i and the hydrostatic pressure, p_{hs}, between the differential sensor and the liquid interface in the cell. Further details on the hydrostatic pressure can be found in section 4.2.2. For the absolute pressure sensors, P1 was used for pressures below 10 bar at the 223 K isotherm, P2 was used for pressures between 10 bar and 30 bar at the 223 K and 253 K isotherms and P3 for all measurements at the 253K, 273 K, 283 K and 298 K isotherms above 30 bar. To measure the differential pressure accurately, pump 5 was used to control the pressure of the pump 5 nitrogen pressure circuit such that the

differential pressure reading of P11 was stable at less than 10 mbar. To ensure this stability, pump 5 was filled to more than 90 vol%. Thus, the pressure response to a volume change in the pump volume was small.

Composition Measurement

When the VLE and the differential pressure had been stabilized, the rig was ready to take samples using the vapor and liquid samplers. The samples were heated to 150 °C to ensure vapor phase and transported by the carrier gas Helium into a Supelco column to separate the components. The GC recorded the conductivity of the gas sent through the Supelco column as a function of time and stored this as output. A 40 minute program was used for all measurements. The GC output was analyzed as described in section 4.1.3.

Sampling

The bellows, see Figure 3.3, have previously been used to compensate for the pressure change caused by a sample. Since the bellows were damaged during the first weeks of the project and the delivery time of new bellows were long, all measurements had to be done without the use of the bellows. Hence, the pressure changed slightly after each sampling.

Two different sampling strategies, alternating and sequential, were used for the VLE measurements during the project period. Samples L1/V1 to L10/V10 were taken using an alternating sampling scheme and the rest using the sequential sampling scheme.

For the samples taken with an alternating sampling scheme, the stirrer was used between each sampling and it was sampled alternating from the liquid and vapor sampler. It was stirred until the pressure was stable within 10 mbar and at least 15 minutes. The cell content was then left to settle potential droplets for at least 20 minutes. Since a 40 minute program was used, the minimum time between each sample was 40 minutes. However, pressure stabilization was slower closer to the critical point and more stirring time was often needed. At least 6 samples were taken at each sampler, where the first sample was considered as a flushing sample.

For the samples taken with the sequential scheme, 6 samples with 42 minute intervals were taken with the liquid sampler without stirring between each sample. The cell content was then stirred for at least 15 minutes until the pressure was stable within 10 mbar and left to settle for at least 20 minutes. Finally, 6 samples were taken with the vapor sampler without stirring between each sample. See the flowsheet in Figure 3.8 for an overview of the experimental procedures.

Chapter 4

Analysis

This chapter includes details on the analysis of the VLE measurements, including calibration of temperature sensors, pressure sensors, and the gas chromatograph (section 4.1). Furthermore, it includes a quantitative uncertainty analysis of the measured quantities pressure, temperature and composition (section 4.2). Additionally, it describes the development of a tool to visualize the residual Helmholtz energy prediction by the EOS-CG 2019 model (section 4.3).

4.1 Calibration

4.1.1 Temperature

A calibration function was needed for the isotherms 223 K, 253 K, 273 K, 283 K and 298 K. It was decided to use the International Temperature Scale of 1990 (ITS-90) [36]. For temperatures between 13.8 K and 273.16 K the reference function was defined as:

$$T_{90}/273.16\ \mathrm{K} = B_0 + \sum_{i=1}^{9} B_i \left[\frac{W_r(T_{90})^{1.6} - 0.65}{0.35}\right]^i \tag{4.1}$$

and for temperatures between 273.15 K and 688.63 K the reference function was defined as:

$$T_{90} = 273,15\ \mathrm{K} + D_0 + \sum_{i=1}^{9} D_i \left[\frac{W_r(T_{90}) - 2.64}{1.64}\right]^i \tag{4.2}$$

In both functions $W_r(T_{90})$ is the reference resistance ratio given in equation 4.3. It is based on the triple points of mercury and gallium through the coefficients A_p and B_n given in equation 4.5 and 4.4. The reference resistance ratio between mercury and its triple point, $W_{Hg,r}$, and gallium and its triple point, $W_{Ga,r}$, are defined as $W_{Hg,r}$=0.8441421 and $W_{Ga,r}$=1.1181389 from ITS-90. The coefficients B_0 to B_9 and D_0 to D_9 are given in ITS-90. $W(T_{90})$ is the ratio between the sensor resistance at a given temperature T_{90} and the sensor resistance measured at the triple point of water, as stated in equation 4.6. The sensor resistance was measured indirectly by measuring the ratio, W_{bridge}, between the reference resistance,R_{ref}=24.998982 Ω, and the sensor resistance $R_{T_{90}}$.

$$W_r(T_{90}) = W(T_{90}) - A_p[W(T_{90}) - 1] - B_n[W(T_{90}) - 1]^2 \tag{4.3}$$

$$B_n = \frac{(W_{Hg} - W_{Hg,r}) - (W_{Ga} - W_{Ga,r}) + W_{Hg,r}W_{Ga} - W_{Ga,r}W_{Hg}}{(W_{Hg} - 1)^2 - (W_{Ga} - 1)^2 + W_{Hg}(W_{Ga} - 1)^2 - W_{Ga}(W_{Hg} - 1)^2} \tag{4.4}$$

$$A_p = \frac{W_{Hg} - W_{Hg,r} - B_n(W_{Hg} - 1)^2}{W_{Hg} - 1} \tag{4.5}$$

$$W(T_{90}) = \frac{R(T_{90})}{R(T_{90} = 273.16\ \mathrm{K})} \tag{4.6}$$

$$R(T_{90}) = W_{brige}R_{ref} \tag{4.7}$$

The arithmetic mean of the computed temperatures of the two sensors TE04 and TE05 was taken as the best estimate of the cell temperature:

$$T = \frac{T_{04} + T_{05}}{2} \tag{4.8}$$

The triple points of mercury, gallium and water had been measured in 2014. To verify that the calibration was still valid for the project period June 2018 to June 2019, the two sensor resistances were measured again at the triple point of water. The results are presented in table 4.1. A deviation of 5e-06 represents a deviation between the 2014 and 2018 measurement of around 1 mK. It was therefore concluded that the calibration was valid, but the calibration function was adjusted with the resistance ratio values from 2018.

Table 4.1: Calibration measurements of the triple point of water.

Temp. Sensor	W_{bridge}, 2018	W_{bridge}(2018) - W_{bridge}(2014)
TE04	1,0154910	5.3158e-06
TE05	1,0178081	4.8908e-07

4.1.2 Pressure

As described in section 3.2.1, the absolute pressure sensors were calibrated by recording the sensor reading and comparing it to a dead weight reading. The temperature in the dead weight was measured indirectly by measuring the resistance of a resistor located inside the pressure piston. The relation between temperature and resistance can be seen in equation 4.9, the Callendar-Van Dusen equation [37]. Transformed into an explicit expression for temperature it can be restated as in equation 4.10. The constants A ($3.9083 \cdot 10^{-3}$ °C^{-1}) and B ($-5.77 \cdot 10^{-3}$ °C^{-2}) are stated in the Van Dusen article [37]. R_0 is the measured resistance of the sensor at 0 °C.

$$R(T) = R_0(1 + AT + BT^2) \tag{4.9}$$

$$T = \frac{-A - \sqrt{A^2 - 4B(1 - \frac{R_T}{R_0})}}{2B} \tag{4.10}$$

The air density was estimated by measuring the dry bulb temperature, T_{dry}, the atmospheric pressure, p_{atm} and the air humidity ϕ [38]:

$$\rho_{air} = \frac{ap_{atm} - (b + cT_{dry} + dT_{dry}^3)\phi}{T_{dry} + 273.15\ \text{K}} \tag{4.11}$$

with the constants $a = 3.48488$, $b = 8.0837$, $c = 0.7374$ and $d = 0.00097525$ [38]. The measured piston temperature, T, the recorded scale reading, U_{scale}, the air density, ρ_{air} and a piston specific force constant K_N were used to compute the reference pressure with an equation provided by the producer of the dead weigh system:

$$p_{ref} = K_N \frac{U_{scale}}{Nk} \frac{G_L}{G_N} (1 - \alpha_{PC}(T - 20K)) \frac{\rho_{air} - \rho_{OIML}}{\rho_{air,N} - \rho_{OIML}} (1 - \lambda p) + ... \\ p_{atm} - \rho_{\mathrm{N}_2} G_L \Delta_{H,sensor} \tag{4.12}$$

G_L and G_N are the local and nominal gravity, ρ_{OIML}=8000 kg/m^3 is the density of the calibration OIML weights and α_{PC}=9.0 $\cdot 10^{-6}$ 1/K, N_k=10000 counts/kg, λ=-3.44 $\cdot 10^{-7}$ 1/bar and $\rho_{air,N}$=1.2 kg/m^3 were constants specified by the producer. The pressure in the piston, p, was taken as the sensor reading pressure as this was approximately equal to the reference pressure. It was verified that using this approximate pressure in equation 4.12 had negligible effect on the calibration result. $\Delta_{H,sensor}$ is the measured height difference between the absolute pressure sensors and the dead weight and ρ_{N_2} was the density of nitrogen computed with the EOS for pure nitrogen [39].

A linear regression relating the reference pressure to the sensor reading was performed for each sensor. As mentioned in section 3.2.1 P2, P3 and P4 were calibrated in 2018 while P1 was calibrated in 2015 by Snorre F. Westman. The reason for this was that there were no VLE measurements planned below 10 bar at the beginning of the project period. It was later determined to measure at 223 K and pressures below 10 bar after a meeting with the industry partners in spring 2019, and the calibration function from 2015 for P1 was then used. The calibration functions are given in equation 4.13, with p being the absolute pressure and p_i the measured pressure at the pressure sensor. The residuals between the fitted pressure and the measured reference pressure for the four calibrations are plotted in Figure 4.1. The accuracy of the pressure measurements are discussed more in the uncertainty analysis in section 4.2.2.

$$\begin{aligned} p &= 1.003039p_1 - 0.003386, p \in [0\ \text{bar}, 10\ \text{bar}] \\ p &= 1.001754p_2 + 0.004091, p \in [10\ \text{bar}, 30\ \text{bar}] \\ p &= 1.000069p_3 + 0.015228, p \in [30\ \text{bar}, 100\ \text{bar}] \\ p &= 1.002157p_4 + 0.068321, p \in [100\ \text{bar}, 200\ \text{bar}] \end{aligned} \tag{4.13}$$

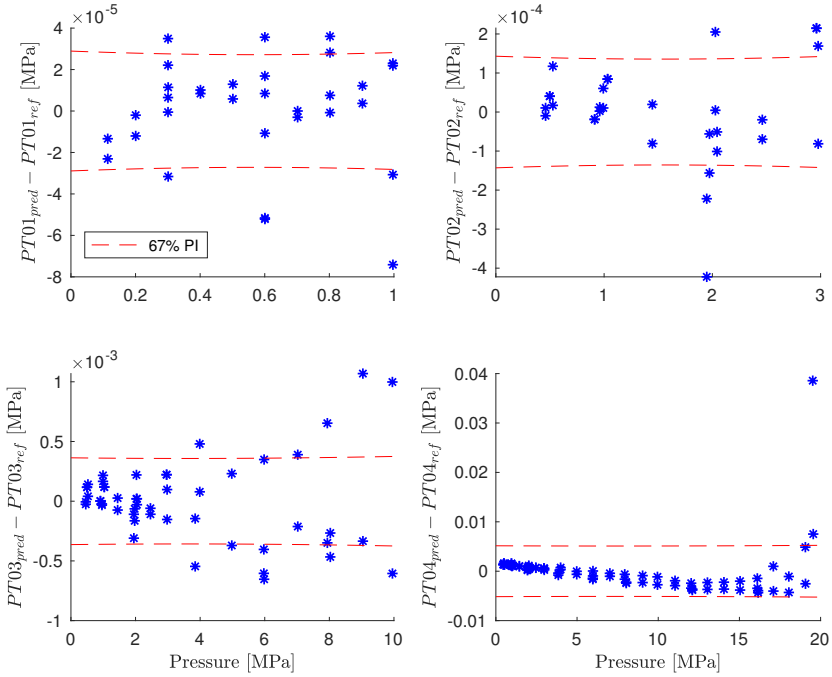

Figure 4.1: Residual plots for the four pressure sensor calibrations.

4.1.3 Composition

Gravimetric Preparation of Calibration Gases

A total of 7 calibration gas mixtures were prepared to calibrate the gas chromatograph (GC) as described in section 3.2.3. The calibration gas compositions were determined to span out the relevant composition range for the planned measurements. The approximate composition of the calibration gases on a $z_{\mathrm{N_2}}$-$z_{\mathrm{CH_4}}$ grid is illustrated in Figure 4.2. The mass of each component was computed using equations 4.14 for CO_2 and 4.15 for N_2 and CH_4. $m_{0\Delta BA}$, $m_{1\Delta BA}$, and $m_{k\Delta BA}$ are the weight difference between the calibration gas bottle and the reference gas bottle before filling of CO_2, after the filling of CO_2 and after the filling of component k, respectively. $\rho_{air,k}$, V_{AK},V_{Bk}, $m_{OIML,Ak}$, and $m_{OIML,Bk}$ are the air density, volume of the weights on the reference gas bottle, volume of the weights on the calibration gas bottle, mass of weight on the reference gas bottle and mass of weight on the calibration gas bottle during weighting k.

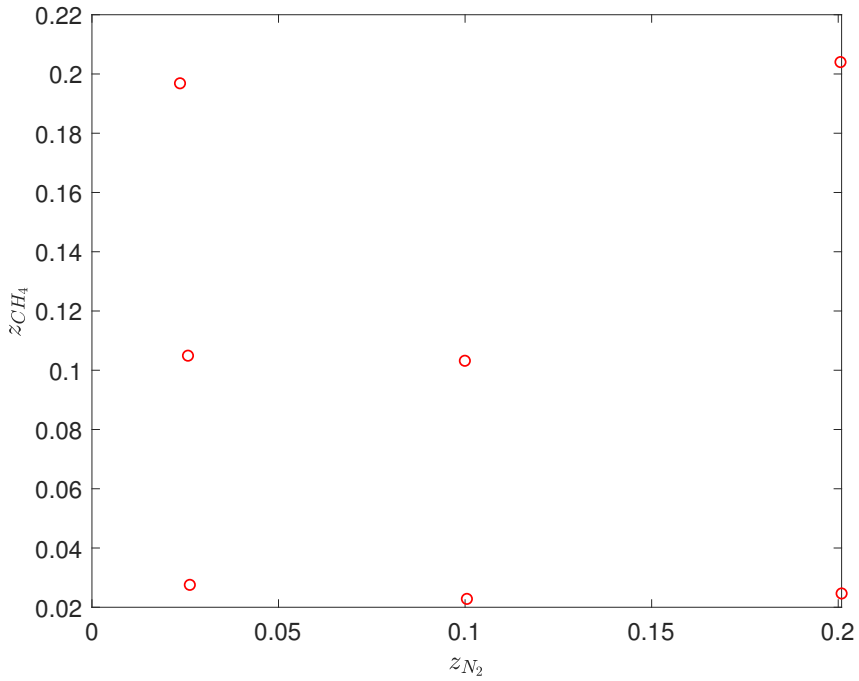

Figure 4.2: Overview of the composition of gravimetrically prepared calibration gases. Mole fraction of methane and nitrogen on y- and x-axis respectively. Mole fraction of CO_2 is implicit, with the most and least CO_2-rich mixture in the lower left and top right corner respectively.

$$m_1 = m_{1\Delta BA} - m_{0\Delta BA} + \rho_{air1}V_B1 - \rho_{air1}V_{A1} - (\rho_{air0}V_{B0} - \rho_{air0}V_{A0}) + (m_{OIML,A1} - m_{OIML,A0}) - (m_{OIML,B1} - m_{OIML,B0}) \quad (4.14)$$

$$m_i = m_{k\Delta BA} - m_{0\Delta BA} + \rho_{air,k}V_Bk - \rho_{air,k}V_Ak - (\rho_{air,0}V_B0 - \rho_{air,0}V_{A0}) + (m_{OIML,Ak} - m_{OIML,A0}) - (m_{OIML,Bk} - m_{OIML,B0}) - m_1 \quad (4.15)$$

The number of moles of each component, n_i, was computed by dividing the mass, m_i with an estimated effective molar mass $M_{i,eff}$:

$$n_i = \frac{m_i}{M_{i,eff}} \tag{4.16}$$

The molar composition of the calibration gas could then be defined by the definition in equation 4.17:

$$y_i = \frac{n_i}{\sum_{j=1}^{j=3} n_j} \tag{4.17}$$

The effective molar mass of component i was estimated from the source gas specifications of the component, as given in equation 4.18 and 4.19. M_{i+imp} is the average molar mass of the source gas, based on the impurity specification given by the producer of the source gas. The j-index runs over all impurity components in the source gas. A detailed discussion on the standard uncertainty of the calibration gases can be found in the report from the summer job 2018 [40].

$$M_{i+imp} = y_i M_i + \sum_j y_j M_j \tag{4.18}$$

$$M_{i,eff} = \frac{M_{i+imp}}{y_i} \tag{4.19}$$

Table 4.2: CO_2-N_2-CH_4 calibration gas mixtures with standard uncertainty in composition.

$y_{\mathrm{CO_2,cal}}$	$y_{\mathrm{N_2,cal}}$	$y_{\mathrm{CH_4,cal}}$	$u_{\mathrm{c}}(y_{\mathrm{cal}})$
0.946202	0.026235	0.027563	8.9e-6
0.779538	0.023602	0.196858	6.8e-6
0.781825	0.194323	0.023850	7.1e-6
0.876690	0.100485	0.022825	8.1e-6
0.796861	0.099939	0.103199	7.2e-6
0.595368	0.200607	0.204021	6.8e-6
0.869339	0.025740	0.104920	9.4e-6

GC Sample Size Planning

During the measurement of VLE points it was ensured that the sample size was large enough to flush the sampler capillaries entirely. This was done to prevent left overs from a previous equilibrium composition. Since the mass or volume of the sample could not be measured directly, an approximate linear function was previously made at Sintef:

$$\begin{aligned} A_{CO2} &= (b + a x_{CO2}) n_{CO2} \\ a &= 1.156 \cdot 10^{16} \\ b &= 7.639 \cdot 10^{15} \end{aligned} \tag{4.20}$$

Equation 4.20 relates the area under the CO_2-peak of the GC output to the mole and mole fraction of CO_2. An example of a typical GC output from a sample is given in Figure 4.3, where the three peaks origin from the three components N_2, CH_4 and CO_2 respectively. The integration

procedure to find the area under each peak is described under ”GC Output Integration Procedure” below. Using equation 4.20, the needed peak area of CO_2 to flush the sampler capillaries could be estimated. During the VLE measurements, an approximate peak area needed to flush the capillaries was computed. This was done using equation 4.21 and approximate estimation of the density of the sampler using EOS-CG. As a worst case estimate pure CO_2 was assumed to ensure that the samples were larger than the minimum size needed to flush the capillary. Notice that the dimensions of the two capillaries were different ($r_{liq} = 75 \cdot 10^{-6}$, l_{liq} = 0.4 m,$r_{vap} = 75 \cdot 10^{-6}$, l_{vap} = 0.3 m) as the liquid capillary stretched to the bottom of the cell.

$$n_{CO2} = \pi r^2_{sampler} l_{sampler} \rho_{sampler} \tag{4.21}$$

It was then ensured, after sampling and integrating the GC output, that the peak area and thus the sample size was large enough. If not, the sample size was increased. The calibration measurements were planned to span out the needed areas of all VLE measurements down to a temperature of 250 K. The most dense mixture would be pure liquid CO_2, and as a worst case estimate the density at 250 K, 1032 kg/m^3, was used. It was later decided to carry out some measurements at 223 K, and it was found that the sample sizes needed here were also spanned by the calibration function. Using a maximum density of 1032 kg/m^3 the maximum needed CO_2 peak area was computed to be 3.4 $\cdot 10^9$ 25 μVs. The calibration measurements of each calibration gas was therefore planned to span out the range from 0 to 3.4 $\cdot$ 10^9 25 μVs. The unit of the peak area origins from the GC output, conductivity in 25 μV versus time in seconds. 5 repetitions were taken at 6 different area responses for each of the seven calibration gases, a total of 210 calibration measurements at each sampler. See the ”Calibration Function” section for the results of the calibration measurements.

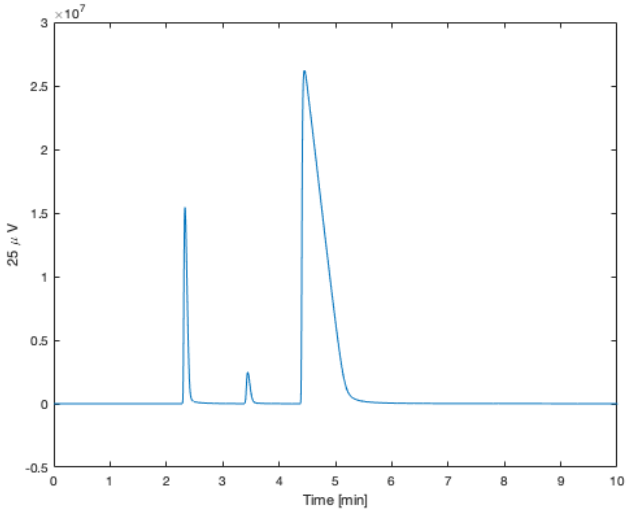

Figure 4.3: Example of a typical output from the GC. Measured voltage of the gas stream plotted versus time. The conductivity of the carrier gas has been calibrated to zero. The three peaks origins from the mass of N_2, CH_4, and CO_2 from left to right, respectively.

GC Output Integration Procedure

To accurately determine the area under each peak an integration procedure was developed. The procedure was based on previously used procedures by Sintef to analyze results for binary

mixtures. Since the GC output in general consisted of three peaks instead of two, extensive changes were made to make the code generic for n peaks. To ensure that the integration was done correctly, the code was designed to generate plots of the peaks. An example of a GC output is given in Figure 4.3. First, the start of every peak was determined and showed in a plot, see Figure 4.4 for an example. The start of the peak was set well before the output started to increase to ensure that the entire peak area was included. Next, the tail region of the two first peaks were determined and an exponential function fitted to the tails. A logarithmic plot of the tail region is shown in Figure 4.5. All the peak tails had a similar shape in the logarithmic space. Figure 4.5 shows that the tail can be divided into two regions with different slope in the linear space. By tuning some parameters manually, the start of the second region was determined and the end of the region was set to the start of the next peak, see Figure 4.6. An exponential function of the form given in equation 4.22 was fitted. The tail fit, extrapolated outside the fitting region in both directions, can also be seen in Figure 4.6. As can be seen in the Figure, the fit was usually very accurate in the fitted region. However, the fit was not as accurate before the start of the fitting region where the slope of the logarithmic GC response changes. A better fit here was not necessary since the region before the interference with the next peak was the main interest. The tail area, given that the next peak hadn't interfered, could then be estimated and added to the peak area. The same tail area was subtracted the next peak to account for the same interference.

$$\hat{f} = b_1 e^{-b_2(t-t_{fit,start})} \tag{4.22}$$

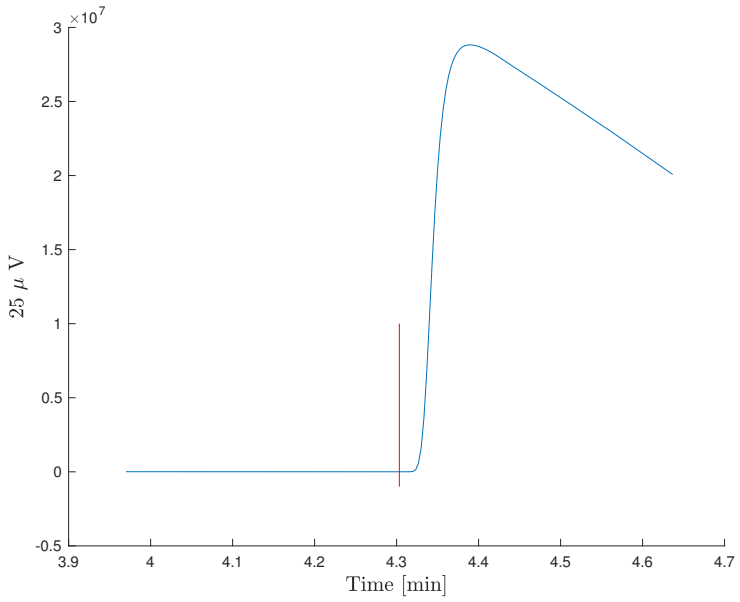

Figure 4.4: Plot showing the GC response (blue) and the determination of the start of the CO_2 peak (red).

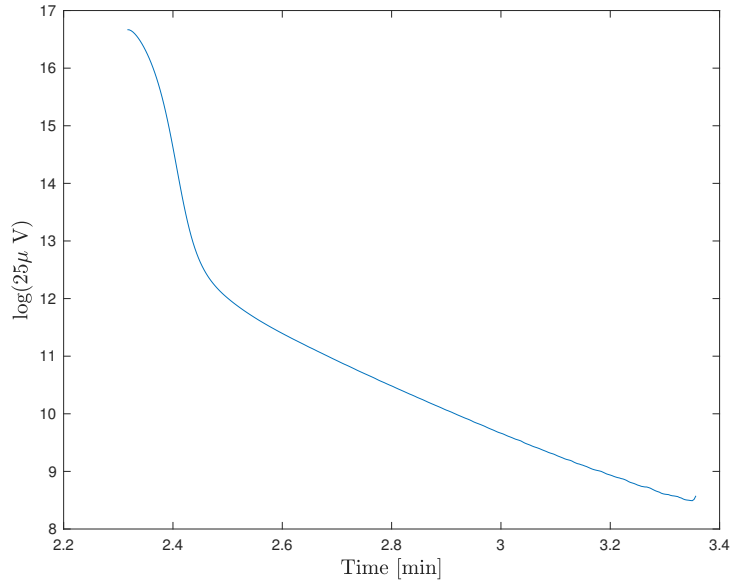

Figure 4.5: The logarithmic value of the GC response for the tail of the N_2 peak, illustrating the linear response in logarithmic space in the tail region. This region can be fitted accurately by an exponential function in the linear space.

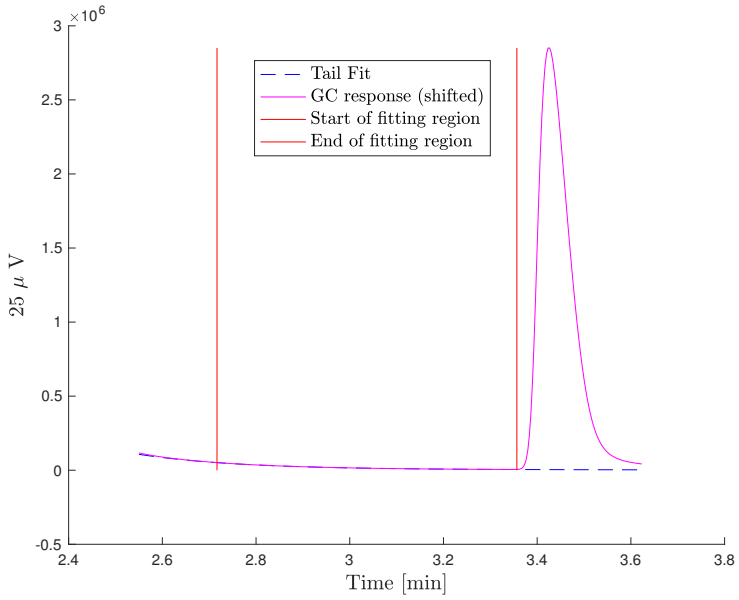

Figure 4.6: The tail region of the same N_2 peak as in Figure 4.5 plotted in linear space, showing the GC response (magenta), determined limits of the fitting region (red) and the tail fit (stapled blue).

Calibration Function

30 calibration measurements were taken of each of the 7 calibration gases with composition as given in table 4.2, with 5 repetitions at 6 different area responses for each sampler. The calibration measurements were fitted to a non linear function form given in equation 4.23.

$$\begin{aligned} k\hat{n}_{\mathrm{CO_2}} &= A_{\mathrm{CO_2}} + 0.001c_1 A_{\mathrm{CO_2}}^{c_2} + c_3 A_{\mathrm{N_2}} \\ k\hat{n}_{\mathrm{N_2}} &= c_4 A_{\mathrm{N_2}} + 0.001c_5 A_{\mathrm{N_2}}^{c_6} \\ k\hat{n}_{\mathrm{CH_4}} &= c_7 A_{\mathrm{CH_4}} + 0.001c_8 A_{\mathrm{CH_4}}^{c_9} \\ y_i &= \frac{k\hat{n}_i}{\sum_{j=1}^{j=3} k\hat{n}_j} \end{aligned} \tag{4.23}$$

The parameters were fitted separately for the liquid and vapor sampler, using the area responses of the GC for the respective samplers. A least squares approach was used to fit the optimal parameters, minimizing the residual function given in equation 4.24 using Matlab.

$$S(\boldsymbol{c}) = \sum_{series} \sum_{j=1}^{n=3} \left(\frac{y_{j,cal} - \bar{\hat{y}}_j}{\sqrt{u_c^2(y_{cal}) + s^2(\bar{\hat{y}}_j)}}) \right)^2 \tag{4.24}$$

$y_{j,cal}$ is the mole fraction of component j determined in the gravimetric analysis,$\bar{\hat{y}}_j$ is the average predicted mole fraction of component j in the given series, $s^2(\bar{\hat{y}}_j)$ is the variance of the predicted average mole fraction of component j in the given series and $u_c^2(y_{cal})$ is the combined standard uncertainty in the composition of the gravimetrically prepared calibration gases. Each series summed over consisted of 5 repetitions with approximately the same area output of the GC. Hence, the optimization problem weighted measurements with low uncertainties and low variances the most. Different function forms were tested, but the form stated in equation 4.23 was found to give the lowest residuals between gravimetrically estimated compositions and the fitted compositions. For the function fitted to the vapor sampler, a weight of 4.5 was added to the residual of the measurement series of the 60-20-20 mole% CO_2-N_2-CH_4 calibration gas. The reason for this was that the fitting routine had trouble finding a solution that had reasonably random residuals as a function of composition for the vapor samples, since 60-20-20 mole% CO_2-N_2-CH_4 is the only calibration gas with 40 mole% CO_2. It was therefore found that the fit was significantly better for lower fractions of CO_2 due to more calibration measurements in this composition region. Thus, a weight of 4.5 was added to the 60 mole% CO_2 calibration gas measurements. For the liquid sampler it was also tested adding weights to the 60-20-20 CO_2-N_2-CH_4 calibration gas measurements, but it did not have any significant effect here. The fitted parameters are summarized in table 4.3.

Parameter	Liquid Sampler	Vapor Sampler
c_1	2.782E-04	1.058E-04
c_2	1.569	1.616
c_3	1.443	1.722
c_4	-1387.681	-1219.920
c_5	0.907	0.955
c_6	1.355	1.374
c_7	7.400	6.595
c_8	1.174	1.174
c_9	-6.220	-6.898

Table 4.3: Fitted parameters to the component calibration function given in equation

Residual plots of the fitted calibration measurements versus the composition are shown in Figures 4.7 and 4.8. A small trend in increasing residuals in the methane composition can be seen for both the liquid and vapor sampler. Cross terms between methane and carbon dioxide and nitrogen were tested out to check if the trend in these residuals could be modeled. However, these cross terms lead to significant increases in the overall residuals and were therefore not used. The cross term between CO_2 and N_2 was added for both the liquid and vapor functions, because of a strong trend with increasing residuals in increasing N_2 mole fraction. Figures with residuals plotted versus area output from GC can be found in the appendix. These plots show clear trends in residual as a function of the GC area output for the different calibration gases. However, a common trend that could be modeled among all the calibration gases was not found. To prevent the model from becoming too complicated with only 42 different measurement series, only the 9 parameters showed in equation 4.23 were adjusted.

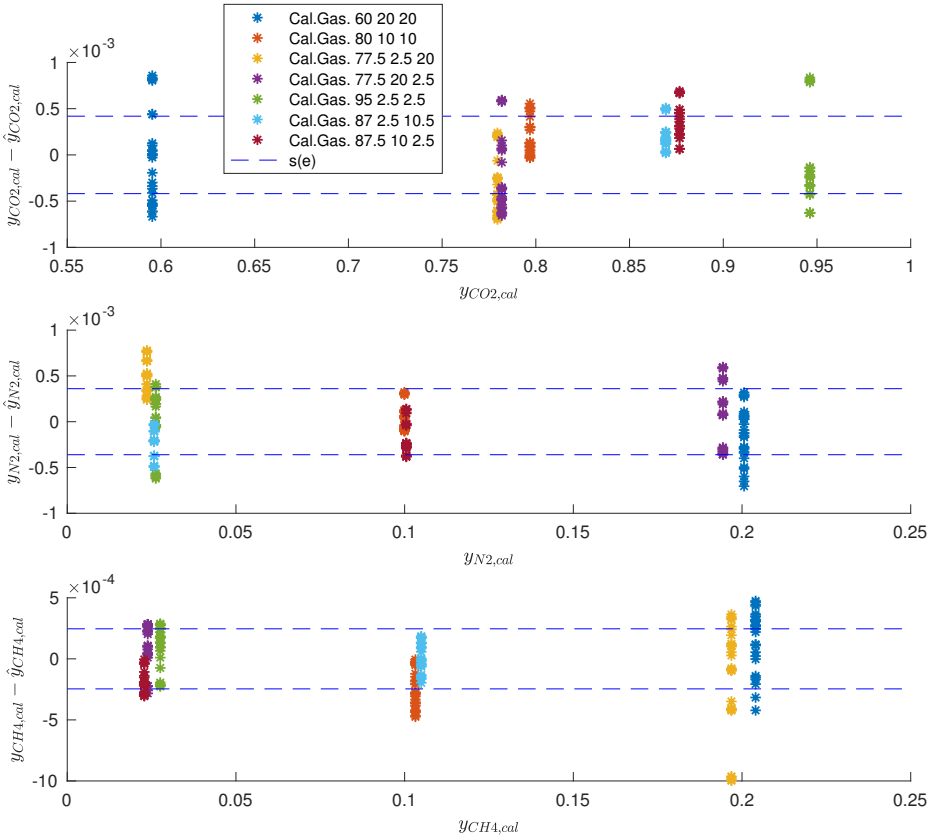

Figure 4.7: Residuals between fitted composition calibration function for the liquid sampler and the gravimetrically determined composition of the 7 calibration gases plotted versus mole fraction of CO_2 (top), N_2 (middle) and CH_4 (bottom).

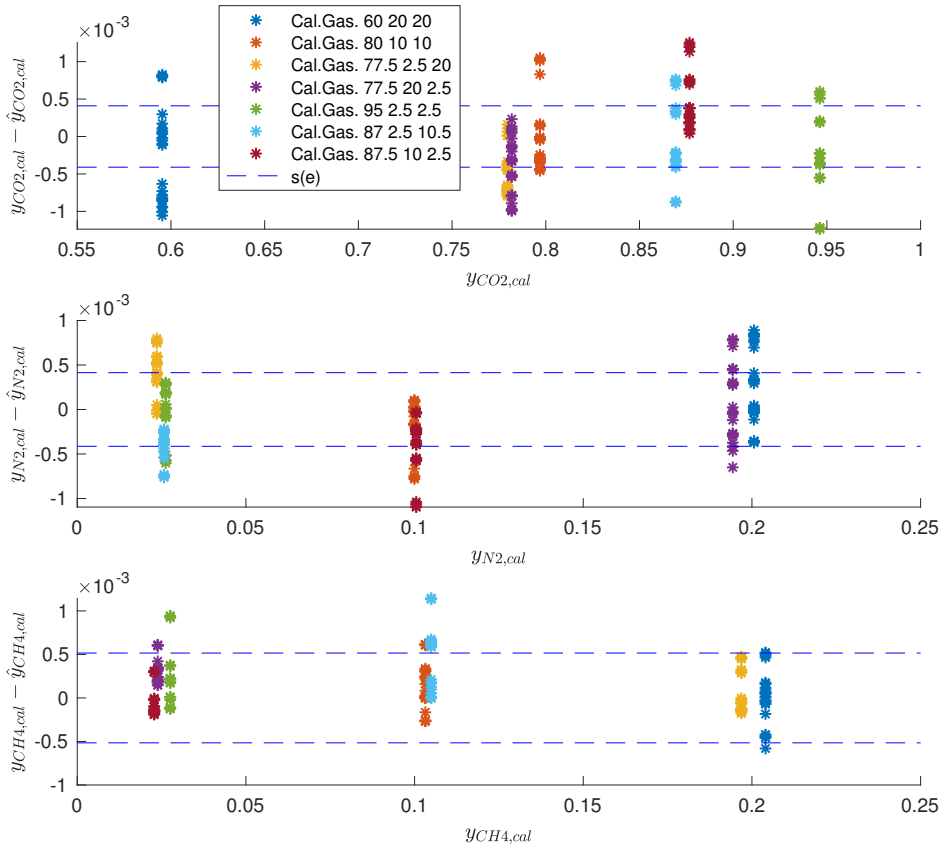

Figure 4.8: Residuals between fitted composition calibration function for the vapor sampler and the gravimetrically determined composition of the 7 calibration gases plotted versus mole fraction of CO_2 (top), N_2 (middle) and CH_4 (bottom).

4.2 Uncertainty Analysis in Measurements

4.2.1 Temperature

As given in equation 4.8, the temperature in the cell was taken to be the arithmetic mean of the measured temperature in the top and bottom flange of the cell. The measurement of one VLE point consisted of several, usually 6, sampling repetitions. The temperature at each repetition, $\bar{T}$, was taken to be the average of the temperature the 2 minutes before the sample was taken. The standard deviation in each of the resistance ratios during the two minutes was in the range $5 \cdot 10^{-7}$-$5 \cdot 10^{-6}$. This corresponds to a standard deviation of 0.1 mK to 1.3 mK. Since the arithmetic mean of the two sensors was taken as the cell temperature, a paired approach was first used to find the standard deviation of the estimated final temperature, $\bar{T}_f$:

$$s^2(\bar{T}_f, paired) = \sum_{i=1}^{n} (\bar{T}_i - \bar{T}_f)^2 \tag{4.25}$$

$\bar{T}_f$ is the average temperature of all sample repetitions at that VLE point, n is the number of samples taken at that VLE point and $\bar{T}_i$ is the average temperature of T04 and T05 in repetition i, $\bar{T}_i = (\overline{T04}_i + \overline{T05}_i)/2$. Notice that $\overline{T04}_i$ and $\overline{T05}_i$ is the average of the recorded temperature during the two minutes before sample i was taken. For the alternating sampling scheme (see section 3.2.4 for procedure), the final temperature $\bar{T}_f$ was taken to be the average of all sample repetition temperatures at both the liquid and vapor sampler. For the sequential scheme, the final temperature for the bubble points was taken to be the average of all sample repetitions at the liquid sampler and the final temperature for the dew points was taken to be the average of all sample repetitions at the vapor sampler. Using the paired approach resulted in standard deviations in the range of 0.008 to 1.5 mK. Next, an unpaired approach was used to estimate the standard deviation of the average temperature between the two temperature sensors:

$$s^2(\bar{T}_f, unpaired) = (\overline{T04} - \bar{T}_f)^2 + (\overline{T05} - \bar{T}_f)^2 \tag{4.26}$$

with

$$\overline{T04} = \frac{\sum_{i=1}^{n} T04_i}{n} \tag{4.27}$$

$$\overline{T05} = \frac{\sum_{i=1}^{n} T05_i}{n} \tag{4.28}$$

Using the unpaired approach the standard deviation was in the range of 2.6 mK to 14 mK, significantly larger than for the paired approach. The reason for this was a deviation between T04 and T05 of around 10-20 mK in the measurements. This reflects the non-uniformity of the temperature in the fluid bath and the cell, due to a temperature gradient from the outer walls of the fluid bath to the center, representing the heat loss to the environments. The non-uniformity was therefore taken as the dominating source of uncertainty and the standard uncertainty estimated as the unpaired standard deviation of the average between T04 and T05, $u(\bar{T}_f) \approx s^2(\bar{T}_f, unpaired)$.

4.2.2 Pressure

A thorough uncertainty analysis of pressure had previously been performed during the study of the binary system CO_2-N_2. Details of this analysis can be found in appendix A.1 in Westman *et*

al. (2016) [5]. The significant aspects are included in the following analysis.

The cell pressure, p, was taken to be the sum of the absolute pressure, differential pressure and the hydrostatic pressure (see below for further explanation). The hydrostatic and differential pressure were very small compared to the absolute pressure. However, their impact was often of the same magnitude as the uncertainty in pressure and therefore had to be included to achieve the most accurate pressure estimate possible. Since the absolute, differential and hydro-static pressure could not be assumed to be independent, the combined uncertainty in one pressure measurement,$u_c(p)$, was estimated as stated in equation 4.29.

$$u_c(p) = |u(p_i)| + |u(p_{diff})| + |u(p_{hs})| \tag{4.29}$$

Absolute Pressure Sensor

The precision of the absolute pressure sensors (Keller model PAA-33X) was stated by the producer to be 0.01% of the full scale, which was 10, 30, 100 and 200 bars for P01, P02, P03 and P04 respectively. Hence, the uncertainty in the absolute pressure reading,$u(p_i)$, was set to 1e-4, 3e-4, 1e-3 and 2e-3 MPa respectively. As described in section 4.1.2, the pressure sensors were calibrated using a dead weight to relate the sensor reading to a reference pressure. Figure 4.1 shows the residuals as a function of sensor pressure for the four pressure sensors. The residuals for pressure sensor PT01, PT02 and PT03 were all below the stated precision, except for two of the calibration measurements at PT03 which were slightly above 1e-3 and one of the calibration measurements at PT02 which was approximately 4e-04. Based on the calibration measurements for PT01, PT02, PT03 the standard uncertainty in the absolute pressure sensors, $u(p_i)$, was therefore set to the sensor precision. For PT04, the calibration measurements above 16 MPa deviated significantly from the linear trend. This was due to a leakage in the pressure circuit for pressure higher than 16 MPa during the pressure calibration measurements. The calibration measurements for PT04 should therefore be redone. However, PT04 was not used in this measurement campaign and thus the PT04 calibration did not affect the results.

Differential Pressure Sensor

Several sources of uncertainty for the differential pressure sensor were identified in Westman *et al.* (2016) [5], but it was concluded that the uncertainty due to the AD converter, $u(p_{diff,AD})$ = 240 Pa, was the dominating source if the differential pressure was kept close to zero. Since the differential pressure was kept below 1e-03 MPa during the VLE measurements, the uncertainty in differential pressure was taken to be $u(p_{diff})$ = $u(p_{diff,vib})$ = 240 Pa.

Hydrostatic Pressure Estimation

A sketch of the cell is shown in Figure 4.9, taken from Westman *et al.* (2016) with permission from Sintef. It illustrates the height, h_{vap}, between the liquid interface and the differential pressure sensor, p_{11}. This fluid column contributes to a small increase in pressure at the liquid interface as compared to the location and height of the differential pressure sensor. Assuming a

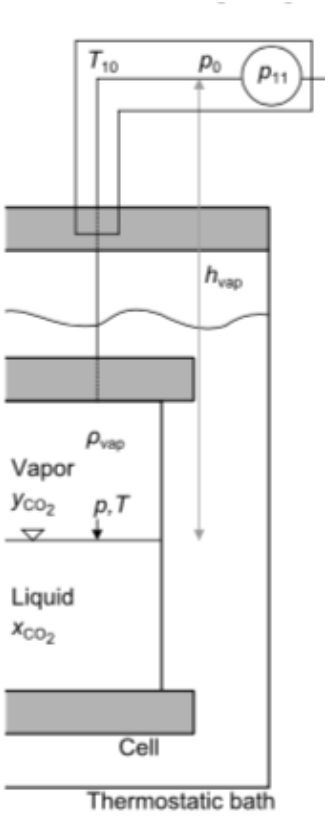

Figure 4.9: Sketch of height difference between cell and differential pressure sensor taken from Westman *et al.* (2016) [5] with permission from Sintef.

constant density, the hydrostatic pressure is computed as:

$$p_{hs} = \rho G_L h \tag{4.30}$$

with G_L being the locally measured gravity constant (9.82146m/s^2). Hence, the hydrostatic pressure contribution is proportional to the vapor density and was therefore highest at high pressures, at most 1.8e-3 MPa. A very detailed analysis of the density estimation and uncertainty contribution was performed in Westman *et al.* (2016). However, since the contribution was at most slightly above the absolute pressure sensor uncertainty, a more coarse estimate was made for the liquid height, vapor density and the uncertainty in these quantities. For the 9 first VLE points (L1-L9 and V1-V9) a USB camera was used to visually inspect the liquid level in the cell, while the other measurements were done without a camera. For the 9 first VLE points the liquid height was therefore visually determined as a percentage of the total cell height (0.083 m) and the standard uncertainty set to 10% of the cell height. For the remaining measurements the liquid height was set to 50% of the cell height with a standard uncertainty of 40% of the cell height. Notice that the total vapor fluid column was 0.501 m high at maximum, when the

liquid level was at the bottom of the cell. Thus, the cell height contributed with at most 17% of the fluid column. As a coarse estimate, the vapor phase density was calculated at the cell temperature, pressure, and vapor phase composition using the EOS-CG 2019 model. The standard uncertainty in vapor density, $u(\rho, vap)$, was set to 10% of the vapor density. The combined uncertainty in hydrostatic pressure was computed using equation 4.31 by assuming uncertainty in density and liquid height to be independent:

$$u(p_{hs}) = \sqrt{\left(\frac{\partial p_{hs}}{\partial \rho_{vap}} u(\rho_{vap})\right)^2 + \left(\frac{\partial p_{hs}}{\partial h} u(h)\right)^2} \tag{4.31}$$

with the partial derivatives equal to $g_L h$ and $g_L \rho_{vap}$ for density and height respectively. $u(p_{hs})$ was at most 1.9e-4 MPa and the impact on the combined uncertainty was therefore small but not negligible. The pressure at each sample repetition, $\bar{p}$, was taken to be the average of the measured pressure two minutes before the sample was taken. The uncertainty of this averaged pressure is stated in equation 4.32 with $s(\bar{p})$ being the standard deviation of the repetitions during the two minutes. As will be described further in section 4.2.4, the average pressure of the first sample repetition was taken as the final pressure, $\bar{p}_f$ for the VLE point reported.

$$u(\bar{p}) = \sqrt{u_c(p)^2 + s(\bar{p})^2} \tag{4.32}$$

4.2.3 Verification of Temperature and Pressure Uncertainty Analysis

The saturation pressure of pure CO_2 was measured at each isotherm to verify the accuracy of the pressure and temperature sensors. A summary of the saturation pressure measurements is given below in Table 4.4. To assess the total uncertainty in pressure including the effect of the uncertainty in temperature, equation 4.33 was used. p_{calc} is the computed saturation pressure using EOS-CG 2019. All the saturation pressure measurements are within 1.5 standard uncertainties of the values, and two of the measurement are within 1 standard uncertainty. It was therefore concluded that the uncertainty analysis of pressure and temperature presented in this chapter gave a realistic picture of the measurement uncertainty in temperature and pressure.

$$u_{tot}(\bar{p}) = \sqrt{u(\bar{p})^2 + \left(\frac{\partial \bar{p}}{\partial \bar{T}} u(\bar{T})\right)^2} \tag{4.33}$$

Table 4.4: Saturation pressure measurements of CO_2 including uncertainties and deviations.

ID	T [K]	p [Mpa]	p_{calc} [MPa]	$u(\bar{T})$ [K]	$u(\bar{p})$ [MPa]	$u_{tot}(p)$ [MPa]	$p - p_{calc}$ [MPa]
P1	223.150	0.6824	0.6823	6.0E-03	3.5E-04	3.8E-04	-8.81E-05
P2	253.160	1.9695	1.9703	2.7E-03	5.7E-04	5.8E-04	8.34E-04
P3	273.168	3.4900	3.4868	1.2E-02	1.3E-03	2.1E-03	-3.24E-03
P4	283.194	4.5083	4.5071	1.0E-03	1.3E-03	1.4E-03	-1.22E-03
P5	298.148	6.4376	6.4339	3.1E-03	1.4E-03	2.5E-03	-3.64E-03

4.2.4 Composition

For binary mixtures, an uncertainty stated in the mole fraction of CO_2 will implicitly also specify the uncertainty of the other component. However, for a ternary mixture this will not be

the case. Therefore, the combined uncertainty of each component (CO_2, N_2 and CH_4) was assessed. In section 4.1.3 the procedure of fitting a calibration function to all the calibration measurements was described. Figure 4.7 and 4.8 show the residuals between gravimetrically determined mole fraction and the predicted mole fraction of the calibration function for all three component together with the standard deviation of the residuals. In previous studies on binary CO_2-rich mixtures, the standard deviations of the residuals in mole fraction of CO_2 were used as the best estimate of the combined uncertainty in composition. For the ternary mixture being used in this work, the combined uncertainty in each component, $u_c(x_i)$ and $u_c(y_i)$, was set to the standard deviation of the residuals in the respective component. The combined standard uncertainty was specified separately for the liquid and vapor sampler calibration function. All these standard uncertainties were less than $5 \cdot 10^{-4}$ mole fraction, and can be found in table A.1 and A.2 in appendix A.2. The reason for choosing the standard deviation of the residuals in the calibration function as the best estimate of the combined uncertainty in composition, was that the calibration function was considered to be the dominating source of uncertainty. The uncertainty of the gravimetrically prepared calibration gases was of magnitude 10^{-6}, and was therefore negligible compared to the standard deviation of the calibration function residuals. Details on the uncertainty analysis of the gravimetrically prepared calibration gases can be found in the report from the summer job in Sintef during the summer of 2018 [40]. It makes sense that the residuals of the calibration function are the dominating source of uncertainty, since the function relates the area output of the GC to the composition based on a non-linear function fitted to a limited amount of calibration measurements.

During this measurement campaign, the bellows in the cell were not working. Hence, it was not possible to compensate the pressure after a sample was taken. When taking a sample, a small amount of mass was extracted from the cell through the capillary and sent to the GC for analysis. This changed both the cell pressure and composition of the phase being sampled slightly. Therefore, the next sample taken would be at a different pressure and composition. In section 3.2.4 two different sampling schemes were described. When using the alternating sampling scheme (sampling alternately with liquid and vapor sampler) the pressure measured before the first sample taken was used as the VLE point pressure, $\bar{p}_f$. Thus, the pressure of the points measured with the alternating sampling scheme are equal for bubble and dew points. Notice that this pressure was the average of the pressure during the two minutes before the sample was taken. For the sequential sampling scheme (first sampling 6 liquid samples then 6 vapor samples), bubble point and dew point pressure was taken to be the average pressure before the first liquid and vapor samples, respectively. Since the first sample taken was a flushing sample to flush the capillaries, it could not be used to estimate the VLE composition. Therefore, a linear regression was performed between composition and pressure to estimate the composition at the equilibrium pressure (before the first sample). This was done for all the components. Figure 4.10 shows an example, with the light green point being the estimated composition in equilibrium,$z_{f,i}$, at the equilibrium pressure $\bar{p}_f$. The stapled red lines shows a 67% prediction interval of the linear regression. In the example (Figure 4.10) the prediction interval for the CO_2 composition is very slim due to the clear linear trend among the sample repetitions. All the sample series did not have such a clear linear trend. For example, the linear regression of the liquid methane concentration (bottom plot Figure 4.10) are not as accurate, which are reflected in a wider prediction interval. The width of the 67% prediction interval, $s(z_{f,i})$, was computed for all the samples and are stated in tables A.1 and A.2 in appendix A.2. The uncertainty of the final equilibrium composition was estimated as stated in equation 4.34, with $u_c(z_i)$ being the

standard combined uncertainty of the component i. For most of the measurements $s(z_{f,i})$ was less than 1e-04 mole fraction and had very little impact. This illustrates that the repeatably of the GC was higher than the precision of the calibration function. Notice that both the pressure and the mole fraction in the linear regression are standardized around the mean of the repetition pressures and mole fractions in figure 4.10. A summary of $u(z_{f,i})$ for all measurements and components can be found in tables 5.1 and 5.2 in section 5.1.1.

$$u(z_{f,i}) = \sqrt{u_c(z_i)^2 + s(z_{f,i})^2} \tag{4.34}$$

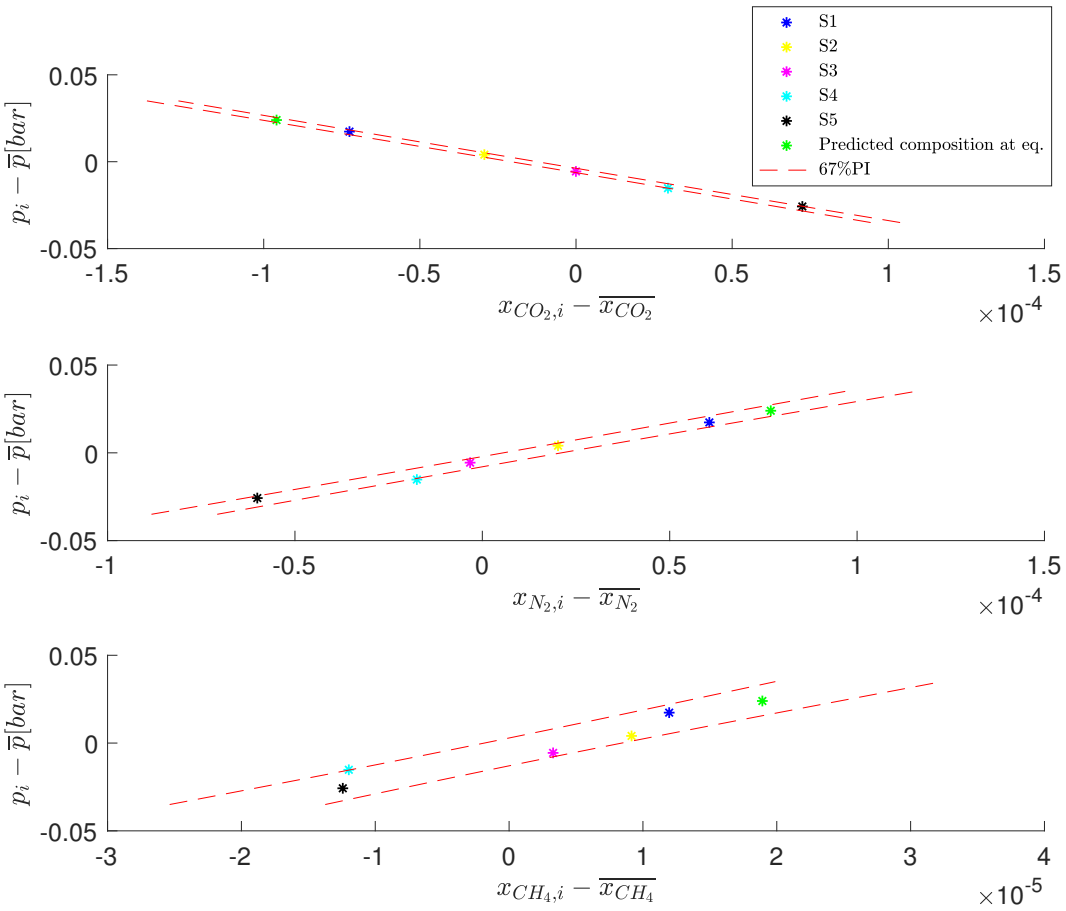

Figure 4.10: Example of a linear extrapolation to determine the equilibrium mole fraction of each component.

4.2.5 Verification of Calibration Function

During the previous measurement campaigns on binary systems by Sintef [5], [17], [18], [6], [19], it was assumed that the calibration function for the GC was valid through the entire campaign. Usually, all the calibration measurements were performed before the VLE measurements. However, it was never verified that the GC output was consistent over time by taking verification samples of the calibration gases subsequent to the measurement campaign. In this

work, verification samples were taken of the 77.5-2.5-20 and 87.5-10-2.5 CO_2-N_2-CH_4 calibration gases at two different area responses for both the liquid and vapor sampler at the end of the measurement campaign. It was chosen to only check two of the calibration gases due to limited amount of time available after the VLE measurements had been completed. The 77.5-2.5-20 and 87.5-10.0-2.5 CO_2-N_2-CH_4 calibration gases were chosen because the mole fraction of each component was different in these gases. They were also among the first gases that were made, and therefore represented the largest risk of potential drifting in the GC. For all the verification samples taken with the vapor sampler, the residual between gravimetrically determined composition (see table 4.2 for accurate compositions) and the predicted composition by the calibration function was within the standard combined uncertainty for all the components. See table A.1 and A.2 in appendix A.2 for $u_c(y_i)$ and $u_c(x_i)$ for all components. For the liquid sampler, about 70% of the samples were within the standard combined uncertainty and 30% slightly above the standard combined uncertainty, well below two times the standard combined uncertainty. All the residuals are presented in Figures A.3 to A.6 in appendix A.3. Based on the size of the residuals, it was concluded that the composition calibration function as a function of the GC area output did not significantly drift during the measurement campaign, a period of approximately 10 months.

4.2.6 Total Uncertainty

In the preceding paragraphs, uncertainty estimates of temperature, pressure and composition of the VLE points have been presented. However, a total uncertainty in one of the quantities was desired because all the variables depend on each other. Composition was chosen as the quantity for the total uncertainty. Equation 4.35 was used to estimate the total uncertainty in component i. The partial derivatives with respect to temperature and pressure were computed numerically using the EOS-CG 2019 model. For all the measurements, the total uncertainty of CO_2 was higher than the total uncertainty of methane and nitrogen. This was mainly due to higher combined uncertainty in the composition of CO_2,$u(z_{f,\mathrm{CO}_2})$, and higher partial derivatives with respect to pressure, $\frac{\partial z_{f,\mathrm{CO}_2}}{\partial p}$. As a conservative estimate, the total standard uncertainty of the composition was therefore set to the total standard uncertainty in CO_2 composition, $u_{tot}(z_f) = u_{tot}(z_{f,i})$. The total uncertainties in each component can be found in tables A.1 and A.2 in appendix A.2.

$$u_{tot}(z_{f,i}) = \sqrt{(u(z_{f,i}))^2 + \left(u(\bar{T}_f)\frac{\partial z_{f,i}}{\partial T}\right)^2 + \left(u(\bar{p}_f)\frac{\partial z_{f,i}}{\partial p}\right)^2} \tag{4.35}$$

4.3 A Tool for Visualizing the Helmholtz Model

In the master thesis by Neumann (2017) [20], a new tool to visualize the Helmholtz energy model was developed in Matlab. The tool was able to generate 3D diagrams of the residual Helmholtz energy, its derivatives (α_τ, α_δ, $\alpha_{\tau\tau}$, $\alpha_{\delta\delta}$, and $\alpha_{\tau\delta}$), the various terms (polynomial, exponential, GBS, and special exponential, see equation 2.8 to 2.11 and equation 2.16) and sums of terms and term types. The subscript in the derivatives refer to which variable (reduced temperature, τ, or reduced density δ) the residual Helmholtz energy is differentiated with respect to. The x- and y-axis was set to a desired combination of temperature, density and composition, either in reduced or absolute form.

However, the tool was only capable of handling pure fluids or binary mixtures. The Helmholtz energy computations were implemented specifically for pure fluids or binary mixtures such that simplifications could be made in the expressions of the equations of the residual Helmholtz energy and the reducing functions (equation 2.15, 2.17, and 2.18).

In this work, the tool has been extended to handle multi-component mixtures with any number of components. This required extensive modifications in the Matlab code, since all functions were made generic for n number of components. Thus, equations 2.16, 2.17, and 2.18 were now implemented in their original form. The structure of the variables were also changed to handle n number of components. Since a mixture with n number of components will have $\binom{n}{2}$ (the binomial coefficient) binary contributions, the number of α_{ij}^r, and number of terms and sum of terms quickly grow as the number of components increase. Therefore, the storage and plotting of the terms were restructured to be more generic for multi-component mixtures. As an example, a plot of the residual Helmholtz energy of the quaternary mixture CO_2-N_2-CH_4-O_2 together with the residual pure component contribution of CO_2 is presented in Figure 4.11. To

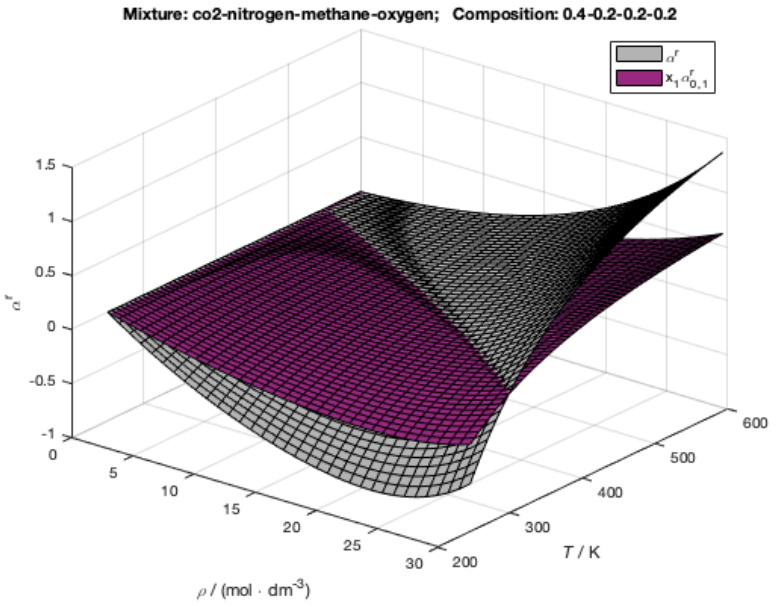

Figure 4.11: Residual Helmholtz energy of the quaternary mixture CO_2-N_2-CH_4-O_2 together with the residual pure component contribution of CO_2 calculated with EOS-CG 2019 on a temperature-density grid. The composition is set to 40 mole% CO_2, 20 mole% N_2, 20 mole%CH_4, and 20 mole% O_2.

be able to plot the Helmholtz energy on a temperature-density grid, the composition needs to be fixed. However, it is often desired to see how the Helmholtz energy, its derivatives, or some of the additive terms change as the composition varies. For binary mixtures, it is easy to visualize this in a 3D-plot as the composition, x_i, of one component can be varied and the other be implicit. An example of such a plot is shown in Figure 4.12. For mixtures with more than two components it is more challenging to visualize the composition variation in three dimensions, because the degrees of freedom increases. The focus of this work is the ternary mixture CO_2-N_2-CH_4. Therefore, the implemented ways of visualizing a varying composition has been focused on ternary mixtures. Two options have been implemented. The first option keeps one

of the three components fixed and varies the two remaining components in the same way as for a binary mixture, see Figure 4.13. The second option is specifying a ratio between two of the components and then vary the last component, see Figure 4.14.

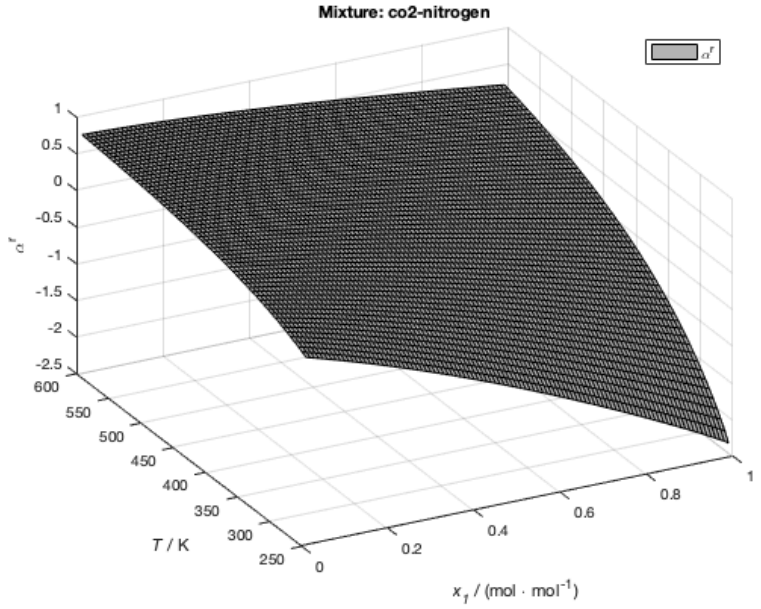

Figure 4.12: Residual Helmholtz energy of the binary mixture CO_2-N_2 calculated with EOS-CG 2019 plotted on a temperature-composition grid with a constant density of 20 mol/L.

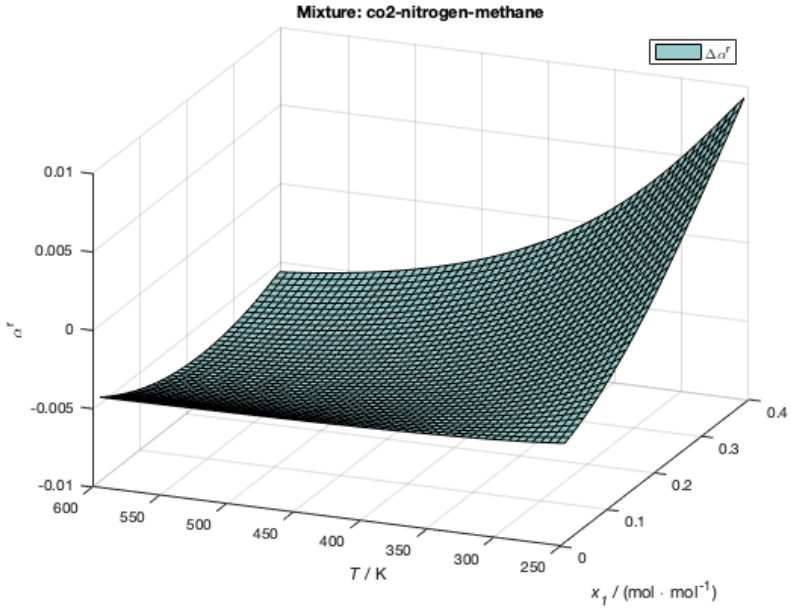

Figure 4.13: The departure function of the ternary mixture CO_2-N_2-CH_4 plotted on a temperature-composition grid with a constant constant density of 20 mol/L. The composition of N_2 is kept constant at 60 mole%.

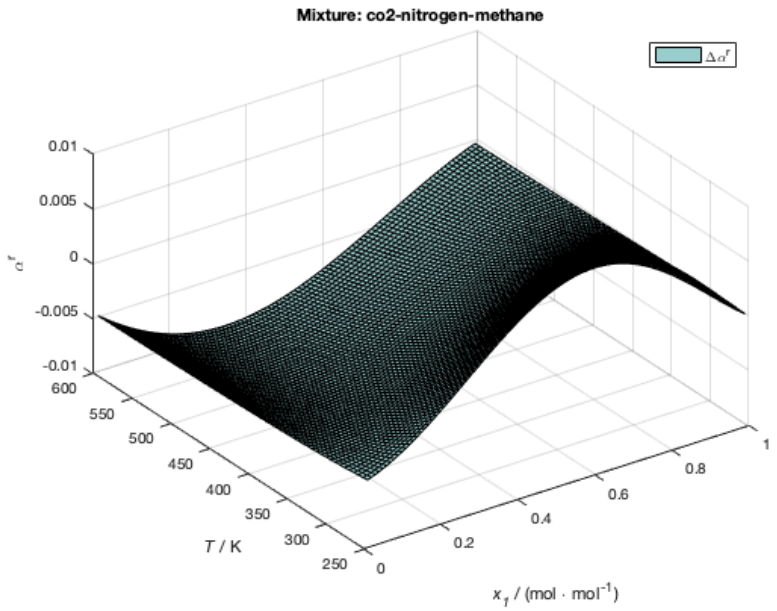

Figure 4.14: The departure function of the ternary mixture CO_2-N_2-CH_4 calculated with EOS-CG 2019 plotted with temperature on the x-axis and mole fraction of CO_2 on the y-axis. The density is constant and equal to 20 mol/L. The ratio between the composition of N_2 and CH_4 is kept constant at 1:1.

Chapter 5

Results and Discussion

This chapter includes all the VLE measurement results (section 5.1.1), a comparison of the measurements to the state-of-the art Helmholtz energy based EOS, EOS-CG 2019, (section 5.1.2), comparison to literature data (section 5.1.3), and a discussion and visualization of the various terms of the EOS-CG 2019 model (section 5.2).

5.1 Measurement Results and Discussion

5.1.1 Measurement Results

The measurement results are summarized in table 5.1 and table 5.2 for bubble points and dew points respectively. The uncertainty in the saturation temperature, $u(\bar{T}_f)$, and pressure, $u(\bar{p}_f)$, the uncertainty in composition of each component, $u(x_{f,i})$ and $u(y_{f,i})$, and the total uncertainty of the composition, $u_{tot}(x_f)$ and $u_{tot}(y_f)$, are stated along with the temperature, pressure and composition of each VLE point. A more complete overview of the uncertainties described in section 4.2 can be found in appendix A.2. A total of 31 bubble and 31 dew points are reported at the temperatures 223 K, 253 K, 273 K, 283 K and 298 K. The measurements at 298 K were performed during the specialization project in fall 2018, but has been re-analyzed and discussed together with the measurements at the other isotherms. The experimental points L1-L5, L10-L31, V1-V5 and V10-V31 were measured with approximately equal amounts of nitrogen and methane in the total composition of the cell. The experimental points L6-L9 and V6-V9 were measured with a ratio between total composition of nitrogen and methane of approximately $z_{\mathrm{N}_2} : z_{\mathrm{CH}_4}$ = 4.4:1.

Table 5.1: The final temperature, pressure and composition of the 31 measured bubble points are shown in column two to six. The most important uncertainty terms are shown in column seven to twelve.

ID	T [K]	p [MPa]	$x_{\mathrm{N_2}}$ [-]	$x_{\mathrm{CH_4}}$ [-]	$x_{\mathrm{CO_2}}$ [-]	$u(\bar{T}_f)$ [K]	$u(\bar{p}_f)$ [MPa]	$u(x_{f,\mathrm{N_2}})$ [-]	$u(x_{f,\mathrm{CH_4}})$ [-]	$u(x_{f,\mathrm{CO_2}})$ [-]	$u_{tot}(x_f)$ [-]
L1	298.138	7.085	0.0089	0.0104	0.9807	8.5E-03	1.5E-03	3.4E-04	2.7E-04	4.2E-04	4.2E-04
L2	298.133	7.524	0.0163	0.0186	0.9651	5.1E-03	1.4E-03	3.4E-04	2.7E-04	4.2E-04	4.2E-04
L3	298.131	7.789	0.0220	0.0244	0.9535	5.5E-03	1.4E-03	3.4E-04	2.7E-04	4.2E-04	4.2E-04
L4	298.131	7.928	0.0266	0.0294	0.9440	5.8E-03	1.4E-03	3.5E-04	2.8E-04	4.6E-04	4.7E-04
L5	298.130	7.877	0.0246	0.0267	0.9487	5.4E-03	1.4E-03	3.5E-04	2.8E-04	4.5E-04	4.6E-04
L6	298.129	6.897	0.0090	0.0024	0.9885	4.6E-03	1.4E-03	3.4E-04	2.7E-04	4.2E-04	4.2E-04
L7	298.129	7.304	0.0183	0.0048	0.9769	4.8E-03	1.4E-03	3.5E-04	2.7E-04	4.3E-04	4.3E-04
L8	298.129	7.669	0.0278	0.0071	0.9651	5.8E-03	1.4E-03	3.4E-04	2.7E-04	4.2E-04	4.2E-04
L9	298.129	7.927	0.0362	0.0088	0.9551	5.5E-03	1.4E-03	3.4E-04	2.7E-04	4.2E-04	4.3E-04
L10	283.154	5.254	0.0083	0.0115	0.9803	1.3E-02	1.3E-03	3.4E-04	2.7E-04	4.2E-04	4.2E-04
L11	283.154	6.146	0.0201	0.0249	0.9550	1.3E-02	1.3E-03	3.4E-04	2.7E-04	4.2E-04	4.2E-04
L12	283.154	7.089	0.0350	0.0388	0.9262	1.3E-02	1.4E-03	3.4E-04	2.7E-04	4.2E-04	4.2E-04
L13	283.155	7.680	0.0449	0.0496	0.9055	1.4E-02	1.4E-03	3.4E-04	2.7E-04	4.2E-04	4.2E-04
L14	283.156	8.259	0.0567	0.0602	0.8831	1.3E-02	1.4E-03	3.4E-04	2.7E-04	4.2E-04	4.2E-04
L15	283.156	8.848	0.0709	0.0766	0.8526	1.4E-02	1.4E-03	3.4E-04	2.7E-04	4.2E-04	4.3E-04
L16	273.168	3.990	0.0050	0.0076	0.9874	1.0E-02	1.3E-03	3.4E-04	2.7E-04	4.2E-04	4.2E-04
L17	273.166	5.252	0.0195	0.0277	0.9527	1.1E-02	1.3E-03	3.4E-04	2.7E-04	4.2E-04	4.2E-04
L18	273.167	6.261	0.0330	0.0444	0.9226	9.9E-03	1.3E-03	3.4E-04	2.7E-04	4.2E-04	4.2E-04
L19	273.167	7.220	0.0478	0.0609	0.8913	1.0E-02	1.4E-03	3.4E-04	2.7E-04	4.2E-04	4.2E-04
L20	273.167	8.166	0.0652	0.0783	0.8565	9.6E-03	1.4E-03	3.4E-04	2.7E-04	4.2E-04	4.2E-04
L21	273.169	8.802	0.0794	0.0912	0.8294	1.0E-02	1.4E-03	3.4E-04	2.7E-04	4.2E-04	4.2E-04
L22	273.170	9.324	0.0939	0.1030	0.8031	1.0E-02	1.4E-03	3.4E-04	2.7E-04	4.2E-04	4.2E-04
L23	253.162	2.337	0.0033	0.0057	0.9910	3.3E-03	5.7E-04	3.4E-04	2.7E-04	4.2E-04	4.2E-04
L24	253.162	2.686	0.0066	0.0113	0.9821	3.5E-03	5.8E-04	3.4E-04	2.7E-04	4.2E-04	4.2E-04
L25	253.163	3.042	0.0102	0.0171	0.9727	3.2E-03	1.3E-03	3.4E-04	2.7E-04	4.2E-04	4.2E-04
L26	253.162	3.411	0.0141	0.0231	0.9629	3.2E-03	1.3E-03	3.4E-04	2.7E-04	4.2E-04	4.2E-04
L27	253.163	3.799	0.0183	0.0294	0.9523	3.0E-03	1.3E-03	3.4E-04	2.7E-04	4.2E-04	4.2E-04
L28	223.151	0.796	0.0009	0.0018	0.9972	6.7E-03	3.5E-04	3.4E-04	2.7E-04	4.2E-04	4.2E-04
L29	223.151	0.996	0.0024	0.0051	0.9925	6.7E-03	3.5E-04	3.4E-04	2.7E-04	4.2E-04	4.2E-04
L30	223.151	1.098	0.0033	0.0068	0.9899	6.5E-03	5.5E-04	3.4E-04	2.7E-04	4.2E-04	4.2E-04
L31	223.150	1.225	0.0044	0.0089	0.9867	5.9E-03	5.5E-04	3.4E-04	2.7E-04	4.2E-04	4.2E-04

Table 5.2: The final temperature, pressure and composition of the 31 measured dew points are shown in column two to six. The most important uncertainty terms are shown in column seven to twelve.

ID	T [K]	p [MPa]	$x_{\mathrm{N_2}}$ [-]	$x_{\mathrm{CH_4}}$ [-]	$x_{\mathrm{CO_2}}$ [-]	$u(\bar{T}_f)$ [K]	$u(\bar{p}_f)$ [MPa]	$u(y_{f,\mathrm{N_2}})$ [-]	$u(y_{f,\mathrm{CH_4}})$ [-]	$u(y_{f,\mathrm{CO_2}})$ [-]	$u_{tot}(y_f)$ [-]
V1	298.138	7.085	0.0215	0.0198	0.9587	8.5E-03	1.5E-03	4.4E-04	3.3E-04	5.7E-04	5.8E-04
V2	298.133	7.524	0.0319	0.0307	0.9373	5.1E-03	1.4E-03	4.4E-04	3.3E-04	5.7E-04	5.7E-04
V3	298.131	7.789	0.0356	0.0350	0.9295	5.5E-03	1.4E-03	4.4E-04	3.3E-04	5.7E-04	5.7E-04
V4	298.131	7.929	0.0350	0.0353	0.9296	5.8E-03	1.4E-03	4.4E-04	3.3E-04	5.7E-04	5.7E-04
V5	298.130	7.877	0.0359	0.0356	0.9285	5.4E-03	1.4E-03	4.4E-04	3.3E-04	5.7E-04	5.7E-04
V6	298.129	6.898	0.0240	0.0050	0.9710	4.6E-03	1.4E-03	4.4E-04	3.3E-04	5.7E-04	5.7E-04
V7	298.129	7.305	0.0419	0.0088	0.9493	4.8E-03	1.4E-03	4.4E-04	3.3E-04	5.7E-04	5.7E-04
V8	298.129	7.670	0.0539	0.0112	0.9348	5.8E-03	1.4E-03	4.4E-04	3.3E-04	5.7E-04	5.7E-04
V9	298.129	7.928	0.0593	0.0122	0.9285	5.5E-03	1.4E-03	4.4E-04	3.3E-04	5.7E-04	5.7E-04
V10	283.154	5.254	0.0476	0.0415	0.9110	1.3E-02	1.3E-03	4.4E-04	3.3E-04	5.7E-04	6.1E-04
V11	283.154	6.144	0.0905	0.0741	0.8354	1.3E-02	1.3E-03	4.4E-04	3.3E-04	5.7E-04	6.0E-04
V12	283.155	7.084	0.1229	0.0949	0.7822	1.3E-02	1.4E-03	4.4E-04	3.3E-04	5.7E-04	5.9E-04
V13	283.155	7.674	0.1334	0.1068	0.7597	6.8E-03	1.4E-03	4.4E-04	3.3E-04	5.7E-04	5.7E-04
V14	283.155	8.264	0.1359	0.1179	0.7463	1.4E-02	1.4E-03	4.4E-04	3.4E-04	5.8E-04	6.0E-04
V15	283.155	8.682	0.1360	0.1208	0.7432	1.4E-02	1.4E-03	4.4E-04	3.3E-04	5.7E-04	5.9E-04
V16	273.167	3.989	0.0465	0.0401	0.9134	1.0E-02	1.3E-03	4.4E-04	3.3E-04	5.8E-04	6.3E-04
V17	273.166	5.251	0.1263	0.1073	0.7663	1.0E-02	1.3E-03	4.4E-04	3.3E-04	5.7E-04	6.0E-04
V18	273.166	6.260	0.1645	0.1389	0.6967	1.0E-02	1.3E-03	4.4E-04	3.3E-04	5.7E-04	5.9E-04
V19	273.167	7.213	0.1875	0.1575	0.6549	9.7E-03	1.4E-03	4.4E-04	3.3E-04	5.7E-04	5.8E-04
V20	273.168	8.158	0.2001	0.1679	0.6319	9.6E-03	1.4E-03	4.4E-04	3.3E-04	5.7E-04	5.8E-04
V21	273.170	8.790	0.2021	0.1712	0.6267	1.0E-02	1.4E-03	4.4E-04	3.3E-04	5.7E-04	5.8E-04
V22	273.170	9.308	0.1995	0.1704	0.6301	1.0E-02	1.4E-03	4.4E-04	3.3E-04	5.7E-04	5.8E-04
V23	253.162	2.334	0.0668	0.0558	0.8774	3.2E-03	5.7E-04	4.5E-04	3.4E-04	6.0E-04	6.2E-04
V24	253.162	2.683	0.1184	0.0973	0.7843	3.2E-03	5.8E-04	4.4E-04	3.3E-04	5.7E-04	5.9E-04
V25	253.163	3.041	0.1575	0.1288	0.7136	3.2E-03	1.3E-03	4.7E-04	3.3E-04	6.0E-04	6.4E-04
V26	253.162	3.409	0.1893	0.1541	0.6566	3.2E-03	1.3E-03	4.4E-04	3.3E-04	5.7E-04	6.0E-04
V27	253.162	3.797	0.2153	0.1745	0.6102	3.4E-03	1.3E-03	4.4E-04	3.3E-04	5.7E-04	5.9E-04
V28	223.151	0.796	0.0708	0.0558	0.8734	6.7E-03	3.5E-04	4.5E-04	3.4E-04	5.9E-04	7.1E-04
V29	223.151	0.995	0.1606	0.1249	0.7145	6.5E-03	3.5E-04	4.5E-04	3.4E-04	5.8E-04	6.5E-04
V30	223.150	1.097	0.1950	0.1514	0.6537	6.4E-03	5.5E-04	4.5E-04	3.3E-04	5.8E-04	6.6E-04
V31	223.151	1.223	0.2289	0.1774	0.5937	6.1E-03	5.5E-04	4.4E-04	3.3E-04	5.7E-04	6.3E-04

5.1.2 Comparison of the Measurements to the Model

All the measurements were compared to the EOS-CG 2019 [4] model prediction. Several different options exist when comparing the experimental points to the model. One method would be the "method of shortest distance", finding the shortest distance between the experimental point and the multi-dimensional model surface (T,p,$x_{\mathrm{CO_2}}$, $z_{\mathrm{N_2}}$ and $z_{\mathrm{CH_4}}$ coordinates). However, using this method would require to non-dimensionalize the variables, and the residual would be relative to the absolute values measured. Therefore, a method conserving more of the physical meaning of the residual was used. The latter method is described in the following paragraph.

Temperature and pressure of the model prediction were fixed at the same temperature and pressure as the experimental point. Next, a tie line was drawn between the experimentally measured dew and bubble point (between L1 and V1, L2 and V2, etc.). The tie line thus represented a vector in the $x_{\mathrm{CO_2}}$-$z_{\mathrm{N_2}}$-$z_{\mathrm{CH_4}}$ space, and described all total compositions that would split in two phases with the measured bubble and dew point composition. The constant pressure and temperature plots presented in Figure 2.6 show examples of how these tie lines connect the bubble and dew point compositions. A small step along this tie line from the experimental point was then taken inwards in the two phase region, to make sure the total composition was in the two phase region. This was done for both the bubble and dew point. As mentioned in section 3.2.4 and 4.1.3, and as can be seen from the results tables 5.1 and 5.2, the pressure at the bubble and dew point was not necessarily the same. However, they were very close and it was verified that the tie line did not change significantly due to this small pressure discrepancy. The total composition found by taking a small step along the tie line from the experimental point was then flashed using EOS-CG 2019 at the experimental values for pressure and temperature. This was done separately for the bubble and dew points. In other words, the model prediction of the dew and bubble point compositions at that pressure, temperature and an estimated total composition was computed. If the total composition was still outside the two phase region, the step distance along the tie line was adjusted until the total composition was inside the two phase region. Notice again that the flash computation was performed at the temperature and pressure of bubble and dew points separately. Finally, the residual between the experimentally measured composition and the model prediction composition was computed for all points.

Figure 5.1 to 5.12 show plots of the 6 different series measured at the 5 temperatures 223 K, 253 K, 273 K, 283 K and 298 K. Notice that the saturation pressure measurements summarized in table 4.4 are included in the figures at the relevant isotherm. The pressures are plotted against the measured (crosses) and model predicted (circles) compositions. Separate figures are made for CO_2 mole fraction as well as N_2 and CH_4 mole fractions. Thus, Figure 5.1 to 5.12 represent pseudo-binary px-diagrams with the ratio between total composition of N_2 and CH_4, $z_{\mathrm{N_2}}$:$z_{\mathrm{CH_4}}$, kept approximately constant in each figure. Visualizing the measurements and the model predictions in this way gives useful information and illustrates important trends. Furthermore, the trends in these figures can be qualitatively compared to the binary px-diagrams of CO_2-N_2 and CO_2-CH_4 at the different temperatures. However, there are two important factors that should be taken into account when evaluating Figure 5.1 to 5.12. The first is that **the line between the model predicted points does not represent the model**, but is simply a straight line drawn between the points. The other is that the points in the $x_{\mathrm{CO_2}}$ or $y_{\mathrm{CO_2}}$-p diagrams are not fully determined, as they would be in a binary system. For the figures showing both the composition of N_2 and CH_4 the points are actually fully determined, since the composition of CO_2 in the liquid

phase can be computed as x_{CO_2}= 1-x_{N_2}-x_{CH_4} and equivalently using y for the vapor phase. The pseudo-binary figures along with residual plots are discussed after the figures are shown.

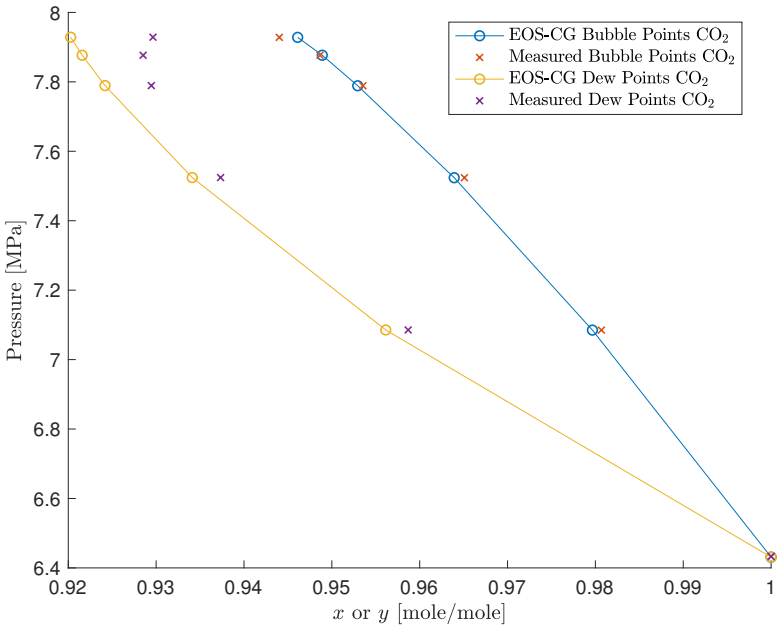

Figure 5.1: Series one of the 298 K isotherm (L1-L5 and V1-V5) with z_{N_2}:z_{CH_4}≈1:1, together with EOS-CG 2019 prediction. The pressure is plotted versus mole fraction of CO_2.

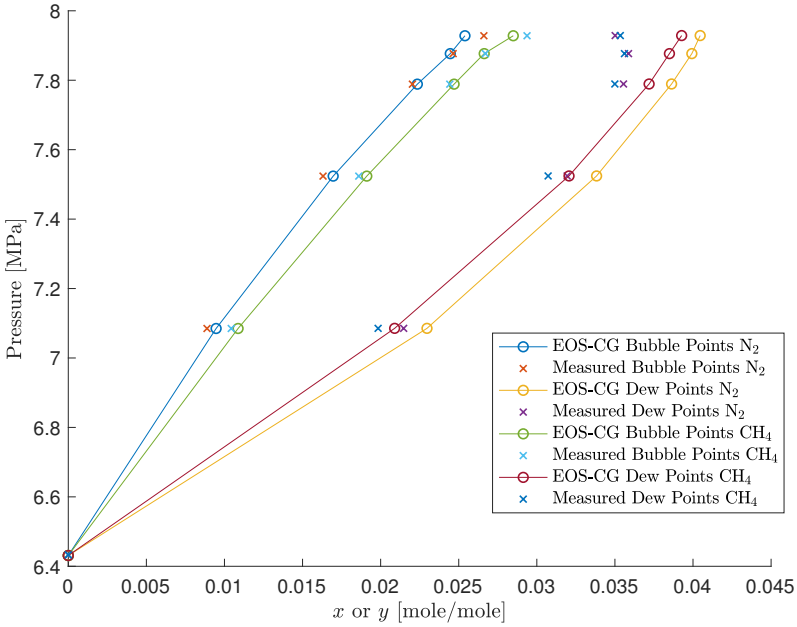

Figure 5.2: Series one of the 298 K isotherm (L1-L5 and V1-V5) with z_{N_2}:z_{CH_4}≈1:1, together with EOS-CG 2019 prediction. The pressure is plotted versus mole fraction of N_2 and CH_4.

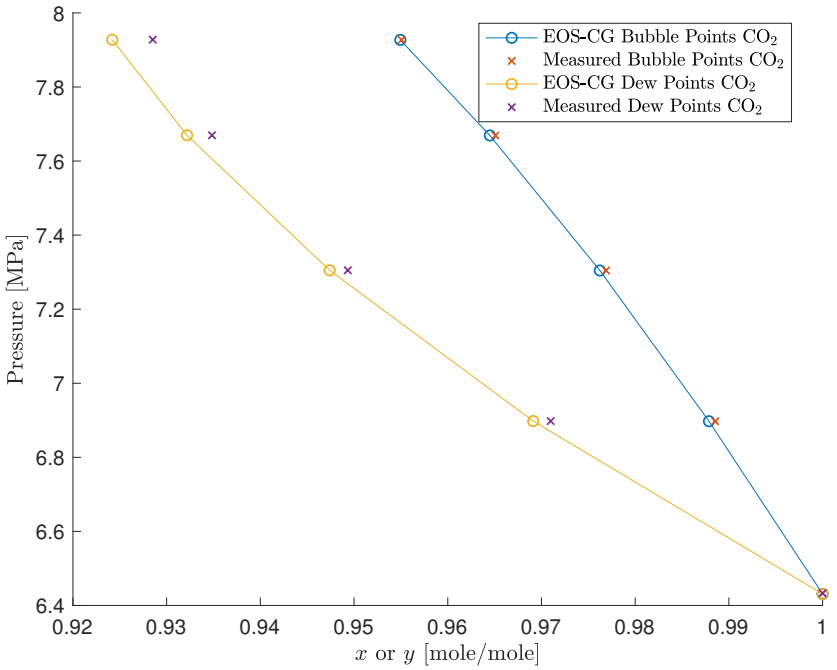

Figure 5.3: Series two of the 298 K isotherm (L6-L9 and V6-V9) with z_{N_2}:z_{CH_4}≈4.4:1, together with EOS-CG 2019 prediction. The pressure is plotted versus mole fraction of CO_2.

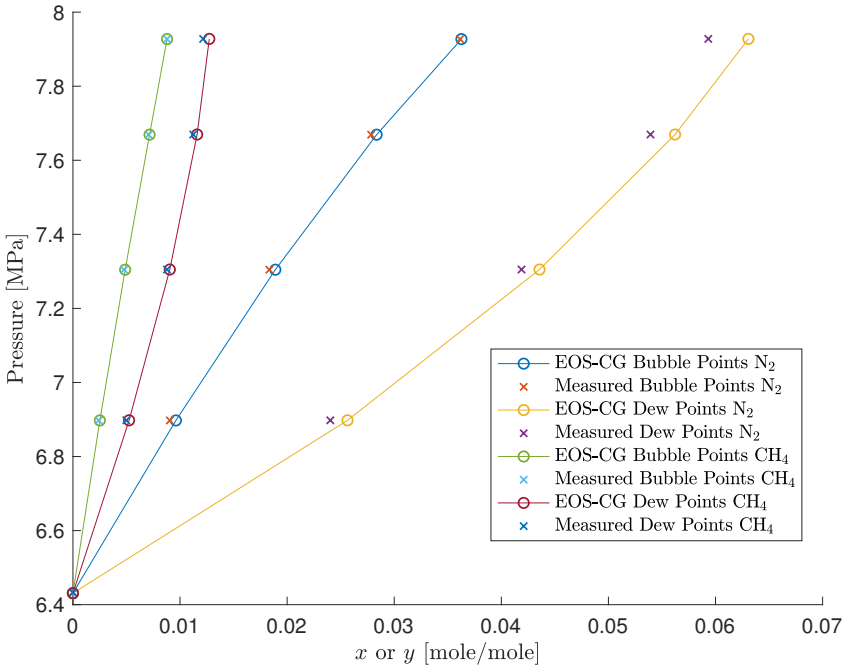

Figure 5.4: Series two of the 298 K isotherm (L6-L9 and V6-V9) with z_{N_2}:z_{CH_4}≈4.4:1, together with EOS-CG 2019 prediction. The pressure is plotted versus mole fraction of N_2 and CH_4.

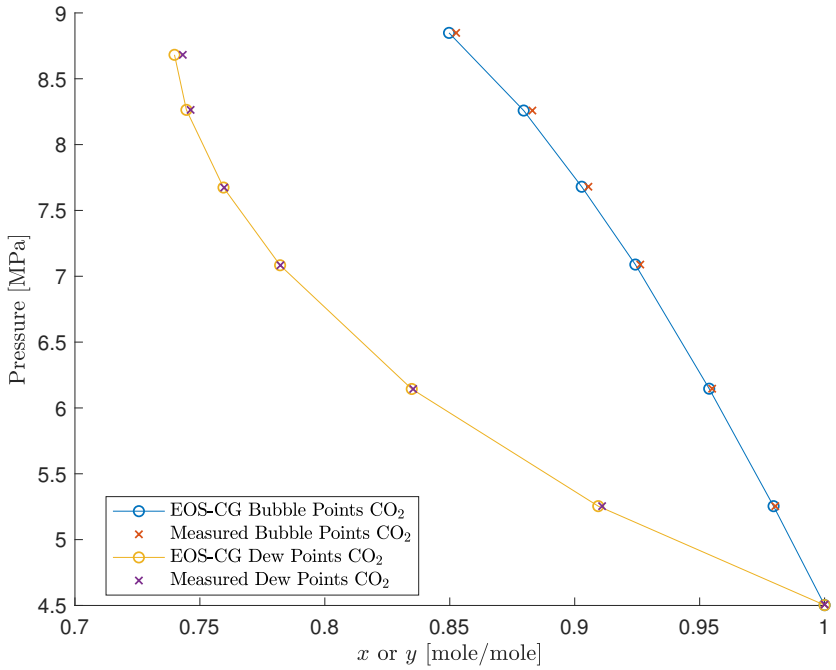

Figure 5.5: Measurements performed at 283 K (L10-L15 and V10-V15) with z_{N_2}:z_{CH_4}≈1:1, together with EOS-CG 2019 prediction. The pressure is plotted versus mole fraction of CO_2.

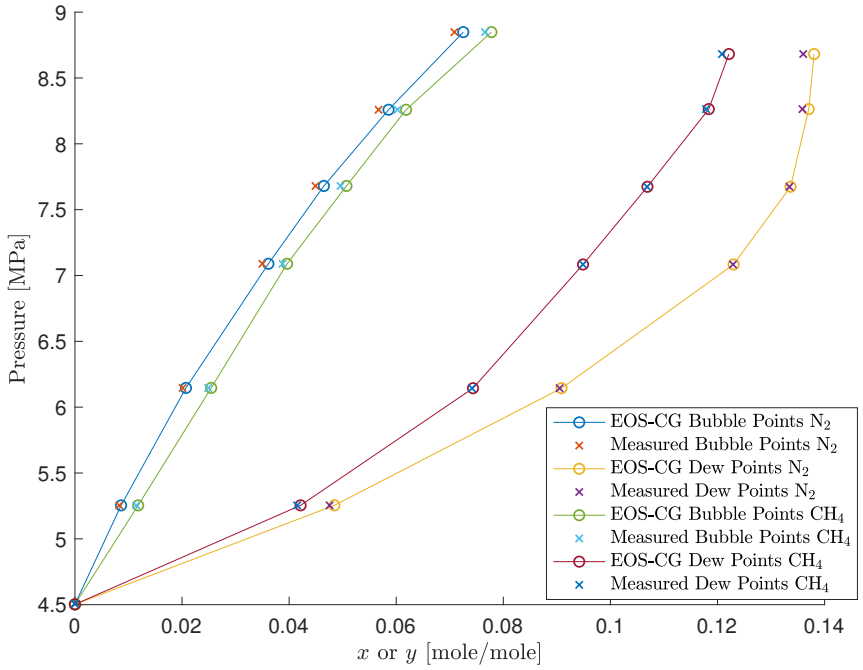

Figure 5.6: Measurements performed at 283 K (L10-L15 and V10-V15) with z_{N_2}:z_{CH_4}≈1:1, together with EOS-CG 2019 prediction. The pressure is plotted versus mole fraction of N_2 and CH_4.

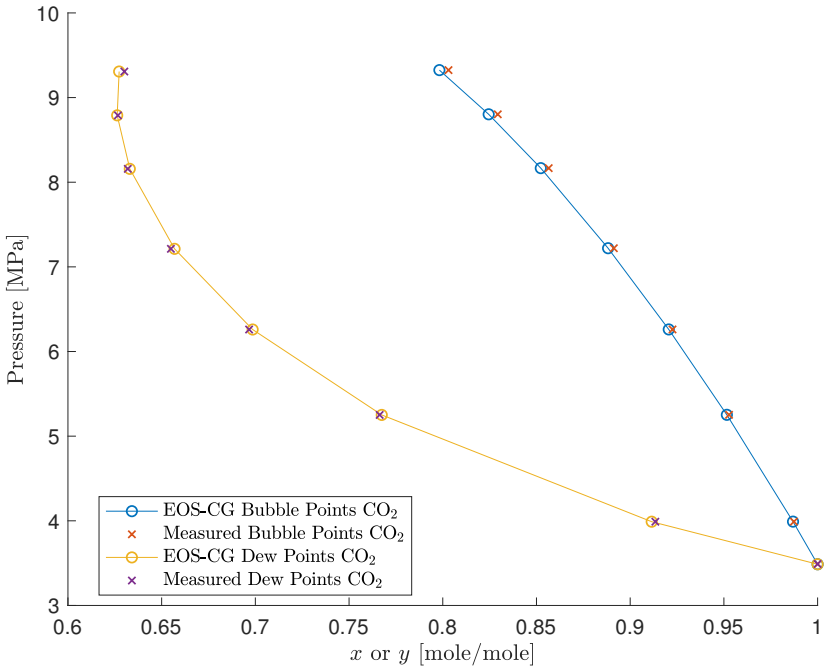

Figure 5.7: Measurements performed at 273 K (L16-L22 and V16-V22) with z_{N_2}:z_{CH_4}≈1:1, together with EOS-CG 2019 prediction. The pressure is plotted versus mole fraction of CO_2.

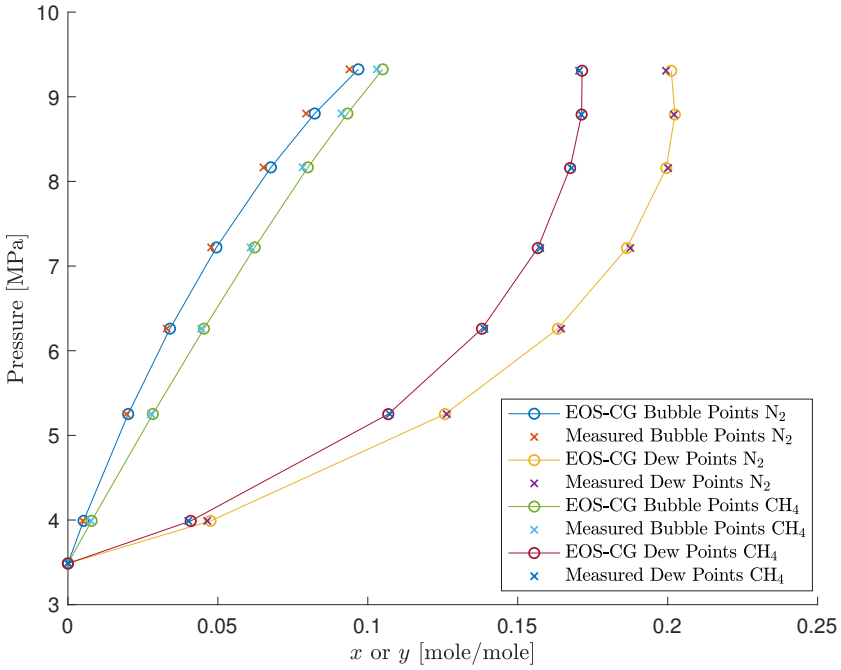

Figure 5.8: Measurements performed at 273 K (L16-L22 and V16-V22) with z_{N_2}:z_{CH_4}≈1:1, together with EOS-CG 2019 prediction. The pressure is plotted versus mole fraction of N_2 and CH_4.

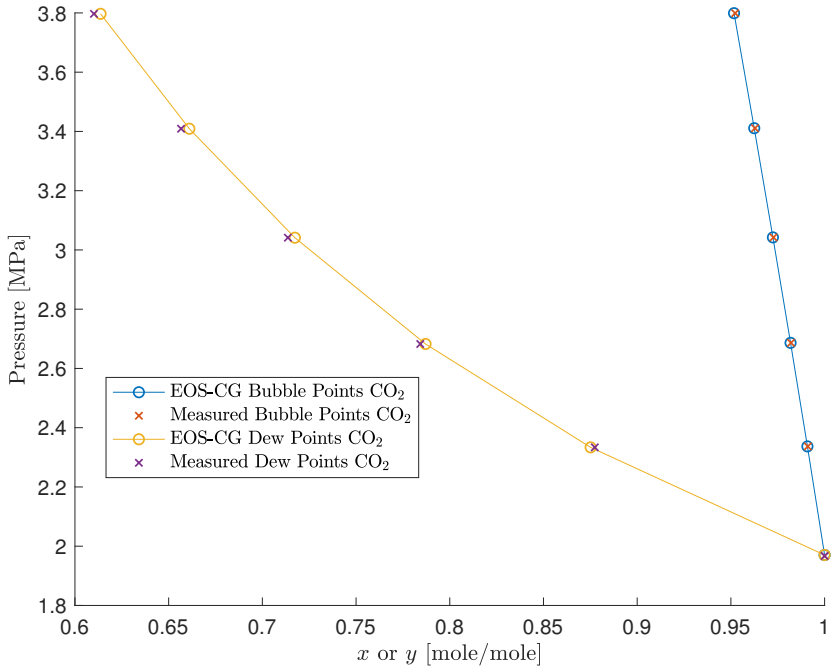

Figure 5.9: Measurements performed at 253 K (L23-L27 and V23-V27) with z_{N_2}:z_{CH_4}≈1:1, together with EOS-CG 2019 prediction. The pressure is plotted versus mole fraction of CO_2.

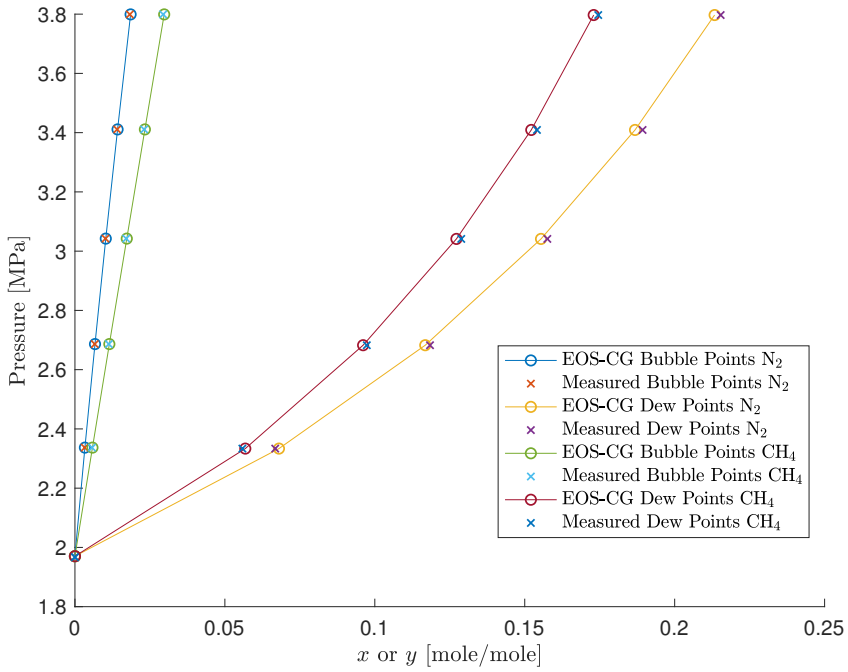

Figure 5.10: Measurements performed at 253 K (L23-L27 and V23-V27) with z_{N_2}:z_{CH_4}≈1:1, together with EOS-CG 2019 prediction. The pressure is plotted versus mole fraction of N_2 and CH_4.

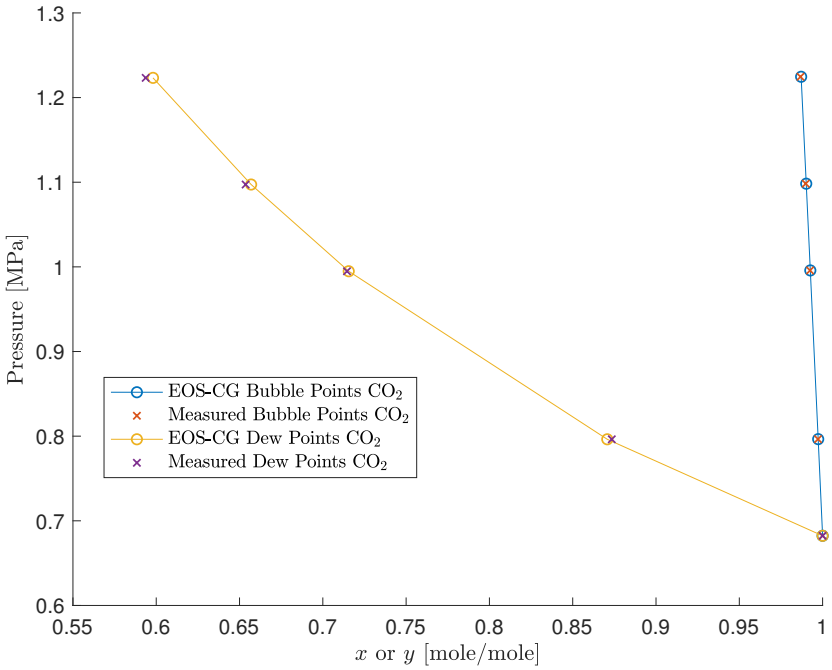

Figure 5.11: Measurements performed at 223 K (L28-L31 and V28-V31) with z_{N_2}:z_{CH_4}≈1:1, together with EOS-CG 2019 prediction. The pressure is plotted versus mole fraction of CO_2.

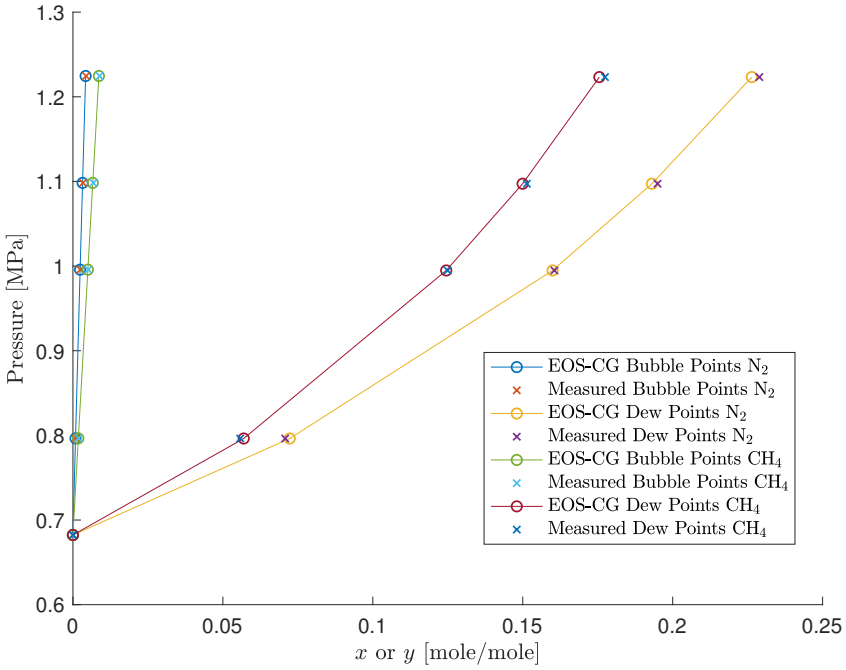

Figure 5.12: Measurements performed at 223 K (L28-L31 and V28-V31) with z_{N_2}:z_{CH_4}≈1:1, together with EOS-CG 2019 prediction. The pressure is plotted versus mole fraction of N_2 and CH_4.

Figures 5.1 to 5.12 provide a comparison between the model and the experimental measurements that makes it easy to relate the measurements to the phase envelope. However, many of the residuals between model and measurement are too small to see. Therefore, residual plots are provided in Figures 5.13, 5.14 and 5.15. Figure 5.13 shows the residuals as a function of pressure, while 5.14 and 5.15 shows the residuals for all the components in chronological order (L1,L2, etc.) for bubble and dew points, respectively.

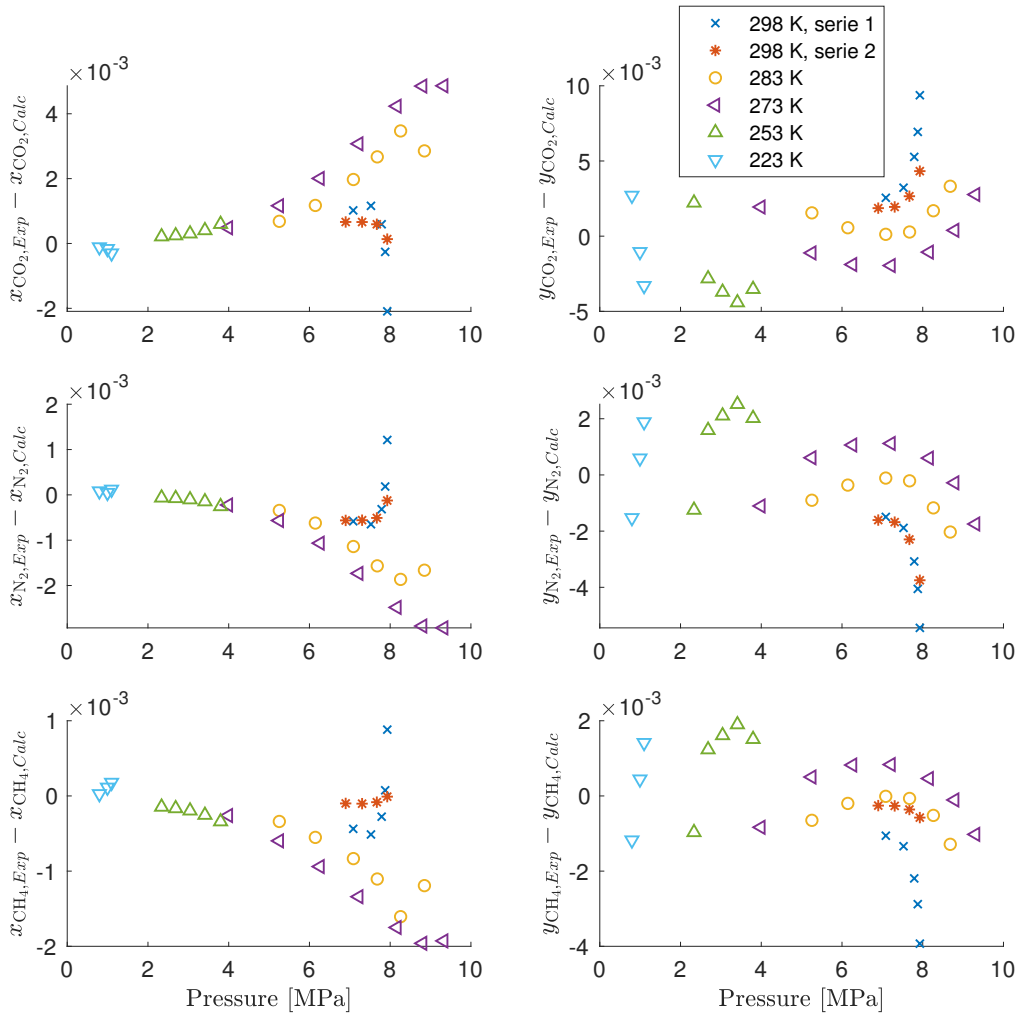

Figure 5.13: Residuals in composition between experimental measurements and EOS-CG 2019 plotted versus the measured pressure. The component and phase (x for liquid phase and y for vapor phase mole fractions) are specified on the axis.

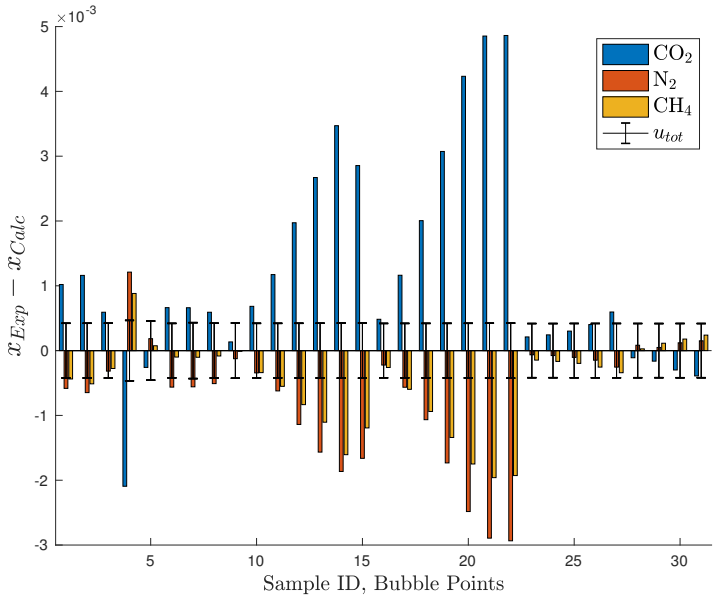

Figure 5.14: Residuals in composition between experimental measurements and EOS-CG 2019 of the bubble points together with the standard total uncertainty, plotted versus the sample ID (see table 5.1).

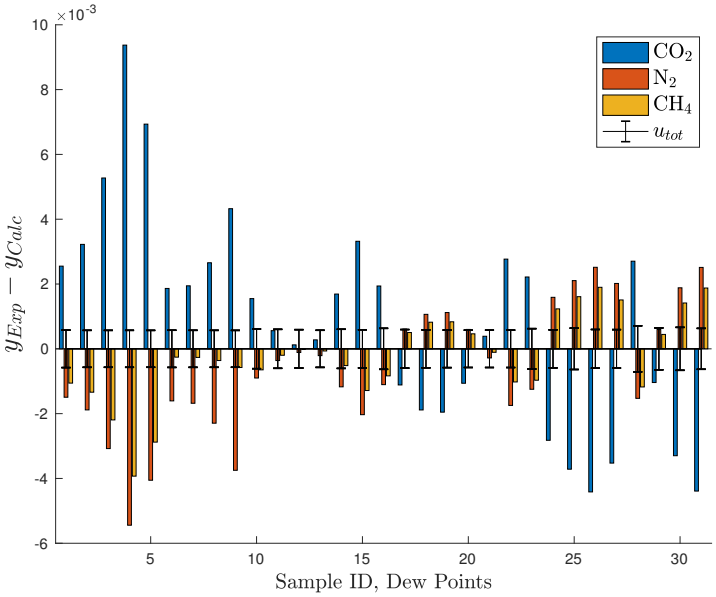

Figure 5.15: Residuals in composition between experimental measurements and EOS-CG 2019 of the dew points together with the standard total uncertainty, plotted versus the sample ID (see table 5.2).

In general, all residuals in liquid composition are lower than 0.5 mole% and all residuals in vapor composition are lower than 1 mole%. This verifies that the model performs well for the ternary mixture, by combining the Helmholtz energy contributions of the three binary systems CO_2-N_2, CO_2-CH_4, and N_2-CH_4 and the contributions of the three pure components CO_2, N_2, and CH_4. The general trend is increasing residuals with increasing pressures and mole fraction of N_2 and CH_4. This is the same trend that has been seen for the binary systems CO_2-N_2 and CO_2-CH_4 in Westman *et al.* (2016) [5] and Petropoulou *et al.* (2018) [6]. The residuals between experimental measurements and EOS-CG 2019 from Westman *et al.* (2016) and Petropoulou *et al.* (2018) are shown in Figure 5.16, plotted on the same axis as the residuals of this work (Figure 5.13). The measurements performed at 223 K by Westman *et al.* (2016) are excluded from the figure because the residuals at this isotherm and high pressures where one order of magnitude higher than at the other isotherms, making the trends of the other isotherms difficult to see.

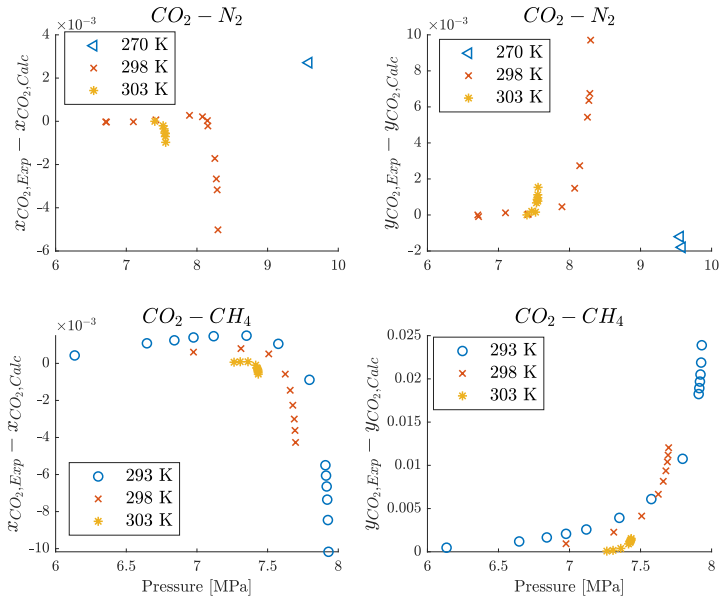

Figure 5.16: Residuals in mole fraction of CO_2 between experimental measurements on the binary mixture of CO_2-N_2 from Westman *et al.* (2016) (two top figures) and the binary mixture of CO_2-CH_4 Petropoulou *et al.* (2018) (two bottom figures), and EOS-CG 2019. The residuals are plotted versus the measured pressure. The component and phase (x for liquid phase and y for vapor phase mole fractions) are specified on the axis.

Figures 5.1 (298 K, CO_2), 5.5 (283 K, CO_2) and 5.7 (273 K, CO_2) illustrate how the model struggles to fit the steep curvature of the phase envelope at pressures close to the critical point. This is in particular evident for the 298 K series 1 measurements in Figure 5.1, which is the series where the measurements were performed closest to the critical point. This shows that the trend in residuals for the ternary mixture follows the trend of the binary mixtures close to the critical point.

The model generally matches the bubble point measurements better than the dew point measurements, which is also the same trend that has been seen for the binary systems. The residual plots in Figure 5.13 indicates that the model mostly matches the bubble points better at higher

temperatures and given pressure. The dew points are difficult to compare across isotherms because the measurements were performed at different states in the phase envelope. However, the 273 K, 283 K, and 298 K isotherms indicate that the model overestimates the mole fraction of CO_2 at 273 K and underestimates it at 298 K, before the phase envelope starts to close again at higher pressures.

Figures 5.14 and 5.15 show the residual in all components together with the standard total uncertainty. The Figures show that the residual between model and experimentally measured bubble points is not statistically significant at 223 K and 253 K. Taking into account that the states measured at 223 K and 253 K were in the bottom corner of the phase envelope, this is in line with the expectation that the model performs well for the lower pressure states in the phase envelope. By studying Figures 5.9 and 5.11, the linear behavior of the bubble points is evident. It therefore makes sense that the model predicts these points well. Most of the dew points at 223 K and 253 K on the other hand, are statistically significantly deviating. In fact, the dew points deviate more at 223 K and 253 K than at 273 K and 283 K. The dew points at these temperatures are not directly comparable since the dew point at 273 K and 283 K are measured at far higher pressures and closer to the critical point. However, it seems to be a trend that the model overestimates the mole fraction of CO_2 at low pressures in the phase envelope to compensate for the steeper curvature at higher pressures. Once the mole fraction of CO_2 in the vapor phase starts to increase with increasing pressure, towards the top of the phase envelope (see Figure 5.7), the model underestimates the mole fraction of CO_2 again. However, for both series at 298 K, the model seems to be constantly underestimating y_{CO_2}. This is also illustrated in the residual plot in Figure 5.15. Notice that the pressure increment from saturation pressure of CO_2 to the first VLE measurement is big compared to the other isotherms and the relative size of the phase envelope. Therefore, it can not be excluded that the model also overestimates y_{CO_2} closer to the saturation pressure of CO_2 at 298 K. Figure 5.14 illustrates that the bubble points deviate the most at 273 K and 283 K. At these temperatures, the model clearly overestimates x_{CO_2}. This is the same trend as for the two series at 298 K at lower pressures, while the model starts underestimating x_{CO_2} at the two highest measurements in series one and the highest in series two. This is also in line with what has been reported for the binary systems CO_2-N_2 and CO_2-CH_4 [5] [6].

Section 2.2.2 describes how the model for multicomponent mixtures are constructed. It combines the pure contributions, $\alpha^r_{o,j}$, from all the components, in this case CO_2, N_2 and CH_4, and the binary specific contributions, $\alpha^r_{i,j}$, from all the binary combinations, in this case CO_2-N_2, CO_2-CH_4 and N_2-CH_4. This is shown in equation 2.12 to 2.15. These equations also show that the mole fraction of each component weight the pure contribution of that component. The binary combination contributions, $\alpha^r_{i,j}$, are weighted by the product of the mole fractions of the components, $x_i x_j$. Furthermore, the binary specific contributions also depend on the reduced temperature and reduced density of the binary mixture, which again are calculated with the molar composition of the mixture, as stated in equations 2.17 and 2.18. As mentioned in the introduction, the fundamental assumption of the model is that multi-component mixtures can be modeled purely based on binary mixture and pure component contributions. The scope of this work is to experimentally verify this fundamental assumption. For all measurement series, except series 2 at 298 K, the ratio between total composition of N_2 and CH_4 was kept approximately at 1:1. Hence, the model combines the CO_2-N_2 and CO_2-CH_4 binary contributions with approximately equal weight. In the three-dimensional phase envelope, visualized in Figure 2.5,

the states measured would therefore be approximately half-way between the x and y axis of the figure. Using this visualization, the phase envelope at the x and y axis will represent the binary phase envelopes of the binary mixtures CO_2-N_2 and CO_2-CH_4. Therefore, the measurements performed with $z_{N_2} : z_{CH_4} \approx 1{:}1$ will be the furthest distance away from the binary mixtures as possible in this three dimensional space. The measurements at $z_{N_2} : z_{CH_4} \approx 1{:}1$ will therefore represent states were the interpolation of the binary mixture contributions is at it's maximum, given a total mole fraction of CO_2. The residuals presented in this work for series 1 at 298 K and all the measurements at 283 K, 273 K, 253 K and 223 K therefore indicate how well the model combination of binary mixture contributions perform at the worst, given that the models for the binary mixtures are equally accurate.

Series 2 at 298 K was measured keeping $z_{N_2} : z_{CH_4} \approx 4.4{:}1$. In other words, the amount of nitrogen was dominating over the amount of methane. The state of the ternary mixture would therefore be closer to the CO_2-N_2 than the CO_2-CH_4 binary mixture. Hence, the interpolation would be smaller and a more accurate fit was expected. By studying Figure 5.13, the residuals as a function of pressure in both phases and for all components can be assessed. For CO_2, the residuals are slightly smaller for series 2 compared to series 1, as expected. For nitrogen, they are approximately the same, while for methane they are smaller for series 2 compared of series 1. Again, it is hard to compare the measurements directly since the critical region will be higher for series 2 than for series 1, due to the higher nitrogen content of series 2. This is evident in Figures 5.1 to 5.4, where series one start to curve towards higher y_{CO_2} above 7.8 MPa while series 2 does not have the same curvature. The effect of varying the ratio between N_2 and CH_4 therefore remains inconclusive. To investigate this further, more measurements are needed at several different total compositions.

Overall, the deviations between model and experimental measurements follow the same trends as for the binary systems CO_2-N_2 and CO_2-CH_4. The residuals are all below 0.5 and 1 mole percent for bubble and dew points respectively. Hence, the accuracy of the model is high for the ternary mixture CO_2-N_2-CH_4. To a large extent, the VLE measurements performed in this work verifies the fundamental assumption that the physical behaviour of a multi-component mixture can be purely predicted by the pure component and binary mixture contributions. It can not be concluded whether the total mole fraction of each of the components affects the accuracy significantly. To verify this, more VLE measurements at different total compositions are needed. Future work should also include more measurements at the lowest isotherms, 223 K and 253 K, at higher pressures and higher mole fractions of CO_2 and N_2 to verify the model behaviour and accuracy in these regions. High methane concentrations were not explored due to the explosion limit of methane in the equilibrium cell. If states above the lower explosion limit are explored, adjustments have to be made to make the VLE rig EX-safe. Furthermore, more calibration mixtures with higher contents of methane and nitrogen must be made, more calibration measurements taken, and a new calibration function for composition fitted. As stated above, the results in this work verifies the fundamental assumption of the model described above to a large extent. It should therefore be considered carefully if more measurements on the CO_2-N_2-CH_4 mixture are needed instead of using the VLE apparatus to measure VLE of other mixtures.

5.1.3 Comparison to Literature Data Residuals

Figure 5.17 shows the residuals between experimental measurements and the model prediction for this work and literature data. The literature data measurements have been performed doing several measurements at the same pressure but at different total compositions. The residuals from the measurements of this work seems to be of the same or lower magnitude as the literature data. Hence, even though the measurements are not directly comparable since they are measured at different compositions, temperatures and/or pressures, the measurements of this work seem to be in line with existing literature data.

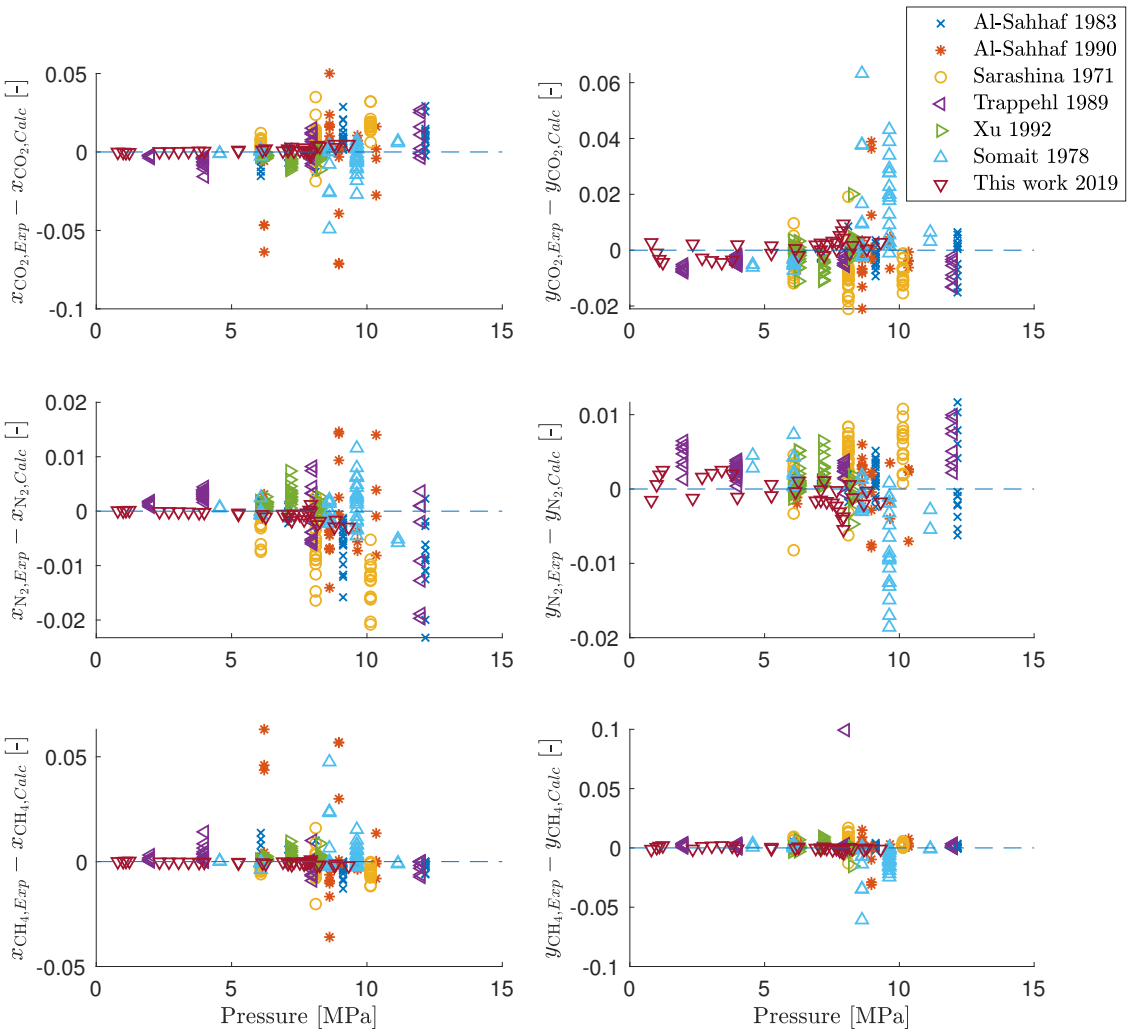

Figure 5.17: Residuals in composition between all available literature experimental data points and EOS-CG 2019 plotted versus the measured pressure. The component and phase (x for liquid phase and y for vapor phase mole fractions) are specified on the axis.

5.2 Visualization of the Residual Helmholtz Energy for the Mixture of CO_2-N_2-CH_4

The tool developed for visualization of the residual Helmholtz energy, α^r, described in section 4.3 was used to investigate the model behaviour of the ternary mixture of CO_2-N_2-CH_4. The objective was to obtain increased insight in how the combination of the various terms of the pure and binary contributions form the model for the ternary mixture. The results are discussed in this section.

Figure 5.18 shows the contributions from the pure components in the ternary mixture, $\alpha^r_{0,i}$, for CO_2, N_2, and CH_4. The residual Helmholtz energy is plotted as a function of temperature and mole fraction of CO_2 in the mixture, with constant density of 20 mol/dm^3 and constant ratio between the mole fraction of N_2 and CH_4, x_{N_2}:x_{CH_4}=1. Hence, a mole fraction of 0.6 for CO_2 implicitly specifies the mole fraction of both N_2 and CH_4 to 0.2. Notice that the composition of the mixture indirectly affects the residual Helmholtz energy through the reducing functions presented in equations 2.17 and 2.18. The contributions to the residual Helmholtz energy from each component have the same shape and magnitude. Thus, they seem to be of approximately equal importance in the pure component part of the residual Helmholtz energy of the ternary mixture, α^r_0. Other densities and compositions were also tested, resulting in the same conclusions. Figures showing each component contribution separately can be found in appendix A4.

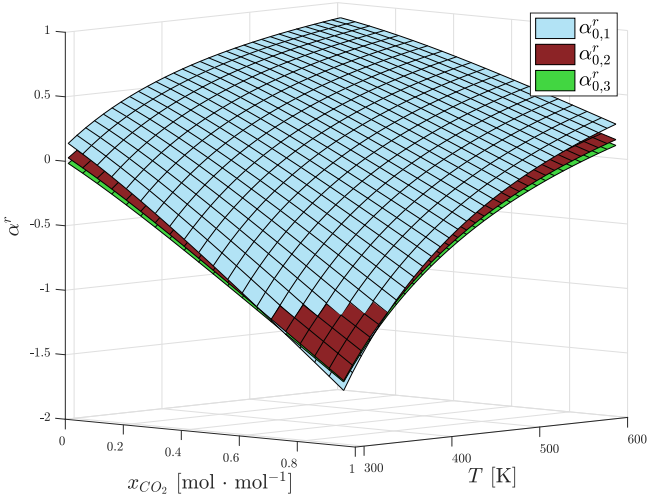

Figure 5.18: The residual Helmholtz energy contribution from the pure components in the ternary mixture of CO_2-N_2-CH_4, referred to as component 1, 2, and 3 in the figure, respectively. Mole fraction of CO_2, x_{CO_2}, and temperature, T, on the x- and y-axis with the ratio between mole fraction of N_2 and CH_4 constant and equal to 1, x_{N_2}:x_{CH_4}=1, and density constant and equal to 20 mol/dm^3.

The departure functions of the residual Helmholtz energy for each binary combination multiplied with the mole fractions of both components, $x_i x_j \alpha^r_{i,j}$, are plotted in figure 5.19 as a function of temperature and mole fraction of CO_2. Density is held constant at 20 mol/dm^3 and the ratio between the mole fraction of N_2 and CH_4 held constant at 1. Hence, 0 mole fraction of CO_2 implies that the mixture contain 50 mole% N_2 and 50 mole% CH_4. With 0 mole% CO_2, the N_2-CH_4 binary contribution, $x_2 x_3 \alpha^r_{2,3}$ is solely dominating. However, for mixtures with more than 50 mole% CO_2 the N_2-CH_4 contribution is one order of magnitude smaller than the CO_2-N_2 and CO_2-CH_4 contributions. Interestingly, the CO_2-N_2 contribution is significantly larger than the CO_2-CH_4 contribution, even though the mole fraction of N_2 and CH_4 are equal. This indicate a stronger impact of the CO_2-N_2 departure function than the CO_2-CH_4 departure function. The departure term is constructed of polynomial, exponential and special exponential

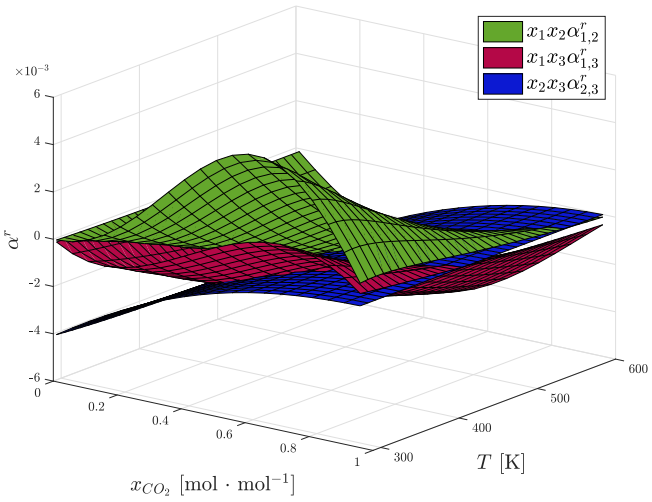

Figure 5.19: The departure terms of the residual Helmholtz energy in the mixture of CO_2-N_2-CH_4, $\alpha^r_{1,2}$, $\alpha^r_{1,3}$, and $\alpha^r_{2,3}$, multiplied by the mole fractions of the respective components. Mole fraction of CO_2, x_{CO_2}, and temperature, T, on the x- and y-axis with the ratio between mole fraction of N_2 and CH_4 constant and equal to 1, x_{N_2}:x_{CH_4}=1. CO_2, N_2 and CH_4 are referred to as component 1, 2, and 3, respectively.

terms as described in equation 2.16. $\alpha^r_{CO_2,N_2}$, $\alpha^r_{CO_2,CH_4}$, and $\alpha^r_{N_2,CH_4}$, consist of 2, 3, and 2 polynomial terms and 4, 3, and 7 special exponential terms, respectively. The sums of the polynomial and special exponential terms multiplied with the respective mole fractions from each binary combination are plotted in Figure 5.20 and Figure 5.21, respectively. They illustrates that the polynomial terms have significantly larger effect than the special exponential terms. As a consequence, the trends seen in the departure functions of each binary contribution are heavily dependent on the sum of the polynomial terms. Figures showing each term separately can be found in appendix A5.

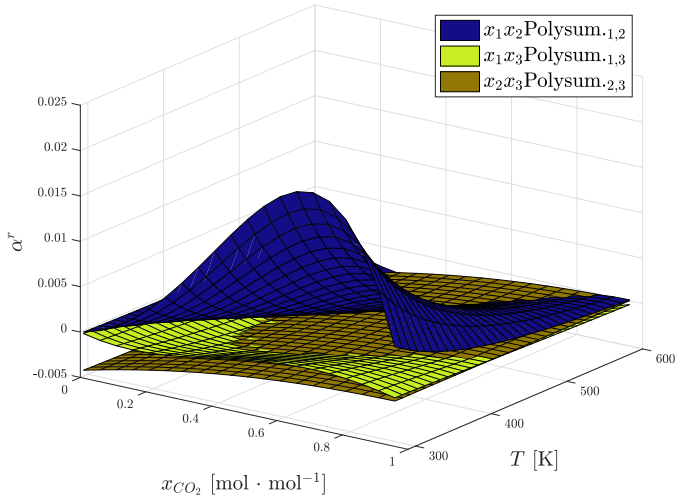

Figure 5.20: The sum of the polynomial terms of the binary combinations CO_2-N_2 (Polysum$_{1,2}$), CO_2-N_2 (Polysum$_{1,3}$), and N_2-CH_4 (Polysum$_{2,3}$), multiplied by the mole fractions of the respective components. Mole fraction of CO_2, $x_{\mathrm{CO_2}}$, and temperature, T, on the x- and y-axis with the ratio between mole fraction of N_2 and CH_4 constant and equal to 1, $x_{\mathrm{N_2}}$:$x_{\mathrm{CH_4}}$=1. CO_2, N_2 and CH_4 are referred to as component 1, 2, and 3, respectively.

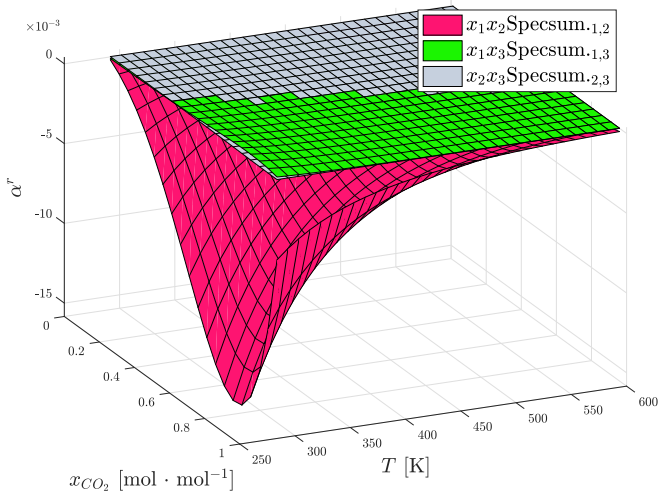

Figure 5.21: The sum of the special exponential terms of the binary combinations CO_2-N_2 (Specsum.$_{1,2}$), CO_2-N_2 (Specsum.$_{1,3}$), and N_2-CH_4 (Specsum.$_{2,3}$), multiplied by the mole fractions of the respective components. Mole fraction of CO_2, $x_{\mathrm{CO_2}}$, and temperature, T, on the x- and y-axis with the ratio between mole fraction of N_2 and CH_4 constant and equal to 1, $x_{\mathrm{N_2}}$:$x_{\mathrm{CH_4}}$=1. CO_2, N_2 and CH_4 are referred to as component 1, 2, and 3, respectively.

Since the departure term in a mixture is affected by the reducing functions given in equation 2.17 and 2.18, the departure functions from the binary combinations, $\alpha^r_{i,j}$, will be different in a ternary mixture and a binary mixture with component i and j. The difference between the departure functions in the ternary and the binary mixtures was therefore inspected qualitatively by visualizing the departure term in the binary mixtures on the same axis as previously done for the ternary mixture (see Figure 5.19). The plots are shown in Figures 5.22, 5.23, and 5.24.

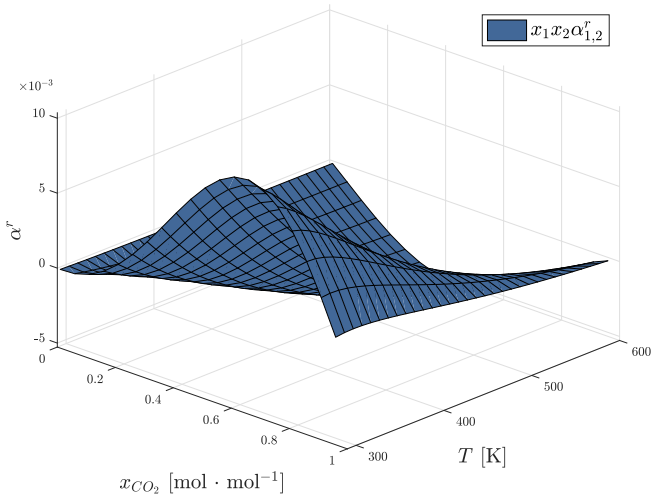

Figure 5.22: The departure term of the residual Helmholtz energy in the binary mixture of CO_2-N_2, $\alpha_{1,2}$, multiplied by the mole fractions of CO_2 and N_2, x_1x_2. Mole fraction of CO_2, x_{CO_2}, and temperature, T, on the x- and y-axis.

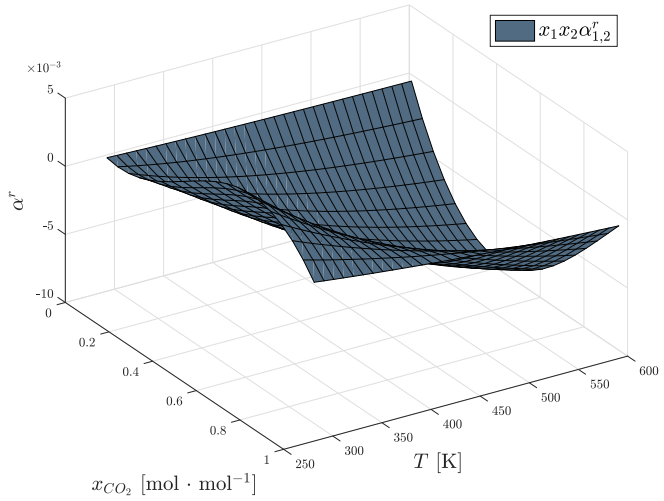

Figure 5.23: The departure term of the residual Helmholtz energy in the binary mixture of CO_2-CH_4, $\alpha_{1,2}$, multiplied by the mole fractions of CO_2 and CH_4, x_1x_2. Mole fraction of CO_2, x_{CO_2}, and temperature, T, on the x- and y-axis.

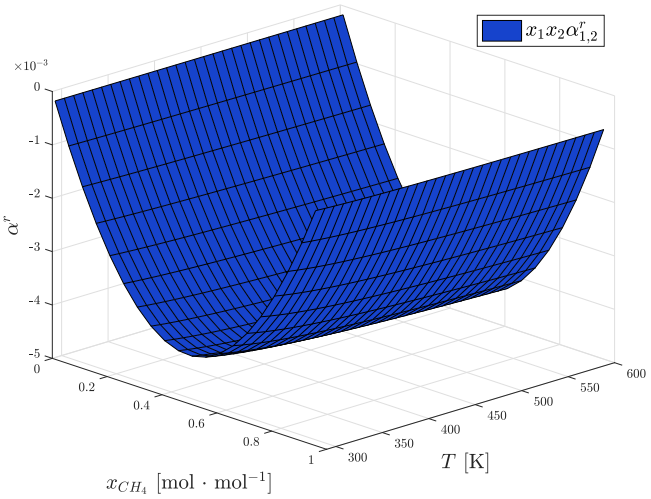

Figure 5.24: The departure term of the residual Helmholtz energy in the binary mixture of CH_4-N_2, $\alpha_{1,2}$, multiplied by the mole fractions of CH_4 and N_2, x_1x_2. Mole fraction of CH_4, z_{CH_4}, and temperature, T, on the x- and y-axis.

The shape of $x_{CO_2}x_{N_2}\alpha^r_{CO_2,N_2}$ in the binary mixture CO_2-N_2 are shown in figure 5.22, plotted versus temperature and mole fraction of CO_2. It is qualitatively similar to the departure function of the binary combination CO_2-N_2 in the ternary mixture of CO_2-N_2-CH_4. Notice that a given mole fraction of CO_2 in Figure 5.19 (the ternary mixture) implies half the amount of N_2 as a given mole fraction of CO_2 in Figure 5.22 (the binary mixture of CO_2-N_2), since the ternary mixture contains CH_4 in addition to CO_2 and N_2. Thus, $x_{CO_2}x_{N_2}\alpha^r_{CO_2,N_2}$ in the ternary mixture is approximately half of $x_{CO_2}x_{N_2}\alpha^r_{CO_2,N_2}$ in the binary mixture. For the binary mixture of CO_2-CH_4, see Figure 5.23, the shape is also qualitatively similar to the shape of $x_{CO_2}x_{CH_4}\alpha^r_{CO_2,CH_4}$ in the ternary mixture. For the binary mixture of CH_4-N_2, the shape shown in Figure 5.24 looks very different from the binary contribution of CH_4-N_2 in the ternary mixture shown in Figure 5.19. However, this is because the binary mixture of CH_4-N_2 cannot be plotted on a x_{CO_2}-T-grid, since there is no CO_2 in this mixture. It was therefore plotted on a x_{CH_4}-T-grid. Hence, the $x_{N_2}x_{CH_4}\alpha^r_{N_2,CH_4}$-term in the binary mixture (Figure 5.24) at 0.5 mole fraction of CH_4 and N_2 should be compared to the $x_{N_2}x_{CH_4}\alpha^r_{N_2,CH_4}$-term in the ternary mixture (Figure 5.19) at 0 mole fraction of CO_2 and 0.5 mole fraction of N_2 and CH_4. Here, the terms look qualitatively the same, with little variation as a function of temperature and magnitude of approximately -0.0045. As the mole fraction of CO_2 in the ternary mixture increases, the mole fractions of N_2 and CH_4 decrease in equal ratio. It therefore makes sense that the temperature dependency of the $x_{N_2}x_{CH_4}\alpha^r_{N_2,CH_4}$-term in the ternary mixture remains the same for various mole fractions of CO_2, but decreases in magnitude toward 0 at 100 mole% CO_2.

Overall, the contributions from pure components and binary combinations in the ternary mixture of CO_2-N_2-CH_4 are in line with the expected model behaviour based on the equations presented in section 2.2.2. The most surprising finding was that the binary contributions to the ternary mixture are significantly different in magnitude. In particular, it is interesting that the contribution from the CO_2-N_2 binary combination, $x_{CO_2}x_{N_2}\alpha^r_{CO_2,N_2}$, is more than twice as large than the contribution from the CO_2-CH_4 binary combination, $x_{CO_2}x_{CH_4}\alpha^r_{CO_2,CH_4}$, even though the mole fractions of N_2 and CH_4 are equal. This indicates that the CO_2-N_2 binary combination has

the most influence on the model of the three binary combinations in CO_2-rich mixtures of the ternary mixture of CO_2-N_2-CH_4. However, it should be noted that all the terms in the Helmholtz energy based model are purely empirical and therefore does not have a physical meaning. In other words, the CO_2-N_2 binary combination has the most influence on the model of CO_2-rich mixtures of the ternary mixtures of CO_2-N_2-CH_4, but the CO_2-N_2 interaction does not necessarily have the strongest impact on the physics of the ternary mixture. Another finding is that for CO_2-rich CO_2-N_2-CH_4-mixtures, the contributions from the binary combinations CO_2-N_2 and CO_2-CH_4 are much larger than the contribution from the binary combination of N_2-CH_4 to the residual Helmholtz energy. This is in line with the reported residuals in section 5.1, where the residuals between experimental point and model prediction to a large extent follow the same trends in the ternary mixture of CO_2-N_2-CH_4 and the binary mixtures of CO_2-N_2 and CO_2-CH_4.

In this work, the impact of the various terms contributing to the residual Helmholtz energy have been studied briefly and qualitatively. Future work should include further investigation of the terms of the residual Helmholtz energy of multicomponent mixtures. The visualization tool could be used to perform similar studies for other multicomponent mixtures. For example, it would be interesting to see how the contribution from binary mixtures fitted to large amounts of data differs from the contribution from binary mixtures fitted to small amounts of data in multicomponent mixtures. The visualization tool could also be used in the fitting of new binary mixtures to existing data, by checking the impact of the binary contribution terms on the prediction of states in multicomponent mixtures. Thus, the visualization tool can hopefully be of help for future work on binary mixtures as well as multicomponent mixtures.

Chapter 6

Conclusion

The vapor liquid equilibrium (VLE) facility in the Sintef Energy lab has been used to measure a total of 31 bubble and 31 dew points of the ternary mixture CO_2-N_2-CH_4 at the temperatures 223 K, 253 K, 273 K, 283 K, and 298 K and pressures in the range of 0.8 MPa to 9.3 MPa. The temperature sensors, pressure sensors, and the gas chromatograph have been calibrated in-house and a thorough quantitative uncertainty analysis has been performed. The reported standard uncertainty in temperature and pressure is lower than 14 mK and 1.5 kPa, respectively. The standard uncertainty of the composition of each component is lower than 0.05 and 0.06 mole percent for bubble and dew points, respectively. The total standard uncertainty has been estimated in terms of composition to be lower than 0.05 and 0.07 mole percent for bubble and dew points, respectively. The results were compared to the state-of-the-art Helmholtz energy based equation of state for the the CO_2-N_2-CH_4-mixture, the EOS-CG 2019 model. The deviations between the experimentally measured points and the model prediction are lower than 0.5 and 1 mole percent for all bubble and dew points respectively. In general, the model prediction is better at lower pressures and lower composition of N_2 and CH_4. Furthermore, the deviations between model and experimental point in the ternary mixture CO_2-N_2-CH_4 follow the same trends seen in literature between model and experimental point in the binary mixtures CO_2-N_2 and CO_2-CH_4. Hence, the reported results verify that the accuracy of the model of multicomponent mixtures are strongly related to the accuracy of the model for the binary mixtures of the involved components. Future work can include more VLE measurements at lower temperatures and higher pressures and mole fractions of CO_2 and N_2, to verify the accuracy of the model in the regions that were not measured during this work.

In summary, the results presented in this work verify that the state-of-the-art Helmholtz energy based equation of state for the ternary mixture of CO_2-N_2-CH_4, EOS-CG 2019, predicts the VLE with the same magnitude of accuracy as it was fitted for the CO_2-N_2 and CO_2-CH_4 binary mixtures at the states measured in this work. One of the fundamental assumptions of the Helmholtz energy based equations of state for multicomponent mixtures is that the behaviour of a multicomponent mixture can be purely predicted by pure component and binary mixture contributions. To a large extent, the results and discussion presented in this work validates that fundamental assumption for the ternary mixture of CO_2-N_2-CH_4.

Bibliography

[1] Roland Span and W. Wagner. A New Equation of State for Carbon Dioxide Covering the Fluid Region from the Triple-Point Temperature to 1100 K at Pressures up to 800 MPa. *Journal of Physical and Chemical Reference Data*, 6:1509–1596, 1996.

[2] O. Kunz and W. Wagner. The GERG-2008 Wide-Range Equation of State for Natural Gases and Other Mixtures. *J. Chem. Eng. Data*, 11:3032–3091, 2012.

[3] S.W. Løvseth, H.G.J. Stang, S.F. Westman, I. Snustad, and Austegard A. Experimental investigations of impurity impact on CO2 mixture phase equilibria. *Energy Procedia Equilibria*, 63:2589–2595, 2014.

[4] S. Herrig. *New Helmholtz-Energy Equations of state for Pure Fluids and CCS-Relevant Mixture*. PhD thesis, Ruhr-University Bochum, 2018.

[5] S.F Westman, H.G.J. Stang, S.W. Løvseth, A. Austegard, and S.Ø. Størset. Vapor-liquid equilibrium data for the carbon dioxide and nitrogen (CO2-N2) system at the temperatures 223, 270, 298 and 303 K and pressures up to 18 MPa. *Fluid Phase Equilibria*, 409:207–241, 2014.

[6] E. Petropoulou, E. Voutsas, S.F Westman, A. Austegard, H.G.J. Stang, and S.W. Løvseth. Vapor-liquid equilibrium of the carbon dioxide/methane mixture at three isotherms. *Fluid Phase Equilibria*, 462:44–58, 2018.

[7] The Intergovernmental Panel on Climate Change (IPCC), Special Report: Global Warming of 1.5 °C. `https://www.ipcc.ch/sr15/`. Accessed: 2019-04-01.

[8] The Intergovernmental Panel on Climate Change (IPCC), Special Report: Global Warming of 1.5°C. `https://www.ipcc.ch/sr15/`. Chapter 2 - Mitigation pathways compatible with 1.5 °C in the context of sustainable development. Page 160. Accessed: 2019-04-01.

[9] Norwegian water resources and energy directorate (NVE): Electricity disclosure 2015. `https://www.nve.no/energy-market-and-regulation/retail-market/electricity-disclosure-2015/`. Accessed:2019-04-02, Last Updated: 2019-04-01.

[10] U.S. Energy Information Administration: Frequently Asked Question: How much electricity does an American home use? `https://www.eia.gov/tools/faqs/faq.php?id=97&t=3`. Accessed:2019-04-02, Last Updated: 2018-10-26.

[11] International Energy Agency (IEA): World Energy Outlook 2018. https://www.iea.org/weo/. Accessed: 2019-04-02, Last Updated: 2019-04-01.

[12] A. Morin (SINTEF Energy Reasearch): IMPACTS - The impact of the quality of CO2 on transport and storage behaviour, Leading the way in CCS implementation event, London, 14-15 April 2014. https://www.slideshare.net/UKCCSRC/a-morin-impactsfp714april2014. Accessed 2019-04-02.

[13] The Norwegian Oil and Energy Department: CO2-håndtering i Norge. https://www.regjeringen.no/no/tema/energi/co2-handtering/co2-handtering/id2601471/. Accessed 2019-04-02, Last Updated 15.05.2018.

[14] Equinor, Total, and Shell. Northern Lights - Mottak og permanent lagring av CO2. Forslag til utredningsprogram for konsekvensutredning. https://www.equinor.com/no/how-and-why/impact-assessments/northernlights.html, January 2018.

[15] NCCS: Reasearch and Results. https://www.sintef.no/projectweb/nccs/research/. Accessed 2019-04-02, Last updated 2019-04-02.

[16] Fiscal metering and thermodynamics (Task 8). https://www.sintef.no/projectweb/nccs/research/fiscal-metering-and-thermodynamics/#/. Accessed 2019-04-02, Last updated 2019-04-02.

[17] S.F Westman, H.G.J. Stang, S.W. Løvseth, A. Austegard, I. Snustad, and I.S. Ertesvåg. Vapor-liquid equilibrium data for the carbon dioxide and oxygen (CO2-O2) system at the temperatures 218, 233, 253, 273, 288 and 298 K and pressures up to 14 MPa. *Fluid Phase Equilibria*, 421:67–87, 2016.

[18] S.W. Løvseth, A. Austegard, S.F Westman, H.G.J. Stang, S. Herrig, and T. Neumann. Thermodynamics of the carbon dioxice plus argon (CO2 + Ar) system: An impoved reference mixture model and measurements of vapor-liquid, vapor-solid, liquid-solid and vapor-liquid-solid phase equilibrium data at the temperatures 213- 299 K and pressures up to 16 MPa. *Fluid Phase Equilibria*, 466:48–78, 2018.

[19] S.F Westman, A. Austegard, H.G.J. Stang, and S.W. Løvseth. Vapor-liquid equilibrium data for the carbon dioxide and carbon monoxide (CO2+CO) system at the temperature 253, 273, 283 and 298 K and pressures up to 13 MPa. *Fluid Phase Equilibria*, 473:37–49, 2018.

[20] T. Neumann. Development of New Helmholtz Models for Binary Mixtures Relevant for CCS, 2017. Master Thesis, Ruhr-University Bochum.

[21] Tore Haug-Warberg. *Den termodynamiske arbeidsboken*. Kolofon Forlag AS, 2006. Chapter 3, pages 17-25.

[22] J. Gernert and R. Span. EOS-CG: A Helmholtz energy mixture model for humid gases and CCS mixtures. *The Journal of Chemical Thermodynamics*, 93, 05 2015.

[23] T. Neumann, M. Thol, I. H. Bell, E. W. Lemmon, and R. Span. New Equations of State for Binary Mixtures Containing Ammonia and one of Twelve Other Components (Argon, Methane, Hydrogen, Nitrogen, Carbon Monoxide, Chlorine, Diethanolamine, Hydrogen Chloride, Hydrogen Sulfide, Monoethanolamine, Oxygen, and Sulfur Dioxide). *Fluid Phase Equilibria*, 2019. To be submitted.

[24] E. W. Lemmon, I. H. Bell, M.L. Huber, and M. O. McLinden. NIST Standard Reference Database 23: Reference Fluid Thermodynamic and Transport Properties- REFPROP 10.0. 2018.

[25] E. W. Lemmon and R.T. Jacobsen. A Generalized Model for the Thermodynamic Properties of Mixtures. *International Journal of Thermodphysics*, 20:825–835, 1999.

[26] O. Kunz, R. Klimeck, W. Wagner, and M. Jaeschke. *The GERG-2014 Wide-Range Equation of State for Natural Gases and Other Mixtures*. Publishing House of the Association of German Engineers, 2007. Düsseldorf.

[27] M. Helbæk and S. Kjelstrup. *Fysikalsk Kjemi*. Fagbokforlaget Vigmostad Bjørke AS, 1999. Chapter 4, pages 181-187.

[28] C.J. Geankoplis. *Transport Processes & Separation Process Principles (Includes Unit Operations)*. Pearson, 2014.

[29] ENERGY Institute London. Hazard analysis for offshore carbon capture platforms and offshore pipelines. `http://decarboni.se/sites/default/files/publications/115563/hazard-analysis-offshore-platforms-offshore-pipelines.pdf`, 2013.

[30] N. Xu, J. Dong, Y. Wang, and J. Shi. High Pressure Vapor Liquid Equilibria at 293 K for systems containing nitrogen, methane and carbon dioxide. *Fluid Phase Equil.*, 81:175–186, 1992.

[31] Vapor-Liquid Equilibria for the Nitrogen-Methane-Carbon-Dioxide System, journal = Journal of Chemical Engineering of Japan. 4(4):77–78, 1970.

[32] G. Trappehl and H. Knapp. Vapour-liquid equilibria in the ternary mixture N_2-CH_4-CO_2 and the quaternary mixture N_2-CH_4-C_2H_6-C_3H_8. *Cryogenics*, 29:42–50, 1989.

[33] F. A. Somait and A. J. Kidnay. LiquidVapor Equilibria at 270.00 K for Systems Containing Nitrogen, Methane, and Carbon Dioxide. *Chemical Engineering Data*, 23:301–305, 1978.

[34] T.A. Al-Sahhaf, A.J. Kidnay, and E.D. Sloan. Liquid+vapor equilibria in the N_2+CO_2+CH_4 system. *Ind. Eng. Chem. Fundam.*, 22:372–380, 1983.

[35] T.A. Al-Sahhaf. Vapor-Liquid Equilibria for the ternary system N_2+CO_2+CH_4 at 230 K and 250 K. *Fluid Phase Equil.*, 55:159–172, 1990.

[36] H. Preston-Thomas. The International Temperature Scale of 1990 (ITS-90). *Metrologia*, 27:3–10, 1990.

[37] Platinum-Resistance Thermometry at Low Temperatures. *Journal of the American Chemical Society*, 47:326–332, 1925.

[38] ISO 6142:2001. Gas analysis - Preparation of calibration gas mixtures - Gravimetric method. page 18, 2001.

[39] R. Span, E. W. Lemmon, R.T. Jacobsen, W. Wagner, and A. Yokozeki. A Reference Equation of State for the Thermodynamic Properties of Nitrogen for Temperatures from 63.151 to 1000 K and Pressures to 2200 MPa. *J. Phys. Chem. Ref. Data*, 29:1361–1433, 2000.

[40] S. Ottøy and A. Langørgen. Summer report 2018. Can be found on Sharepoint: GT FME NCCS T8 Thermodynamics Metering - VLE 2018. Ask Sintef for permission, August 2018.

Appendix

A1. Complimentary Residual Plots for the Composition Calibration Function

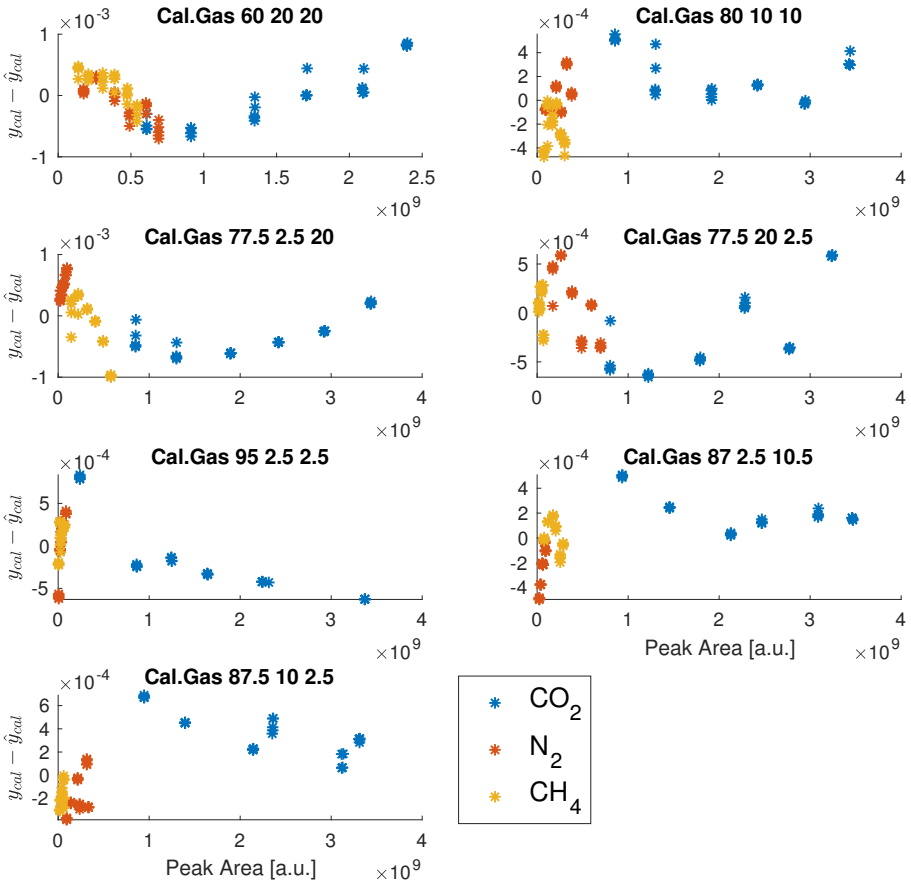

Figure A.1: Residuals between fitted composition calibration function for the liquid sampler and the gravimetrically determined composition of the 7 calibration gases plotted versus peak area. The calibration gas is specified above each sub figure.

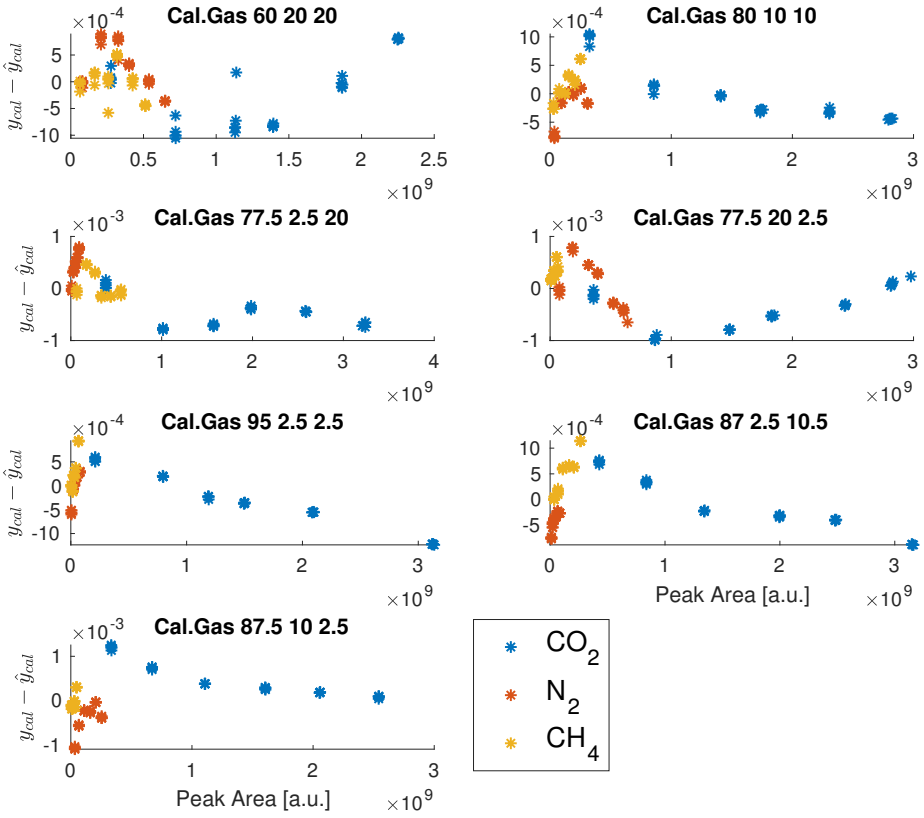

Figure A.2: Residuals between fitted composition calibration function for the vapor sampler and the gravimetrically determined composition of the 7 calibration gases plotted versus peak area. The calibration gas is specified above each sub figure.

A2. Uncertainty Analysis Tables

ID	$u_c(x_{\mathrm{N}_2})$	$u_c(x_{\mathrm{CH}_4})$	$u_c(x_{\mathrm{CO}_2})$	$s(x_{f,\mathrm{N}_2})$	$s(x_{f,\mathrm{CH}_4})$	$s(x_{f,\mathrm{CO}_2})$	$u(x_{f,\mathrm{N}_2})$	$\mathrm{u}(\mathrm{x}_{f,\mathrm{CH}_4})$	$u(x_{f,\mathrm{CO}_2})$	$u_{tot}(x_{\mathrm{N}_2})$	$u_{tot}(x_{\mathrm{CH}_4})$	$u_{tot}(x_{\mathrm{CO}_2})$
L1	3.4E-04	2.7E-04	4.2E-04	2.0E-05	8.8E-06	1.2E-05	3.4E-04	2.7E-04	4.2E-04	3.4E-04	2.7E-04	4.2E-04
L2	3.4E-04	2.7E-04	4.2E-04	1.6E-05	1.2E-05	2.8E-05	3.4E-04	2.7E-04	4.2E-04	3.4E-04	2.7E-04	4.2E-04
L3	3.4E-04	2.7E-04	4.2E-04	1.3E-05	1.1E-05	2.4E-05	3.4E-04	2.7E-04	4.2E-04	3.4E-04	2.7E-04	4.2E-04
L4	3.4E-04	2.7E-04	4.2E-04	1.1E-04	8.3E-05	1.9E-04	3.5E-04	2.8E-04	4.6E-04	3.6E-04	2.9E-04	4.7E-04
L5	3.4E-04	2.7E-04	4.2E-04	9.0E-05	8.0E-05	1.7E-04	3.5E-04	2.8E-04	4.5E-04	3.5E-04	2.9E-04	4.6E-04
L6	3.4E-04	2.7E-04	4.2E-04	1.9E-05	3.8E-06	2.3E-05	3.4E-04	2.7E-04	4.2E-04	3.4E-04	2.7E-04	4.2E-04
L7	3.4E-04	2.7E-04	4.2E-04	8.4E-05	1.6E-05	1.0E-04	3.5E-04	2.7E-04	4.3E-04	3.5E-04	2.7E-04	4.3E-04
L8	3.4E-04	2.7E-04	4.2E-04	3.2E-05	8.2E-06	3.9E-05	3.4E-04	2.7E-04	4.2E-04	3.4E-04	2.7E-04	4.2E-04
L9	3.4E-04	2.7E-04	4.2E-04	5.4E-05	9.2E-06	6.3E-05	3.4E-04	2.7E-04	4.2E-04	3.4E-04	2.7E-04	4.3E-04
L10	3.4E-04	2.7E-04	4.2E-04	9.6E-06	1.1E-05	1.6E-05	3.4E-04	2.7E-04	4.2E-04	3.4E-04	2.7E-04	4.2E-04
L11	3.4E-04	2.7E-04	4.2E-04	5.9E-06	2.5E-06	5.6E-06	3.4E-04	2.7E-04	4.2E-04	3.4E-04	2.7E-04	4.2E-04
L12	3.4E-04	2.7E-04	4.2E-04	7.8E-06	6.0E-06	1.3E-05	3.4E-04	2.7E-04	4.2E-04	3.4E-04	2.7E-04	4.2E-04
L13	3.4E-04	2.7E-04	4.2E-04	8.5E-06	2.3E-06	1.0E-05	3.4E-04	2.7E-04	4.2E-04	3.4E-04	2.7E-04	4.2E-04
L14	3.4E-04	2.7E-04	4.2E-04	8.3E-06	3.5E-05	4.1E-05	3.4E-04	2.7E-04	4.2E-04	3.4E-04	2.8E-04	4.2E-04
L15	3.4E-04	2.7E-04	4.2E-04	6.7E-06	3.6E-06	8.6E-06	3.4E-04	2.7E-04	4.2E-04	3.4E-04	2.7E-04	4.3E-04
L16	3.4E-04	2.7E-04	4.2E-04	2.0E-06	2.2E-06	3.5E-06	3.4E-04	2.7E-04	4.2E-04	3.4E-04	2.7E-04	4.2E-04
L17	3.4E-04	2.7E-04	4.2E-04	4.8E-06	1.8E-06	3.1E-06	3.4E-04	2.7E-04	4.2E-04	3.4E-04	2.7E-04	4.2E-04
L18	3.4E-04	2.7E-04	4.2E-04	1.4E-05	9.7E-06	9.4E-06	3.4E-04	2.7E-04	4.2E-04	3.4E-04	2.7E-04	4.2E-04
L19	3.4E-04	2.7E-04	4.2E-04	1.1E-05	3.6E-06	9.7E-06	3.4E-04	2.7E-04	4.2E-04	3.4E-04	2.7E-04	4.2E-04
L20	3.4E-04	2.7E-04	4.2E-04	1.8E-05	2.3E-05	1.0E-05	3.4E-04	2.7E-04	4.2E-04	3.4E-04	2.7E-04	4.2E-04
L21	3.4E-04	2.7E-04	4.2E-04	1.4E-05	1.3E-05	1.3E-05	3.4E-04	2.7E-04	4.2E-04	3.4E-04	2.7E-04	4.2E-04
L22	3.4E-04	2.7E-04	4.2E-04	9.7E-06	1.2E-05	5.2E-06	3.4E-04	2.7E-04	4.2E-04	3.4E-04	2.7E-04	4.2E-04
L23	3.4E-04	2.7E-04	4.2E-04	8.5E-06	3.4E-06	7.1E-06	3.4E-04	2.7E-04	4.2E-04	3.4E-04	2.7E-04	4.2E-04
L24	3.4E-04	2.7E-04	4.2E-04	8.5E-06	3.9E-06	5.1E-06	3.4E-04	2.7E-04	4.2E-04	3.4E-04	2.7E-04	4.2E-04
L25	3.4E-04	2.7E-04	4.2E-04	9.6E-06	4.1E-06	5.6E-06	3.4E-04	2.7E-04	4.2E-04	3.4E-04	2.7E-04	4.2E-04
L26	3.4E-04	2.7E-04	4.2E-04	1.2E-05	6.5E-06	6.6E-06	3.4E-04	2.7E-04	4.2E-04	3.4E-04	2.7E-04	4.2E-04
L27	3.4E-04	2.7E-04	4.2E-04	6.9E-06	3.4E-06	3.5E-06	3.4E-04	2.7E-04	4.2E-04	3.4E-04	2.7E-04	4.2E-04
L28	3.4E-04	2.7E-04	4.2E-04	1.2E-05	1.2E-05	2.3E-05	3.4E-04	2.7E-04	4.2E-04	3.4E-04	2.7E-04	4.2E-04
L29	3.4E-04	2.7E-04	4.2E-04	7.8E-06	1.5E-05	8.9E-06	3.4E-04	2.7E-04	4.2E-04	3.4E-04	2.7E-04	4.2E-04
L30	3.4E-04	2.7E-04	4.2E-04	1.9E-05	1.2E-05	2.4E-05	3.4E-04	2.7E-04	4.2E-04	3.4E-04	2.7E-04	4.2E-04
L31	3.4E-04	2.7E-04	4.2E-04	1.2E-05	1.2E-05	1.5E-05	3.4E-04	2.7E-04	4.2E-04	3.4E-04	2.7E-04	4.2E-04

Table A.1: Summary of uncertainty analysis for liquid composition.

ID	$u_c(y_{N_2})$	$u_c(y_{CH_4})$	$u_c(y_{CO_2})$	s(y_{f,N_2})	$s(y_{f,CH_4})$	$s(y_{f,CO_2})$	$u(y_{f,N_2})$	u(y_{f,CH_4})	$u(y_{f,CO_2})$	$u_{tot}(y_{N_2})$	$u_{tot}(y_{CH_4})$	$u_{tot}(y_{CO_2})$
V1	4.4E-04	3.3E-04	5.7E-04	8.1E-06	3.7E-06	5.0E-06	4.4E-04	3.3E-04	5.7E-04	4.5E-04	3.4E-04	5.8E-04
V2	4.4E-04	3.3E-04	5.7E-04	3.7E-06	3.4E-06	5.7E-06	4.4E-04	3.3E-04	5.7E-04	4.4E-04	3.3E-04	5.7E-04
V3	4.4E-04	3.3E-04	5.7E-04	4.4E-06	4.5E-06	8.6E-06	4.4E-04	3.3E-04	5.7E-04	4.4E-04	3.3E-04	5.7E-04
V4	4.4E-04	3.3E-04	5.7E-04	1.6E-05	1.8E-05	3.4E-05	4.4E-04	3.3E-04	5.7E-04	4.4E-04	3.3E-04	5.7E-04
V5	4.4E-04	3.3E-04	5.7E-04	6.6E-06	1.4E-05	1.4E-05	4.4E-04	3.3E-04	5.7E-04	4.4E-04	3.3E-04	5.7E-04
V6	4.4E-04	3.3E-04	5.7E-04	1.3E-05	6.3E-06	1.9E-05	4.4E-04	3.3E-04	5.7E-04	4.5E-04	3.3E-04	5.7E-04
V7	4.4E-04	3.3E-04	5.7E-04	1.5E-05	5.4E-06	2.0E-05	4.4E-04	3.3E-04	5.7E-04	4.4E-04	3.3E-04	5.7E-04
V8	4.4E-04	3.3E-04	5.7E-04	3.0E-06	1.7E-06	4.3E-06	4.4E-04	3.3E-04	5.7E-04	4.4E-04	3.3E-04	5.7E-04
V9	4.4E-04	3.3E-04	5.7E-04	3.5E-06	3.7E-06	1.6E-06	4.4E-04	3.3E-04	5.7E-04	4.4E-04	3.3E-04	5.7E-04
V10	4.4E-04	3.3E-04	5.7E-04	3.3E-05	2.8E-05	6.0E-05	4.4E-04	3.3E-04	5.7E-04	4.6E-04	3.5E-04	6.1E-04
V11	4.4E-04	3.3E-04	5.7E-04	3.7E-05	3.5E-05	7.2E-05	4.4E-04	3.3E-04	5.7E-04	4.6E-04	3.4E-04	6.0E-04
V12	4.4E-04	3.3E-04	5.7E-04	4.1E-05	2.4E-05	6.4E-05	4.4E-04	3.3E-04	5.7E-04	4.5E-04	3.4E-04	5.9E-04
V13	4.4E-04	3.3E-04	5.7E-04	1.7E-05	7.8E-06	2.3E-05	4.4E-04	3.3E-04	5.7E-04	4.4E-04	3.3E-04	5.7E-04
V14	4.4E-04	3.3E-04	5.7E-04	6.0E-05	8.5E-05	1.4E-04	4.4E-04	3.4E-04	5.8E-04	4.5E-04	3.5E-04	6.0E-04
V15	4.4E-04	3.3E-04	5.7E-04	1.4E-05	2.3E-05	3.3E-05	4.4E-04	3.3E-04	5.7E-04	4.5E-04	3.4E-04	5.9E-04
V16	4.4E-04	3.3E-04	5.7E-04	7.1E-05	4.0E-05	1.1E-04	4.4E-04	3.3E-04	5.8E-04	4.7E-04	3.5E-04	6.3E-04
V17	4.4E-04	3.3E-04	5.7E-04	2.8E-05	8.7E-06	3.7E-05	4.4E-04	3.3E-04	5.7E-04	4.5E-04	3.4E-04	6.0E-04
V18	4.4E-04	3.3E-04	5.7E-04	3.5E-05	1.8E-05	4.1E-05	4.4E-04	3.3E-04	5.7E-04	4.5E-04	3.4E-04	5.9E-04
V19	4.4E-04	3.3E-04	5.7E-04	1.0E-05	2.8E-05	3.4E-05	4.4E-04	3.3E-04	5.7E-04	4.5E-04	3.4E-04	5.8E-04
V20	4.4E-04	3.3E-04	5.7E-04	3.3E-06	1.5E-05	1.4E-05	4.4E-04	3.3E-04	5.7E-04	4.4E-04	3.3E-04	5.8E-04
V21	4.4E-04	3.3E-04	5.7E-04	1.6E-05	6.6E-06	1.7E-05	4.4E-04	3.3E-04	5.7E-04	4.4E-04	3.3E-04	5.8E-04
V22	4.4E-04	3.3E-04	5.7E-04	7.5E-06	1.4E-05	1.9E-05	4.4E-04	3.3E-04	5.7E-04	4.4E-04	3.3E-04	5.8E-04
V23	4.4E-04	3.3E-04	5.7E-04	1.1E-04	8.7E-05	1.9E-04	4.5E-04	3.4E-04	6.0E-04	4.6E-04	3.5E-04	6.2E-04
V24	4.4E-04	3.3E-04	5.7E-04	5.0E-05	2.7E-05	7.6E-05	4.4E-04	3.3E-04	5.7E-04	4.5E-04	3.4E-04	5.9E-04
V25	4.4E-04	3.3E-04	5.7E-04	1.6E-04	3.4E-05	1.9E-04	4.7E-04	3.3E-04	6.0E-04	4.8E-04	3.5E-04	6.4E-04
V26	4.4E-04	3.3E-04	5.7E-04	3.7E-05	2.8E-05	6.4E-05	4.4E-04	3.3E-04	5.7E-04	4.5E-04	3.4E-04	6.0E-04
V27	4.4E-04	3.3E-04	5.7E-04	5.9E-05	4.5E-05	1.0E-04	4.4E-04	3.3E-04	5.7E-04	4.5E-04	3.4E-04	5.9E-04
V28	4.4E-04	3.3E-04	5.7E-04	1.0E-04	6.1E-05	1.6E-04	4.5E-04	3.4E-04	5.9E-04	5.0E-04	3.8E-04	7.1E-04
V29	4.4E-04	3.3E-04	5.7E-04	8.1E-05	5.9E-05	1.4E-04	4.5E-04	3.4E-04	5.8E-04	4.7E-04	3.6E-04	6.5E-04
V30	4.4E-04	3.3E-04	5.7E-04	7.6E-05	3.7E-05	1.1E-04	4.5E-04	3.3E-04	5.8E-04	4.8E-04	3.6E-04	6.6E-04
V31	4.4E-04	3.3E-04	5.7E-04	4.9E-05	3.3E-05	8.1E-05	4.4E-04	3.3E-04	5.7E-04	4.7E-04	3.5E-04	6.3E-04

Table A.2: Summary of uncertainty analysis for vapor composition.

A3. Residual Plots for the Verification Measurements

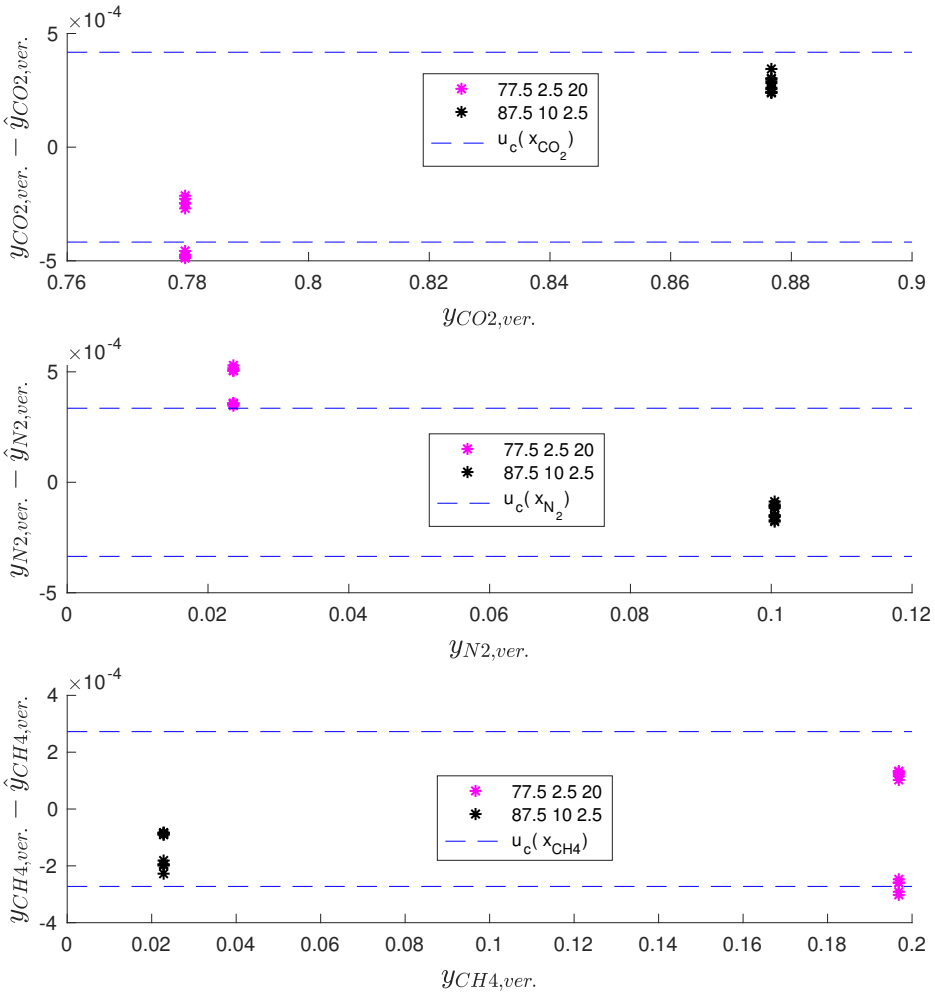

Figure A.3: Residuals between the fitted composition calibration function for the liquid sampler and the gravimetrically determined composition of the two calibration gases used to take verification samples, plotted versus mole fraction of CO_2(top), N_2(middle) and CH_4(bottom). The standard combined uncertainty of each component is included as blue stapled lines.

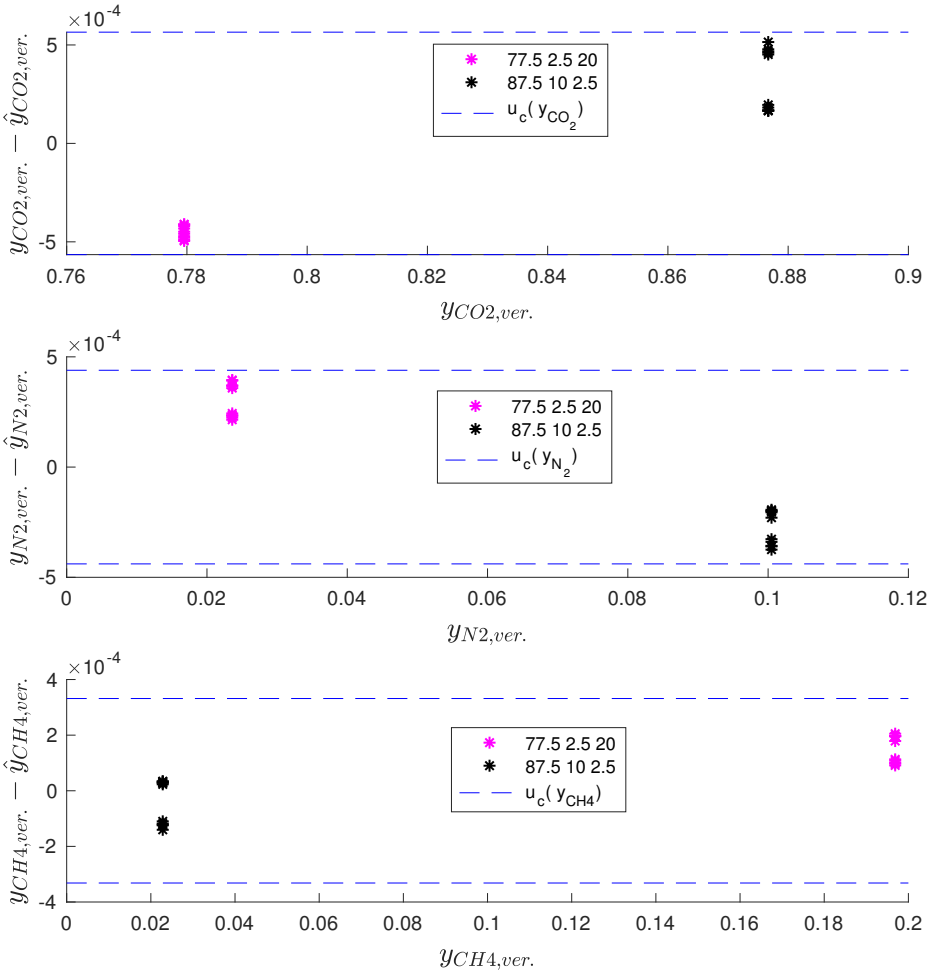

Figure A.4: Residuals between the fitted composition calibration function for the vapor sampler and the gravimetrically determined composition of the two calibration gases used to take verification samples, plotted versus mole fraction of CO_2(top), N_2(middle) and CH_4(bottom). The standard combined uncertainty of each component is included as blue stapled lines.

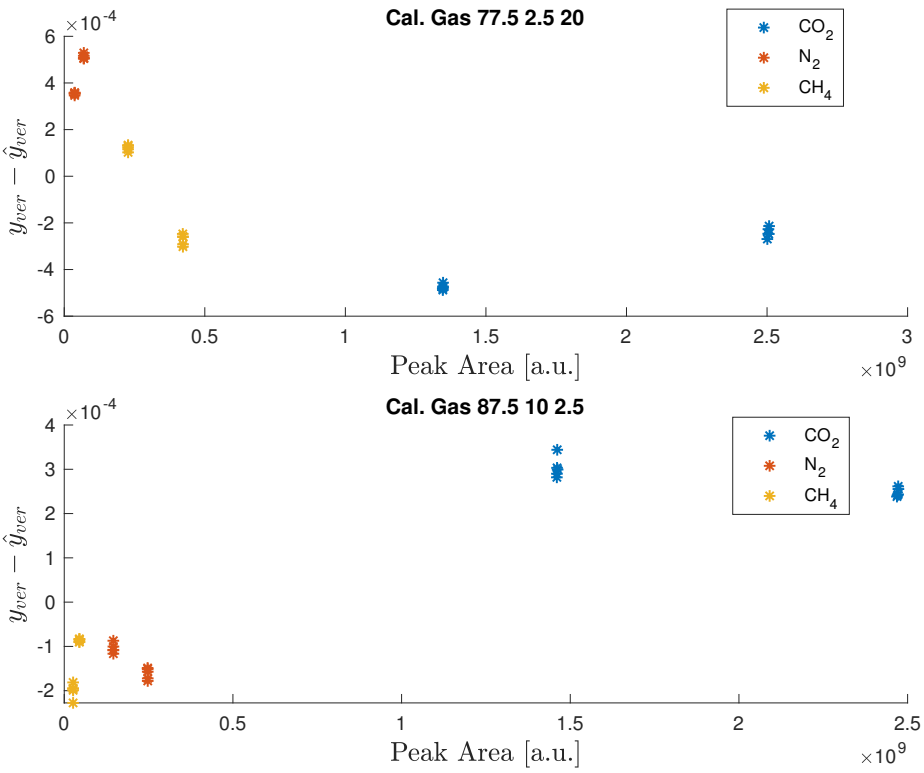

Figure A.5: Residuals between fitted composition calibration function for the liquid sampler and the gravimetrically determined composition of the two calibration gases used to take verification samples, plotted versus peak area. The calibration gas is specified above each sub figure.

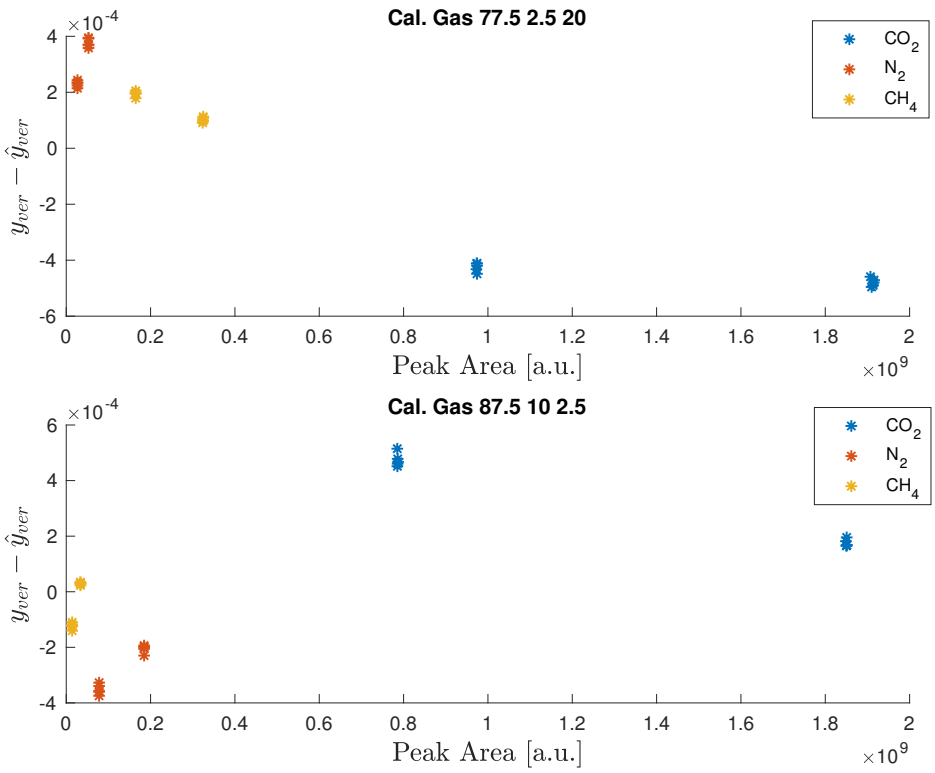

Figure A.6: Residuals between fitted composition calibration function for the vapor sampler and the gravimetrically determined composition of the two calibration gases used to take verification samples, plotted versus peak area. The calibration gas is specified above each sub figure.

A4. Pure Component Residual Contributions of the Mixture of CO_2-N_2-CH_4

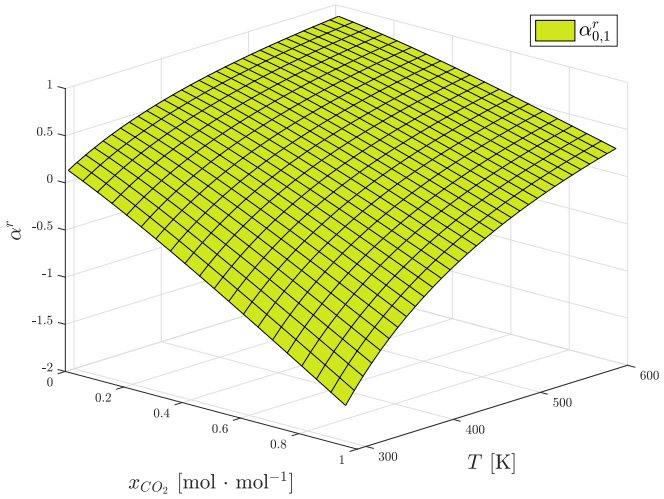

Figure A.7: The residual Helmholtz energy contribution from the pure component CO_2 in the ternary mixture of CO_2-N_2-CH_4, referred to as component 1 in the figure. Mole fraction of CO_2, x_{CO_2}, and temperature, T, on the x- and y-axis with the ratio between mole fraction of N_2 and CH_4 constant and equal to 1, x_{N_2}:x_{CH_4}=1, and density constant and equal to 20 mol/dm^3.

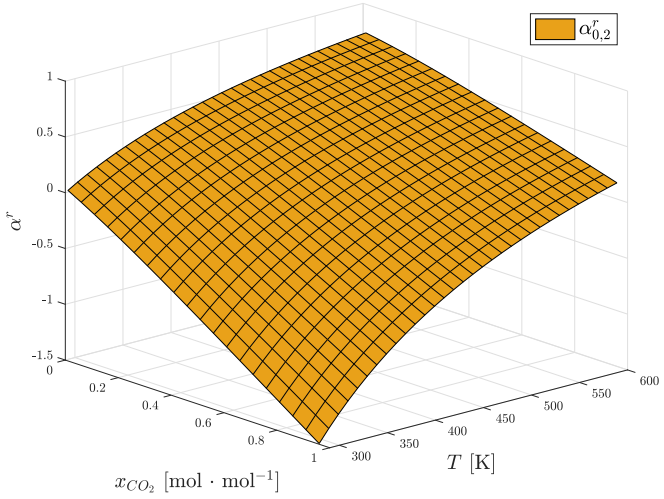

Figure A.8: The residual Helmholtz energy contribution from the pure component N_2 in the ternary mixture of CO_2-N_2-CH_4, referred to as component 2 in the figure. Mole fraction of CO_2, x_{CO_2}, and temperature, T, on the x- and y-axis with the ratio between mole fraction of N_2 and CH_4 constant and equal to 1, x_{N_2}:x_{CH_4}=1, and density constant and equal to 20 mol/dm^3.

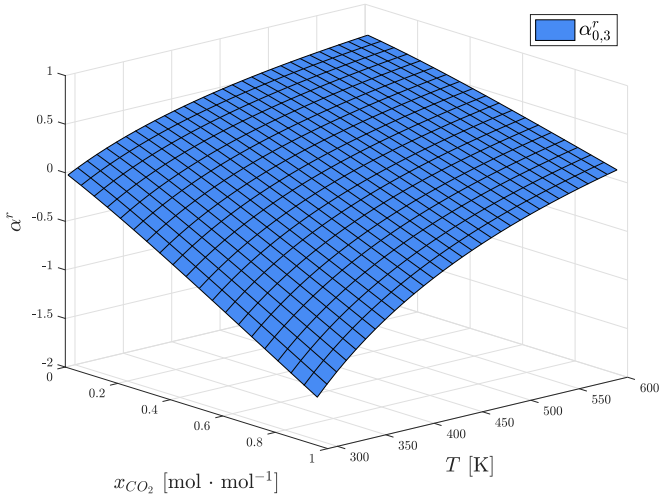

Figure A.9: The residual Helmholtz energy contribution from the pure component CH_4 in the ternary mixture of CO_2-N_2-CH_4, referred to as component 3 in the figure. Mole fraction of CO_2, $x_{\mathrm{CO_2}}$, and temperature, T, on the x- and y-axis with the ratio between mole fraction of N_2 and CH_4 constant and equal to 1, $x_{\mathrm{N_2}}$:$x_{\mathrm{CH_4}}$=1, and density constant and equal to 20 mol/dm^3.

A5. Individual Binary Combination Terms of the Mixture of CO_2-N_2-CH_4

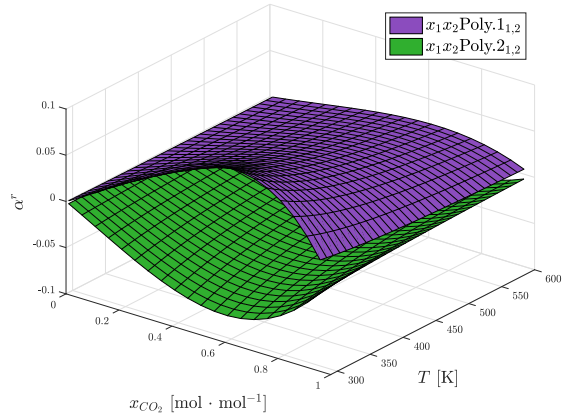

Figure A.10: Polynomial terms of the binary combination of CO_2-N_2 in the ternary mixture of CO_2-N_2-CH_4 multiplied with the mole fraction of CO_2 and N_2. Mole fraction of CO_2, z_{CO_2}, and temperature, T, on the x- and y-axis with the ratio between mole fraction of N_2 and CH_4 constant and equal to 1, z_{N_2}:z_{CH_4}=1, and density constant and equal to 20 mol/dm^3.

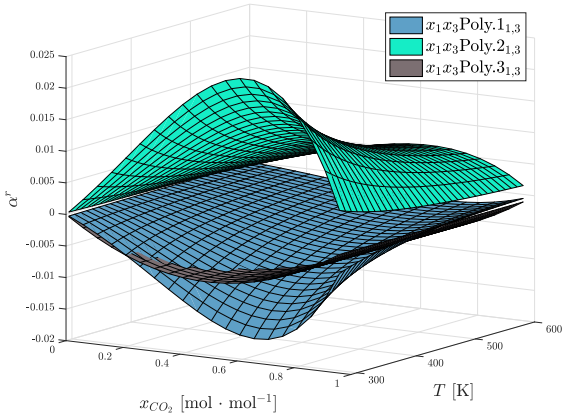

Figure A.11: Polynomial terms of the binary combination of CO_2-CH_4 in the ternary mixture of CO_2-N_2-CH_4 multiplied with the mole fraction of CO_2 and CH_4. Mole fraction of CO_2, z_{CO_2}, and temperature, T, on the x- and y-axis with the ratio between mole fraction of N_2 and CH_4 constant and equal to 1, z_{N_2}:z_{CH_4}=1, and density constant and equal to 20 mol/dm^3.

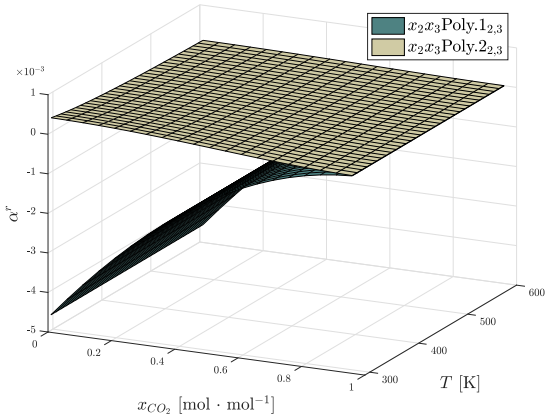

Figure A.12: Polynomial terms of the binary combination of N_2-CH_4 in the ternary mixture of CO_2-N_2-CH_4 multiplied with the mole fraction of N_2 and CH_4. Mole fraction of CO_2, z_{CO_2}, and temperature, T, on the x- and y-axis with the ratio between mole fraction of N_2 and CH_4 constant and equal to 1, z_{N_2}:z_{CH_4}=1, and density constant and equal to 20 mol/dm^3.

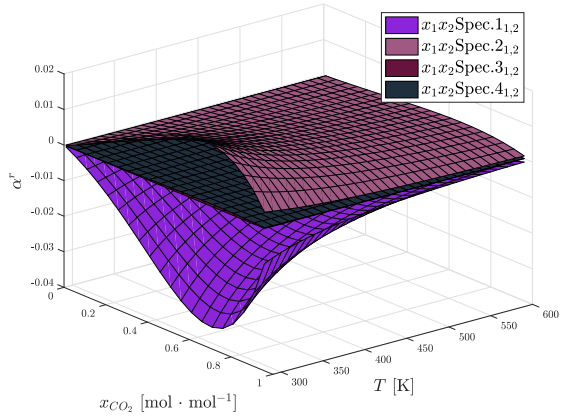

Figure A.13: Special exponential terms of the binary combination of CO_2-N_2 in the ternary mixture of CO_2-N_2-CH_4 multiplied with the mole fraction of CO_2 and N_2. Mole fraction of CO_2, z_{CO_2}, and temperature, T, on the x- and y-axis with the ratio between mole fraction of N_2 and CH_4 constant and equal to 1, z_{N_2}:z_{CH_4}=1, and density constant and equal to 20 mol/dm^3.

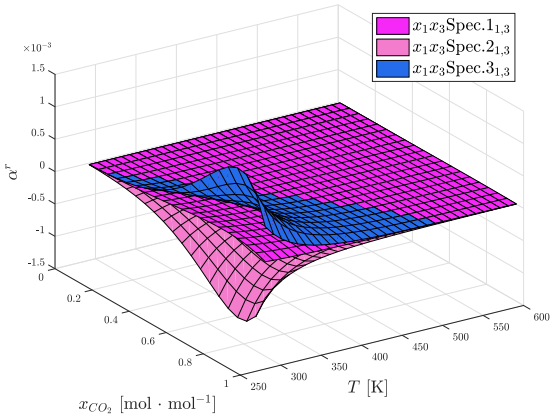

Figure A.14: Special exponential terms of the binary combination of N_2-CH_4 in the ternary mixture of CO_2-N_2-CH_4 multiplied with the mole fraction of N_2 and CH_4. Mole fraction of CO_2, z_{CO_2}, and temperature, T, on the x- and y-axis with the ratio between mole fraction of N_2 and CH_4 constant and equal to 1, z_{N_2}:z_{CH_4}=1, and density constant and equal to 20 mol/dm^3.

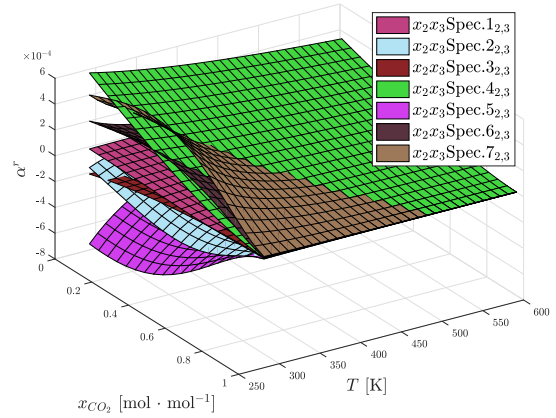

Figure A.15: Special exponential terms of the binary combination of N_2-CH_4 in the ternary mixture of CO_2-N_2-CH_4 multiplied with the mole fraction of N_2 and CH_4. Mole fraction of CO_2, z_{CO_2}, and temperature, T, on the x- and y-axis with the ratio between mole fraction of N_2 and CH_4 constant and equal to 1, z_{N_2}:z_{CH_4}=1, and density constant and equal to 20 mol/dm^3.

Sindre Ottøy

VLE Measurements and Verification of a Helmholtz Energy Equation of State for the Ternary Mixture of CO_2-N_2-CH_4

NTNU
Kunnskap for en bedre verden

SINTEF